MULTISCALE MODELING AND DESIGN OF ULTRA-HIGH-PERFORMANCE CONCRETE

A Dissertation
Presented to
The Academic Faculty

by

Brett D. Ellis

In Partial Fulfillment
of the Requirements for the Degree
Doctor of Philosophy in the
George W. Woodruff School of Mechanical Engineering

Georgia Institute of Technology

December 2013

MULTISCALE MODELING AND DESIGN OF
ULTRA-HIGH-PERFORMANCE CONCRETE

Approved by:

Dr. David L. McDowell, Advisor
George W. Woodruff School of
Mechanical Engineering
Georgia Institute of Technology

Dr. Kimberly Kurtis
School of Civil and
Environmental Engineering
Georgia Institute of Technology

Dr. Min Zhou
George W. Woodruff School of
Mechanical Engineering
Georgia Institute of Technology

Dr. Naresh Thadhani
School of Material Science and
Engineering
Georgia Institute of Technology

Dr. Richard Neu
George W. Woodruff School of
Mechanical Engineering
Georgia Institute of Technology

Dr. Stanley Woodson
United States Army Corps of
Engineering
University of Illinois

Date Approved: June 27, 2003

I dedicate this dissertation to my wife and two daughters, who support and inspire me.

ACKNOWLEDGEMENTS

Finally, I thank my daughters, Emily and Bailey Ellis, for inspiring me each and every day.

TABLE OF CONTENTS

LIST OF TABLES

LIST OF FIGURES

SUMMARY

Ultra-High-Performance Concretes (UHPCs) are a promising class of cementitious materials possessing mechanical properties superior to those of Normal Strength Concretes (NSCs). However, UHPCs have been slow to transition from laboratory testing to insertion in new applications, partly due to an intuitive trial-and-error *materials development process*. This research seeks to addresses this problem by implementing a *materials design process* for the design of UHPC materials and structures subject to blast loads with specific impulses between 1.25- and 1.5-MPa-ms and impact loads resulting from the impact of a 0.50-caliber bullet travelling between 900 and 1,000 m/s. The implemented materials design process consists of simultaneous bottom-up deductive mappings and top-down inductive decision paths through a set of process-structure-property-performance (PSPP) relations identified for this purpose. The bottom-up deductive mappings are constructed from a combination of analytical models adopted from the literature and two hierarchical multiscale models developed to simulate the blast performance of a 1,626-mm tall by 864-mm wide UHPC panel and the impact performance of a 305-mm tall by 305-mm wide UHPC panel. Both multiscale models employ models at three length scales – single fiber, multiple fiber, and structural – to quantify deductive relations in terms of fiber pitch (6-36 mm/revolution), fiber volume fraction (0-2%), uniaxial tensile strength of matrix (5-12 MPa), quasi-static tensile strength of fiber-reinforced matrix (10-20 MPa), and dissipated energy density (20-100 kJ/m^2). The inductive decision path is formulated within the Inductive Design Exploration Method (IDEM), which determines robust combinations of properties, structures, and processing steps that satisfy the performance requirements. Subsequently, the preferred material and structural designs are determined by rank order of results of objective functions, defined in terms of mass and costs of the UHPC panel.

CHAPTER 1:

INTRODUCTION

Advances in civilization are closely tied to advances in materials; so much so that entire spans of time are named after the most advanced material of the age. For example, the Bronze Age was named after the then most advanced material, smelted arsenic and bronze. New materials continue to advance civilization; three recent examples include: (1) silicon used in transistors leading to a rapid increases in inexpensive computational resources; (2) carbon-fiber reinforced composite materials leading to energy efficient airplanes, such as the Boeing 787; and (3) lithium-based compounds used in batteries leading to lightweight portable electronic devices such as smart phones. Clearly, materials are important to the advancement of civilization.

The process of developing new materials has been and still is a laborious, iterative, and intuitive process characterized by four steps: (1) generate a new idea for a new or improved material; (2) process the material in a laboratory environment; (3) test the new material for a combination of physical, chemical, thermal, or other properties; and (4) repeat steps one through three as needed until the desired properties are realized. Subsequently, the new material must find a path to commercial viability. Here, commercial viability is defined by three criteria: (1) the material must be usable in a structure; (2) the material must be capable of being manufactured, or processed, at the quantities needed and with the target properties to satisfy demand; and (3) the material must be economically profitable at the volumes needed for the previously identified

structures and processing conditions. Unfortunately this *materials development and insertion process* is not guaranteed to produce the desired new material. Moreover, when it does produce a new or improved material satisfying the requirements, the *materials development and insertion process* typically requires fifteen years or longer.

The lengthy time required by the *materials development and insertion process* can be observed in the development of Normal Strength Concretes (NSCs) and Ultra-High-Performance Concretes (UHPCs), both of which are cementitious granular materials primarily composed of Portland Cement (PC), aggregate, reinforcement, and water. Figure 1 shows the annual consumption of Portland Cement – used here as a proxy for the consumption of NSC – in the United States as a function of year from 1824 to 2012 (Anon., 1988; Graybeal, 2012; Kelly, van Oss, & Matos, 2012; Mindess, Young, & Darwin, 2002). The invention of "modern" Portland Cement in 1845 marks the invention of NSC. Thirty-five years later in 1880, only 22 thousand metric tons, or less than 0.5 kg per person, of Portland Cement were consumed in the United States. In contrast, 415 kg per person of Portland Cement were consumed in 2005. The slow development of NSCs is mirrored in the development of UHPCs. For example, UHPCs were in invented 1978; thirty-four years later in 2012, only 18 UHPC bridges have been constructed in North America. Thus, the *materials development and insertion process* is still laden with problems.
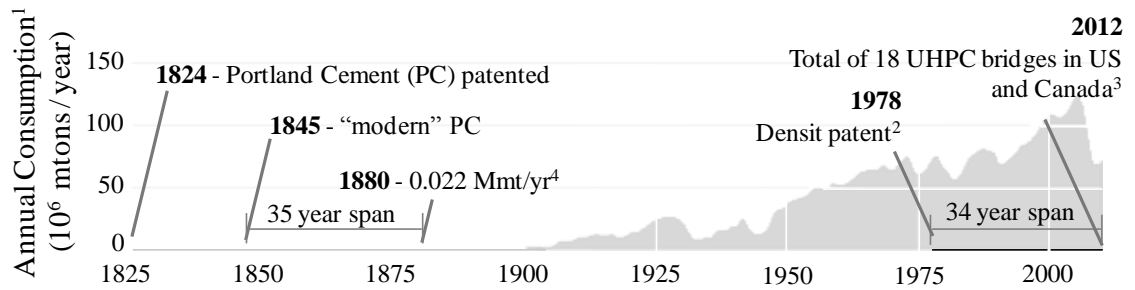
[1] Kelly, van Oss, & Matos (2012),
[2] Anon (2010)
[3] Gaybeal (2012)
[4] Mindess, Young, and Darwin (2003).

Figure 1.   United States Portland Cement (PC) consumption from 1825 to 2012, highlighting the 35 and 34 years span after the invention of Normal Strength Concrete (NSC) and Ultra-High-Performance Concrete (UHPC), respectively.

The time required by the material development and insertion process is a symptom of four systematic problems (McDowell et al., 2009a). First, the final material design is determined by optimizing the performance of the initial material design; thus alternative material designs with possible superior properties are tacitly omitted. Second, the time needed to process and test each test material limits the rate at which new materials are introduced. Third, the expense of physical experiments limits the number of physical experiments performed; thus, optimization in the materials development process continues until the performance requirement is met. Fourth, the materials development process can only produce materials that are possible with current manufacturing technology.

The problems associated with the *materials development and insertion process* are exacerbated for extreme loading conditions, such as blast and impact. Specifically, the physical experiments forming the feedback mechanism for the *materials development*

process are more expensive and time intensive than conventionally loaded structures. A confounding problem is that an expected range of levels of extreme loading, e.g. impulse of a blast load or the velocity of an impact, may change substantially depending on various factors. To rapidly adapt to current and future extreme loading conditions, a new materials design process is needed.

The genesis for the proposed materials design process emanates from Olson (1997), who clarified the simultaneous deductive and inductive paths within a material's process-structure-property-performance relations. The deductive path seeks to form accurate cause-effect relations in a bottom-up manner through the process-structure-property-performance relations. The inductive path involves a top-down search for properties, structures, and processing steps that satisfy the overall performance requirements of the structure.

The recent increase in cost-effective computational resources allows the deductive path to be moved from a physical domain, primarily comprised of testing in a laboratory, to primarily a computational domain. However, the deductive path in the computational domain gives rise to new problems. First, the actual microstructure in a given physical sample is rarely known, instead low order attributes, such as the volume fraction and mean size of each constituent, may be available from processing conditions or a micrograph from a similarly processed material. This leads to uncertainty in the placement and orientation of microstructures to be modeled. Second, numerical simulations require model assumptions to be tractable. For example, models often include boundary condition assumptions such as plane strain or periodic boundaries. Third, the number of degrees of freedom possible in numerical models is finite; therefore,

responses from smaller length-scales must be homogenized and the physical domain simulated is much smaller than physical specimens. Fourth, multiscale modeling requires a transition between length and time scales. Finally, robust design algorithms need to be employed.

This dissertation addresses these problems by applying a top-down *materials design process* to the design of Ultra-High-Performance Concrete (UHPC) subject to the extreme loading conditions of blast and impact. The specific objectives of this dissertation are to:

- develop and validate models at length and time scales relevant to the blast loading of UHPC panels;

- link the models together into a multiscale modeling framework to accurately model phenomenon relevant to blast loading of UHPC panels;

- determine an appropriate mapping of the process-structure-property-performance relations for blast and impact loading;

- inductively (top-down) search for ranged sets of inputs satisfying the performance requirements; and

- identify preferred combinations of design variables that satisfy the system level requirements.

The remainder of this dissertation is organized as follows. Chapter 2 reviews relevant background material pertaining to UHPC materials, the development of UHPC materials, and extreme loading conditions such as blast and impact loading. Chapter 3 details the multiscale model of a UHPC blast panel consisting of three different length

scales: single-fiber, multiple-fiber, and structural length scale. The multiscale model is validated by results of physical experiments conducted at the United States Army Corps of Engineers (USACE) Engineer Research Development Center (ERDC). Chapter 4 details the model at the structural level length scale for simulating impact loading. Chapter 5 provides the theoretical framework for the design problem. Chapter 6 exercises the design framework for designing UHPCs for blast loading and impact loading. Finally, Chapter 7 summarizes the dissertation and highlights the unique contributions of this research.

The unique contributions of this dissertation are as follows:

- Develops and validates a multiscale model at three different length scales for predicting the evolution of damage, deflection, and critical impulse for a UHPC panel subjected to blast loading;
- Develops a computational framework for the analysis of uniformly pitched non-circular cross section reinforcement fibers pulled from a cementitious matrix. This framework represents the first time that uniformly pitched non-circular cross section fibers have been (1) modeled in the finite element framework and (2) modeled within a matrix with constitutive properties other than an elastic, homogeneous matrix;
- Provides an alternate explanation of the mechanisms causing the elastic-plastic response of twisted fibers being pulled from a cementitious matrix;
- Implements the Inductive Design Exploration Method (IDEM) (Choi et al., 2008) in a large multiscale framework; and
- Identifies preferred designs that minimize cost and mass of UHPC materials for structures and satisfy system performance requirements related to blast and impact.

CHAPTER 2:

BACKGROUND

The objective of this dissertation is to reduce the time required to develop new UHPC materials and structures to less than 10 years by implementing a *materials design process*. To support the achievement of this, this chapter reviews relevant background information and is organized as follows. Section 2.1 establishes a classification scheme for cementitious materials. Section 2.2 characterizes UHPCs and compares UHPCs to NSCs. Section 2.3 reviews previous research on blast and impact loading conditions. Section 2.4 presents the constitutive models used by previous researchers to model cementitious materials. Section 2.5 reviews approaches to link different length scales within multiscale models. Section 2.6 reviews approaches to the inverse design algorithm, IDEM.

2.1   Classification of cementitious materials

Cementitious materials are granular composites characterized by a common composition of Portland Cement and water. Unless specified otherwise, the following classifications of cementitious materials are adopted in this dissertation. Cement paste, or paste, is the hardened material created after curing a mixture of Portland Cement and water. Cement pastes may contain other admixtures such as High-Range Water Reducing Agents (HRWRA), but may not contain higher length-scale constituents such as fibers, aggregates, or sand. Cement mortar, or mortar, is the hardened material created

after curing a mixture of Portland Cement, sand, and water. Cement mortars may contain

admixtures such as HRWRA, but may not contain aggregate or fibers. Normal Strength

Concrete (NSC) is the hardened material created after mixing Portland Cement, aggregate

with a diameter typically between 9 and 50 mm, sand, and water. NSCs have unconfined

compressive strengths, as specified by American Society for Testing and Materials

(ASTM) C39 (2012a), less than or equal to 50 MPa. Ultra-High-Performance Concrete

(UHPC) is the hardened material created after mixing Portland Cement, sand, silica fume,

quartz powder, high-range water reducing agents, fibers, and water. Although UHPCs

generally have unconfined compressive strengths greater than 150 MPa (Naaman &

Wille, 2012), they may be more generally defined in terms of performance, rather than

strength. Between NSCs and UHPCs lies a range of cementitious materials referred to as

High-Performance Concretes with unconfined compressive strengths between 50 and 150

MPa, . In general, HPCs have the same constituents of UHPCs, but with a higher water

to cement ratio, w/cm.

2.2   Characteristics of UHPC

UHPCs are cementitious granular composites composed of Portland Cement,

sand, quartz powder, silica-fume, high-range water reducing agents, fibers, and water.

The high-range water reducing agents allow water to cementitious material w/cm ratios

to be less than 0.3 without affecting the workability of the UHPC slurry (Richard,

Cheyrezy, & Dugat, 1996). In comparison, NSCs are composed of Portland Cement,

aggregate, sand, and water, and typically have w/cm ratios between 0.4 and 0.7. The

composition of UHPCs leads to a denser, less porous microstructure. Accordingly,

denser microstructures lead to improved mechanical and mass transport properties. For example, UHPCs typically have unconfined compressive and tensile strengths greater than 150 MPa and 10 MPa, respectively; NSCs have typical unconfined compressive and tensile strengths of 28 MPa and 3 MPa, respectively. The improved mass transport properties are quantified by improved freeze-thaw performance (Thomas et al., 2012) and reduced chloride ion transport (Oh et al., 2002).

The following two sections discuss the role of porosity and fiber content in the structure and properties of UHPC.

2.2.1 Porosity

Porosity in cementitious materials occurs within the cement matrix and tends to increase near the boundary of coarser length scale incorporated phases, e.g. fibers or aggregate. Here, the matrix is defined to be cement mortar for NSCs or the hardened mixture of Portland Cement, water, silica fume, and quartz powder for UHPCs.

The cementitious matrix can be divided into two different phases depending on the proximity to coarser length scale interstitials. The first phase, commonly referred to as the Interfacial Transition Zone (ITZ), is a relatively porous region located within a 10- to 50-μm-thick shell around non-porous aggregates and fibers (Mehta & Monteiro, 2005). Even though the thickness of ITZ is quite small, the 75 to 100 μm mean spacing between aggregates in NSC allows the ITZ to comprise between 20 and 40% of the total volume not occupied by aggregates (Mindess et al., 2002). Combined with the high levels of porosity, the 20 to 40% volume fraction of the ITZ to the total matrix cause the ITZ to dictate percolation properties, e.g. chloride ion diffusion (Oh et al., 2002), for NSC

microstructures. Computational simulations by Garboczi and Bentz (1991) indicate that the thickness and elevated porosity of the ITZ are caused by elevated w/cm ratios near the surface of interstitials. The second phase of the matrix, or bulk matrix, is the portion of the matrix that is further away from the surface of coarser scale interstitials. The bulk matrix is characterized by lower levels of porosity than the ITZ.

The processing of UHPCs reduces the porosity within the ITZ and bulk matrix by selectively controlling the constituents. First, high-range water reducing agents are used to reduce w/cm ratios to levels near 0.2 while maintaining adequate workability, thus preventing the formation of voids during casting. Second, the mean particle diameter and volume fraction of each constituent are prescribed in order to increase the packing density of the microstructure (de Larrard & Sedran, 1994). For example, consider the packing density of a binary granular composite composed of constituent-1 and constituent-2. If both constituents are idealized as mono-disperse spheres of the same diameter, a random distribution of spheres leads to a 64% observed packing density, i.e., $V_{pore} = 0.36$ (Cumberland & Crawford, 1987). Note that the random distribution of particles creates a lower packing density than the theoretically possible 76% for hexagonal-close-packed systems (Cumberland & Crawford, 1987). However, if the constituents have different mean diameters, de Larrard and Sedran (1994) showed that the observed packing density can be increased to 75%, a 17% improvement over uniform diameter constituents, by using a 30% volume fraction of constituent-2 that has a diameter $1/16^{th}$ of constituent-1. The influence of particle size and volume fractions on packing density has motivated at least 15 different particle packing models that can be classified by the treatment of the particles in the model (discrete or continuous) and by

the number of components (binary, ternary, or higher order) (Alexander & Mindess, 2005).

By controlling the incorporated phases, or "constituents", volume fractions of constituents and mean diameter of the constituents, UHPC pores are smaller and occupy less total volume than the pores within NSC. For example, Klobes et al. (2008) determined that a UHPC had a 3.0-nm mean pore radii and a 8.8% total porosity volume fraction, whereas a NSC had a 54.1-nm mean pore radii and 16.9% total porosity.

2.2.2   Fiber-Reinforcement

Although straw and asbestos fibers have reinforced mud and clay for millennia (Mehta & Monteiro, 2005; Mindess et al., 2002), Naaman (1985) dates the modern use of short, discontinuous randomly-oriented fibers within cementitious materials to the early 1960's. The primary use of fibers is to increase the ductility and toughness of cementitious material, which is quasi-brittle without fibers. A secondary use of fibers is to mitigate the risk of explosive spall due to rapid thermal heating (cf. Bentz, 2000; Bilodeau, Kodur, & Hoff, 2004; Hertz, 2003; Kalifa, Chéné, & Gallé, 2001). This secondary use will not be covered in this dissertation.

Fibers of various shapes and the influence of fiber shape of the response at the single fiber and multiple fiber length scales have been examined since the early 1960s, when researchers modified the morphology of fibers from straight and smooth with circular cross sections to include either off-axis or on-axis features (Naaman, 1985). Initially, researchers focused on adding off-axis features, e.g. crimping along the fiber's length or making hooks at the ends of the fiber, to fibers having circular cross sections.

In 1999, Naaman (1999) introduced on-axis features and patented helically twisted fibers with polygonal-shaped cross-sections. Although possible, experimental or numerical research has not been published documenting the effects of combining on-axis and off-axis features within a single fiber.

Fibers used in UHPCs are typically straight, smooth fibers with circular cross sections made from high strength steel. The diameters of the cross section depends on the constituents of the matrix surrounding the fiber. For example, Richard, Cheyrezy, and Roux (1996) recommend the diameter of the fiber be smaller than maximum particle diameter, which in their case was 0.4 mm. A fiber's length should be as long as possible without exceeding the fiber's critical length, at which a fiber ruptures instead of slips (Johnston, 2001). Typical values of the fiber length to diameter ratio, or aspect ratio, λ, are between 60 and 100.

The influence of fiber morphology is experimentally determined via the single-fiber pullout test. The result of the test is a pullout force, defined as the force at which the fiber inelastically is removed from the matrix, as a function of end slip. End slip is measured as the difference between the current and the reference configurations for the point on the fiber that is initially at the crack face of the matrix. The single-fiber pullout test is relatively inexpensive and can account for the angles between the fiber's embedded axis and the pull direction. The typical responses of straight, smooth fibers, hooked fibers, and twisted fibers are reviewed next.

Straight, smooth fibers with circular cross sections exhibit three energy storage and dissipation stages (Boshoff, Mechtcherine, & van Zijl, 2009; Cunha, Barros, & Sena-Cruz, 2010; Easley, Faber, & Shah, 1999; Kim, El-Tawil, & Naaman, 2009). In the first

stage, energy is stored as the fiber undergoes relatively small displacements before the peak force is reached. In the second stage, the pullout force decreases as the chemical bonds between the fiber and the matrix break. In the third stage, the pullout force decreases as the end slip increases, and energy dissipates via friction at the fiber-matrix interface. For straight, smooth fibers, the fiber length has a strong influence on the peak pullout force. For example, Cunha, Barros, and Sena-Cruz (2010) reported a 100% increase in peak pullout force when fiber length is increased from 20 mm to 30 mm. Additional studies were conducted by Chan and Chu (2004a) and Guerrero and Naaman (2000) to determine the effects of matrix constituents on pullout behavior.

Hooked fibers exhibit behaviors different from those of straight fibers. As reported by Cunha, Barros, and Sena-Cruz (2010), a hooked fiber embedded 20 mm into a matrix shows a peak pullout force approximately 4.5 times that of a straight, smooth fiber embedded at the same depth. Even though the peak pullout force of a hooked fiber increases with the embedded length of the fiber, the increase is not as pronounced as that for straight, smooth fibers (Cunha et al., 2010). In addition to the three energy storage and dissipation mechanisms of straight, smooth fibers, hooked fibers also dissipate energy via plastic work during pullout. Although not a distinct mechanism, the residual stress in a fiber's hook appears to increase normal tractions and ultimately the force required during the friction-dominated stage of pullout.

Twisted fibers display a behavior that is different from that of either straight, smooth fibers or hooked fibers. The single fiber pullout results by Naaman (2003) indicate substantial differences in maximum pullout force, end slip at which maximum pullout force is reached, and pullout force during the last 20% of the fiber length.

Twisted fibers generate peak pullout forces on the order of two to three times those of straight, smooth fibers, depending on the morphology of the twisted fiber. The second difference is that twisted fibers reach maximum pullout forces at approximately 10 times the end slip distance as that of straight or hooked fibers. This work-hardening behavior has important implications for the distribution of damage throughout structural-level length scales (Kim, El-Tawil, & Naaman, 2007). The third difference is that twisted fibers maintain pullout forces close to the maximum pullout force for up to 80% of a fiber's embedded length. These three differences cause the total work for pullout of a twisted fiber to be four to five times greater than that for a straight, smooth fiber (Naaman, 2003). Other studies concerning twisted fibers have determined the influence of matrix composition (Guerrero & Naaman, 2000), the rate of pullout (Kim et al., 2009), and the number of fiber strands (Sujivorakul & Naaman, 2002). Although Naaman and coworkers were first to use twisted, polygonal, discontinuous, and randomly oriented fibers, Menzel (1952) documented similar improvement in the pullout behavior of continuous steel rebar reinforcement placed in cementitious matrices. Menzel's results indicate that a helically threaded rebar reinforcement sustains greater than 10 times the stress of a straight, smooth rebar over the first 0.40 mm of end slip.

Analytical models of a single straight, smooth fiber being pulled out of a matrix have been framed in terms of energy balance (Focacci, Nanni, & Bakis, 2000) and equilibrium (Naaman et al., 1991). The equilibrium-derived analytical model uses experimental data to determine five constants: bond modulus, bond strength, constant frictional bond stress, and two decaying frictional parameters. Numerically, Li and Mobasher (1998) used a two-dimensional axisymmetric framework containing three

linear elastic constitutive relations to simulate the three pertinent materials: fiber, interface, and matrix. The modeled mechanisms include fiber debonding and friction. A clamping pressure was applied at the outer edge of the matrix to simulate shrinkage. Results were presented and compared to experimental data for the first 0.1 mm of end slip.

An analytical model to predict the pullout force versus end slip relation for hooked fibers was introduced by Alwan, Naaman, and Guerrero (1999), who extended the model of straight, smooth fibers given by Naaman, Namur, Alwan, and Najm (1991). The model predicts four different characteristic responses depending on the end slip of the fiber. The first characteristic response is a rapid increase in pullout load as the fiber undergoes debonding. Second, the pullout force increases to a maximum value and maintains the maximum value as both kinks in the embedded end of the fiber respond as plastic hinges during increased end slip. The third characteristic response occurs when the deepest kink of the embedded end of the hooked fiber completely passes through the curved portion of the fiber bed. At this point, the pullout force decreases to lower value until the fiber is completely removed from the hooked part of the fiber bed, thus leading to the characteristic fourth response: a friction-dominated pullout similar to that of a straight, smooth fiber.

An analytical model to predict the pullout of a twisted fiber was presented by Sujivorakul and Naaman (2003), with complete details given by Sujivorakul (2002). The analytical model assumes a homogeneous elastic matrix surrounding an elastic-plastic fiber. The model accounts for the fiber's embedded length, cross-sectional shape, pitch, untwisting torque, tensile strength of the fiber, and friction between the fiber and the

15

matrix. Calibration of the model requires experimental data pertaining to the bond shear stress versus slip relation, untwisting torque at the embedded tip of the fiber, and a locking torque coefficient, each of which depend upon the pitch of the fiber and the cementitious matrix surrounding the fiber. In other words, for a given fiber and matrix, a different calibration is required for each pitch and matrix. Although the analytical model has been used to predict the pullout force during the first 5 mm of end slip, the model does not capture the experimentally observed matrix tunneling, defined as the erosion of the matrix surrounding the fiber as the fiber is pulled from the matrix, or the resulting rapid decrease in pullout force at end slips between 70 to 80% of the fiber's initial embedded length.

Although it is important to understand how a single fiber interacts within the surrounding cementitious matrix, fibers are distributed throughout cementitious materials. Therefore, the influence of multiple fibers must also be understood. The number of fibers within a cementitious material is quantified by the fiber volume fraction, V_{fiber}, defined as the volume of fibers divided by the total volume of the cementitious matrix and the fibers. A theoretical upper bound for the maximum fiber volume fraction, $V_{fiber,\max}$, of randomly placed fibers was calculated and measured by Parkhouse and Kelly (1995), who showed that $V_{fiber,\max} = 2\ln(\lambda)/\lambda$. For typical aspect ratios of 60 and 100, the maximum fiber volume fractions are 15 and 10%, respectively. However, UHPCs typically have fiber volume fractions between 1 and 3%, and rarely greater than 5%. Fiber volume fractions less than $V_{fiber,\max}$ are used because mechanical properties degrade before reaching the theoretical fiber volume fractions. For example, Richard, Cheyrezy, and Roux (1996) showed that the flexural strength reaches a maximum of approximately

60 MPa for $V_{fiber} = 4\%$ and the fracture energy reached a maximum of 36 kJ/m^2 for

$V_{fiber} = 2\%$. The reduction in flexural strength and fracture energy stem from a decrease

in workability and resulting creation of porosity. In order to reduce porosity while

increasing fiber content, Rossi (2005) used fibers at three different length scales, namely

lengths of 20, 7.5, and 2 mm and diameters of 0.275, 0.175, and 0.1 mm, respectively, to

produce composites with up to 11% fiber volume fraction.

Because direct tensile tests for concrete are very difficult (Mindess et al., 2002),

tensile properties of cementitious materials are determined via either the third-point

flexure test defined by American Society for Testing and Materials (ASTM) C78 (2012b)

or the splitting tensile strength test defined by ASTM C496 (2012a). The first method,

third-point flexure test, typically uses a $152.4 \times 152.4 \times 508$ mm prismatic beam subject

to four point bending. The tensile face of the beam is loaded at 0.9 to 1.2 MPa/min until

fracture, at which point the modulus of rupture, R, is calculated as $R = \dfrac{PL}{bd^2}$, where P is

the maximum value of the sum of forces at the two center supports, L is the length

between the outside supports, and b and d are the width and depth of the prismatic

beam at the fracture location. This measurement technique has two problems: (1) the

calculation of R assumes small strain; and (2) measurements of ductility and toughness

confound the influence of fiber and matrix because part of the v-notch shape to cracking.

Part of the resistance to cracking is provided from the matrix and part of the resistance to

fracture is provided by fibers after the matrix has already cracked. Thus, this method is

ill-suited to inform material design.

The second method, splitting tensile strength test, specifies that a specimen, in the shape of a right cylinder, should be compressed between two platens across the specimen's diameter at a constant rate between 0.7 to 1.4 MPa/min (2012a). All other surfaces of the specimen must remain traction-free during the test. Although the platens do create local regions of triaxial states of stress, specimens predominantly fail in tension. Thus, the splitting tensile strength, f_{sp}, provides a measure for the quasi-static tensile strength of the material. The problem with this method is that it may over-estimate the role of fibers due to the compressive stress increasing the normal tractions, and thus frictional forces, between the fiber and the matrix.

The influence of V_{fiber} and fiber geometry on NSC and UHPC tensile behavior are inferred from results of the splitting tensile strength, f_{sp}, of the composite to that of the corresponding cementitious material without fiber reinforcement. As shown in Figure 2, the ratio of splitting tensile strength depends on the topology of the fiber as well as the normalized fiber volume fraction, defined as $V_{fiber} \times L_{fiber} / \phi_{fiber}$, where L_{fiber} is the length of the fiber and ϕ_{fiber} is the diameter of the fiber. The data in Figure 2 summarize experimental results published in peer reviewed journals between 1992 and 2010 (El-Dieb, 2009; Gao, Sun, & Morino, 1997; Köksal et al., 2008; Lim & Oh, 1999; Song & Hwang, 2004; Wafa & Ashour, 1992; Yao, Li, & Wu, 2003; Zhang, Yan, & Jia, 2010).
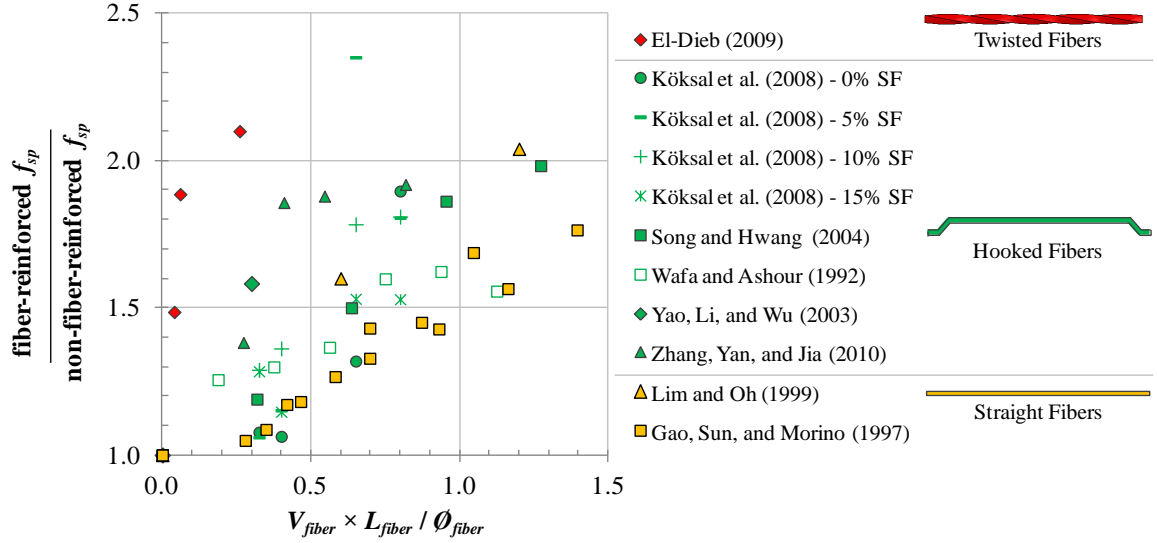
Figure 2.   Effect of normalized fiber volume fraction and fiber topology on the splitting tensile strength of NSC and UHPC.

2.3   Loading conditions

2.3.1   *Blast loading*

Since the introduction of UHPCs (Bache, 1981), results have been published from five experimental programs that subjected a total of 16 UHPC panels to blast loads at scaled distances ranging from 0.37 to 2.18 m/kg$^{1/3}$ (Rebentrost & Wight, 2009). Of the 16 panels, 13 panels were reinforced with steel rebar, and 3 panels were not reinforced. One of the three non-reinforced panels was 2- by 1- by 0.1-m in dimension and survived a reflected impulse of 1.62 MPa-ms (Wu et al., 2009). The maximum and permanent centerline deflections were 13.2 and 4.1 mm, respectively. The two remaining non-reinforced UHPC panels were 3.5- by 1.3- by 0.1-m in dimension with one panel containing 2% volume fraction of fibers and the other panel containing 4% volume

fraction of fibers (Schleyer et al., 2010a). After subjected to a reflected impulse of 0.83

MPa-ms. the panels containing 2% and 4% fiber volume fractions permanently deflected

180 and 90 mm, respectively, at their mid-heights. Without testing until failure, the

limited experimental data provide only a lower limit to the critical load level; the upper

bound remains to be established.

Additional experiments have been performed on NSCs demonstrating the

influence of fiber-reinforcement (Lan, Lok, & Heng, 2005; Zhou et al., 2008) and

unconfined compressive strength (Leppänen, 2005; Nyström & Gylltoft, 2009;

Rebentrost & Wight, 2008; Schenker et al., 2008; Wu et al., 2009; Zhou et al., 2008) on

the response of blast loaded panels.

Numerical simulations of the blast panels have been performed via modified

degree-of-freedom simulations using custom in-house codes (Schleyer et al., 2010b; Wu

et al., 2009) and hydrocode simulations (Leppänen, 2005; Nyström & Gylltoft, 2009;

Schenker et al., 2008; Zhou et al., 2008) using the Riedel-Hiermaier-Thoma (RHT)

constitutive model (Riedel et al., 1999). The responses of UHPC panels have been

simulated via two different computational approaches. Wu et al. (Wu et al., 2009) used a

layered single-degree-of-freedom model to predict the critical energy absorption capacity

of UHPC panels with and without steel rebar reinforcement. This approach relies upon

an a priori assumption of the elastic-plastic response of the panel (Biggs, 1964), which

defines the "shape function." Hence, this approach is limited to elastic-plastic responses

and cannot model fracture. In contrast to the single-degree-of-freedom approach, Zhou et

al. (Zhou et al., 2008) used a coupled damage-plasticity Riedel-Hiermaier-Thoma (RHT)

constitutive model (Riedel, Wicklein, & Thoma, 2008) that is pressure-sensitive and

strain-rate dependent to determine the response of rebar-reinforced UHPC panels. Spall,

defined as the ejection of mass on the surface opposite from that of the blast load

impingement, was modeled by deleting elements with damage values exceeding 0.22 (on

a scale from 0 to 1) during the first 0.5 ms after loading, for strain rates greater than 10 s^{-1}. Although it accounts for spall, this approach underestimated the experimentally

observed deflection by approximately 40%. Furthermore, this approach is not sensitive

to changes in microstructure as expressed by volume fraction of fibers, aggregate, or

porosity (Riedel, Kawai, & Kondo, 2009; Riedel et al., 2008). Note that neither the

layered single-degree-of-freedom model or the damage-plasticity model included

information from length scales smaller than the UHPC or steel rebar reinforcement

levels; thus, neither approach is suitable for supporting materials design, i.e., tailoring the

microstructure to achieve targeted responses or properties. Details of the five sets of

experiments are given in Table 1.

Table 1. UHPC blast loading experiments and numerical analysis.

Time and Location	Panel Dimensions $L \times W \times t$ (m)	Number of Experiments	f_c (MPa)	Rebar	Scaled Distance $(m/kg^{1/3})$	Ref.
May 2004 Woomera, Australia	$2 \times 1 \times 0.050$ $2 \times 1 \times 0.075$ $2 \times 1 \times 0.1$	7	160	yes	1.31 1.75 2.18	Rebentrost and Wight (2008, 2009)
2005 Not published	$1.3 \times 1 \times 0.1$	2	170	yes	0.12 0.14	Rebentrost and Wight (2009); Zhou et al. (2008)
2006 Woomera, Australia	$2 \times 1 \times 0.1$ (with blast resistance window)	1	not available	not available	1.86	Rebentrost and Wight (2009)
2008 University of Adelaide, Australia	$2 \times 1 \times 0.1$ $2 \times 1 \times 0.1$	1 1	152 152	no yes	0.50 0.37	Rebentrost and Wight (2009); Wu et al. (2009)
2008 Cumbria, England	$3.5 \times 1.3 \times 0.1$	4	not published	yes and no	1.51 1.93 2.59	Rebentrost and Wight (2009); Schleyer et al. (2010b)

2.3.2 Impact loading

Impact loading is a dynamic loading process characterized by elastic deformation, inelastic deformation (e.g., compaction), fracture, and fragmentation (Clayton, 2008). Physical characteristics of interest may include the ballistic limit, penetration depth, perforation thickness, and scabbing thickness (Li & Tong, 2003).

The response of UHPCs to impact is characterized by either of two experiments: split Hopkinson pressure bar (SHPB) (Davies, 1948; Gebbeken, Greulich, & Pietzsch, 2006; Grote, Park, & Zhou, 2001; Hopkinson, 1914; Kolsky, 1949) or gas gun flyer plate experiments (Gebbeken et al., 2006; Grote et al., 2001). SHPB loads the test specimen in a state of plane strain due to the propagation of a one-dimensional compressive wave at

strain rates between 250 and 1,700 s^{-1} (Grote et al., 2001). In comparison, gas gun

experiments allow compressive loading at strain rates on the order of 10^4 s^{-1} (Gebbeken et

al., 2006; Grote et al., 2001). Both sets of experiments reveal that the compressive flow

stress of cementitious materials increases with increasing compressive strain rate (e.g.,

(Grote et al., 2001; Malvar & Ross, 1998; Malvern et al., 1985)). These results are

codified by CEB-FIB Model Code 90 (CEB-FIP, 1998) which suggest a significant non-

linear increase in compressive strength for strain rates greater than 30 s^{-1}. Similar to

compressive strain-rate effects, cementitious specimens loaded in tension also have

exhibit significant non-linear increases to tensile strength for strain rates greater than 30

s^{-1} (CEB-FIP, 1998). In this manner, SHPB and gas gun experiments are used to

characterize the material properties of UHPCs during impact loading.

Beyond UHPC material properties, it is often desired to understand how

projectiles and targets interact. For a given target material, target geometry, projectile

material, and projectile geometry, the target's response can be mapped to a "phase

diagram" for a range of impact speeds and obliquity angles, defined as the angle between

the projectile's velocity vector and the normal vector of the target (Backman &

Goldsmith, 1978). For an obliquity angle of 0º, the phase diagram of a 6.35-mm-thick

aluminum alloy panel impacted by a 6.35-mm-diameter ogival-noded projectile depends

on the projectile's speed and may be divided into three regions (Backman & Goldsmith,

1978): (1) embeds intact in which the projectile embeds into the panel, and the panel

remains intact; (2) perforates intact in which the projectile perforates the panel, and the

panel remains intact; and (3) perforates shattered in which the projectile perforates the

panel, and the panel shatters. Here, shatter is defined as multiple fractures such that the

panel separates into more than 1 piece. The ballistic limit is defined as the projectile velocity at which the projectile just perforates the target with a residual speed of 0 m/s; thus, the ballistic limit is the impact speed that separates the embeds intact and the perforates intact regions.

For cementitious targets, it is common to perform physical experiments at a 0° obliquity angle. The physical experiments can be classified as either penetration or perforation experiments. The primary difference between the two tests are that the penetration experiments have very large thickness such that projectile does not perforate the target, whereas perforation experiments have thinner targets and the projectile may or may not perforate the target. Four common responses are: (1) the penetration depth, defined as the depth the projectile penetrates during a penetration experiments; (2) scabbing limit, defined as the minimum target thickness required to prevent scabbing, or the ejection of mass from the distal face; (3) perforation limit, defined as the minimum target thickness to prevent perforation of the target by the projectile; and (4) ballistic limit, defined as the projectile's minimum impact velocity such that the projectile perforates the target of a given thickness.

Projectiles in penetration and perforation experiments are quantified by their length, diameter, mass, and nose shape. The typical nose shapes are blunt, spherical, conical, and ogival. Ogival-nosed projectiles are characterized by Caliber-Radius-Head (CRH) ψ, defined as $\psi = s/2a$, where s is the radius of ogival nose and a is the radius of the projectile (Forrestal & Luk, 1992). The type of projectile nose influences not only the penetration depth, but also the failure pattern of the cementitious target during

deformation (Li et al., 2005). For example, ogival-nosed projectiles are likely to penetrate, tunnel, and cause scabbing of the target.

Impact problems have been solved by empirical, numerical, and analytical techniques (Backman & Goldsmith, 1978). Empirical techniques predict the impact response by interpolating experimental data. Experimental data is restricted to: (1) ratios of target thickness to projectile diameter less than 3; (2) projectile diameters less than 400 mm; (3) projectile densities between 5.5 and 22.1 g/cm^3; (4) impact velocities between 150 and 914 m/s; (5) ratios of perforation thicknesses to projectile's diameter between 3 and 18; and (6) ratios of scabbing thickness to the projectile's diameter between 3 and 18 (Kennedy, 1976). The interpolation of experimental results has led to no fewer than 19 different empirical relations, as documented by Li et al. (2005). Because of the limited range of applicability and need for physical experiments, empirical techniques have in large part been replaced by numerical and analytical techniques.

Numerical simulations modeling impact of UHPC and NSC materials have been done by multiple researchers; the unique approaches are mentioned here. Park et al. (2001) modeled the planar impact of a two-phase microstructure with a pressure-dependent Drucker-Prager yield condition (Drucker & Prager, 1952) and explicit modeling of interfaces between the two phases. Clayton (2008) introduced a self-consistent theory, with a multiplicatively decomposed deformation gradient, that emphasizes adherence to the 2nd law of thermodynamics. Nöldgen et al. (2012) and Riedel et al. (2010) simulated an aircraft engine impacting steel rebar reinforced UHPC panels using the RHT constitutive model (Riedel et al., 1999).

Analytical techniques for solving the penetration problem are based on the Spherical Cavity Expansion (SCE) model first published by Bishop, Hill, and Mott (1945), who estimated the force needed to push a rigid conical punch into an incompressible, ductile material at quasi-static rates. Later, Goodier (1964) extended SCE to include the dynamic penetration of incompressible, ductile, semi-infinite targets by rigid spherical penetrators. The material model for the target was extended by incorporating compressible materials (Hanagud & Ross, 1971) and granular materials such as soil (Forrestal & Luk, 1992) and concrete (Forrestal & Tzou, 1997). The concrete material model includes a cracked region of material as well as the compressible region of material considered previously. Enhancement to the projectile included alterations for conical, blunt, ogival, and arbitrary nose shapes (Bernard & Hanagud, 1975; Chen & Li, 2002; Forrestal & Luk, 1992). The benefit of analytical techniques is that they are based on ordinary differential equations, which are significantly easier to solve than the partial differential equations of finite element analysis.

Analytical techniques for solving the perforation problem have been adapted from the penetration problem. Yankelevsky (1997) proposed a two-stage model for perforation of concrete, in which the first-stage was modeled by a Cylindrical Cavity Expansion (CCE) model and the second-stage was modeled as a scabbing problem. The transition between the first and second stage occurs when the summed forces resisting the projectile from penetrating into the target equals the force required to scab material off of the distal face of the target. Empirical measurements have determined that both NSCs and UHPCs scab at a geometric angle of approximately 70º. Li and Tong (2003) extended the two-stage model to a semi-analytical technique.

2.4   Constitutive models for cementitious materials

During compressive loading, cementitious materials exhibit non-linear behavior at stress levels less than the ultimate compressive strength. Furthermore, the compressive and tensile yield strengths are asymmetric and depend upon the hydrostatic pressure and strain-rate. After reaching ultimate strength, cementitious materials exhibit precipitous strain-softening in tension and a more gradual strain-softening in compression.

Drucker and Prager (1952) introduced a pressure-dependent yield criteria. Soon after, Kachanov (1958) introduced Continuum Damage Mechanics (CDM), which reduced stiffness through a monotonically increasing isotropic damage internal state variable (ISV). Holmquist, Johnson, and Cook (1993) combined aspects of both models to create a phenomenological pressure and strain-rate sensitive damaged-plasticity model for brittle materials. Lubliner et al. (1989) introduced a damaged-plasticity model based on compression and tension plastic strain ISV and an isotropic damage ISV, which was later modified by Lee and Fenves (1998) to contain two damage ISVs, one for tension and one for compression.

As noted by Jirásek (1998), strain-softening constitutive models within the finite element method lose ellipticity, resulting in mesh dependency. Three computational methods have been used to allow strain-localization during strain-softening without creating mesh dependency, namely integral non-local constitutive models (Jirásek & Rolshoven, 2003), gradient-enhanced continua (e.g., second-gradient (Abu Al-Rub & Voyiadjis, 2009)), and use of traction-separation elements (Hillerborg, Modéer, & Petersson, 1976).

2.5   Linking of length scales

To model physical phenomenon, multiscale models incorporate individual models at different length and time scales. These individual models have been connected, or linked, by nine different approaches in the literature, as documented by McDowell (2010). To link a continuum model at a finer length scale to a continuum model at a coarser length scale, two common approaches are the concurrent and hierarchical approaches to multiscale modeling. Concurrent multiscale models simultaneously solve the balance and constitutive laws framed at different length scales, relying on shared boundaries to pass information from one length scale to another (Ghosh, Lee, & Raghavan, 2001; Kouznetsova et al., 2002). A significant drawback of concurrent multiscale modeling is the increased computational resources required. On the other hand, hierarchical multiscale models simulate the response at different length scales independently of each other, allow more rapid and parallelizable computations (Carrere et al., 2004; McVeigh et al., 2006). The challenge for hierarchical modeling is the linking of the length scales.

Luscher, McDowell, and Bronkhorst (2010) recently proposed an approach to linking different length scales within a hierarchical multiscale model, namely the invariance of mass, momentum, dissipated energy, and stored energy between length scales. Kinematic consistency is maintained between length scales with second-gradient continua at the fine and coarse length scales. A numerical example involving a two-phase microstructure without interfaces indicates the utility of this approach (Luscher, 2010).

For cementitious material systems, there have been several documented multiscale models concerning the determination of material properties. For example, Garboczi and Bentz (1998) utilize a two-scale model at micrometer and millimeter length scales to calculate the effective diffusivity of a concrete system with account of the evolution of hydration products. Bernard, Ulm, and Lemarchand (2003) proposed a four-scale model with length scales ranging from to estimate the early-age time-dependent properties of elastic modulus, solid percolation threshold, and Poisson's ratio of hydrated cement as a function of the volume fractions of the different phases.

There are fewer examples in the literature of multiscale models that consider initial-boundary-value problems. Maekawa, Ishida, Kishi (2003) simulated the life-span of rebar-reinforced concrete structures via a concurrent two-scale model. The fine length scale is constructed using the work of Maekawa, Chaube, and Kishi (1999), who considered thermal conservation as well as conservation of mass and transport of water (H_2O), chloride ions $(Cl-)$, oxygen (O_2), calcium ion (Ca_2+), carbon dioxide (CO_2), and chrome (Cr) to estimate local material properties. The local material properties, i.e., strength, stiffness, temperature, water content, and pore pressure, are then used within a hand-shaking scheme to transition to the coarse length scale. The coarse length scale consists of a 3D finite element model utilizing Galerkin's method of weighted residual functions to determine fracture due to local material properties and globally applied boundary conditions (Maekawa, Okamura, & Pimanmas, 2003). The influence of fracture on the transport of mass, e.g., water and chloride ions, is considered by passing the degree of damage from the coarse length back to the fine length scale.

Kabele (2007) presented a hierarchical multiscale framework for modeling the fracture of high performance fiber reinforced cementitious composite beams in shear loading. The four length scales – structural, distributed multiple cracks, individual cracks, and phenomenological microscale of individual fibers – are linked through spatial averaging of a representative volume element (RVE) based on overall stress and overall deformation of the RVE.

2.6 Inverse materials design

Historically, a trial-and-error materials development process required upward of 20 years to determine the right combination of processing steps leading to the microstructures and properties that satisfied the desired performance level. This problem motivated Olson (1997) to clarify the simultaneous deductive mappings and inductive decision path necessary for material design. The deductive mappings are a set of bottom-up cause-and-effect relations; the inductive decision path searches for properties, microstructures, and processes that satisfy the one or more desired performance requirements.

Adopting the nomenclature of Chen et al. (1996), variables in design problems can be classified as either design, noise, or response. Design variables, also referred to as input or control variables, are variables which a designer may control either the central tendency, the distribution, or the central tendency and the dispersion of the values. Noise variables are variables affecting the response of a system, but are beyond a designer's control (McDowell et al., 2009b). The input and noise variables are inputs to a system

model, which generates responses in terms of response variables. Together, the input, noise, and output variables and the system model define a system.

The inverse design problem is to determine preferred sets of inputs which combine to produce the desired responses. The solutions may be either optimal or robust. Optimal solutions seek to determine values of input variables which produce a maximal or minimal value of one or more response variables. Robust solutions, introduced by Taguchi (1986), seek to determine values of input variables such that the response variables are insensitive to variation, or uncertainty. Here, three types of robust solutions are classified. Type I robust solutions (Taguchi, 1986) seek to determine values of input variables which produce responses that are insensitive to uncertainty of noise variables. Type II robust solutions, proposed by Chen et al. (1996), laid the foundation for propagated uncertainty analysis by seeking the desired performance level while minimizing variation due to control factors. Type III robust solutions (Choi et al., 2005a) minimize variation in the performance due to the uncertainty inherent to the model.

Choi et al. (2008) classified robust design approaches as either "all-in-one" or "multilevel" approaches. In all-in-one robust approaches (Du & Chen, 2002), the system boundary is relatively large and may encompass multiple internal variables, yet the designer only deals with input and output variables. Any intermediate variables, defined as variables that serve as the output variable of a lower level and an input variable to a higher level, are within the system. As noted by Choi et al. (2008), the all-in-one robust approach requires models within a multiple model chain to be computationally or mathematically interfaced, thus constructing a single system. Because all levels are interfaced into a single model, traditional sampling strategies such as Monte Carlo

sampling (e.g., Choi, Grandhi, & Canfield, 2007) and Latin HyperCube sampling (e.g.,

Helton & Davis, 2003) may be used to determine the variation in the response of the

system. Because multiple model chains must be interfaced, the all-in-one approach is

disadvantageous for models existing on heterogeneous computational platforms,

problems which require intermediate decisions, and complex systems (Choi et al., 2008).

The advantage of all-in-one approaches is that propagated error between levels is handled

within the all-in-one model.

Multilevel approaches split the system into multiple levels, thus creating a chain

of systems. The systems within a multilevel approach are connected through

intermediate variables, which function as response variables at lower levels of hierarchy

and input variables at higher levels of hierarchy. The multilevel approaches in the

literature can be divided into approaches that do and do not consider uncertainty.

Approaches not considering uncertainty, pioneered by Schmit and Mehrinfar (1982) and

Sobieszczanski-Sobieski et al. (1987), rely upon higher-level optimizations calling

multiple lower-level optimizations. Multilevel approaches considering uncertainty have

been introduced for the worst case propagated uncertainty (Gu et al., 2000), generic

probabilistic approaches (Du & Chen, 2002), probabilisitc analytical target cascading

(Liu et al., 2005), and the Inductive Design Exploration Method (IDEM) (Choi et al.,

2008).

Robust inverse algorithms can also be classified by the number of response

variables, either univariate or multivariate (Murphy, Tsui, & Allen, 2005). Robust

inverse algorithms for univariate systems, or systems with one response variable, have

been determined via either loss functions with two-step methods or utility function

approach. The loss function with two-step methods, introduced by Taguchi (1986), assigns a loss function to quantify the loss associated with a value of a response variable deviating from a target. The loss function can then be minimized by determining the maximum signal-to-noise ratio. In contrast to the loss function approach, the utility function approach (Harrington, 1965) assigns an expected utility value based on values of input variables.

For inverse design problems involving multivariate responses, Murphy, Tsui, and Allen (2005) review three approaches for determining preferred values of input variables. The first approach, the additive combination of univariate loss functions (e.g., Pignatiello, 1993), searches for robust solutions to multivariate design problems by summing individual univariate loss functions to make a multivariate loss function which may be minimized. The second approach, the multiplicative combination of univariate utility functions, seeks to minimize the product of the geometric average of univariate utility functions. The third approach, the compromise Decision Support Problem (cDSP) (e.g., Mistree, Hughes, & Bras, 1993), determines the values of design variables to achieve conflicting goals to the best extent possible while satisfying a set of constraints.

For computational materials design across multiple levels, McDowell et al (2009b) recommend the use of robust inverse design algorithms due to natural, model parameter, model structure, and propagated uncertainty, as described by Isukapalli, Roy, & Georgopoulos (1998).

CHAPTER 3:

HIERARCHICAL MULTISCALE MODEL SIMULATING THE RESPONSE OF A UHPC PANEL TO BLAST LOADING

The hierarchical multiscale model to simulate blast loading consists of three length scales as shown in Figure 3. At the smallest length scale, labeled "Level 2," a three-dimensional finite element model simulates a single fiber pulled from a cementitious matrix. The model accounts for material properties of the fiber, ITZ, and the matrix, as well as the fiber's length, cross-sectional shape, and helical twisting along the fiber axis. An example of helical twisting is shown in the "Fiber Detail" view. The right half of the fiber is not modeled due to symmetry. Details of the model and results generated by the model are presented in Section 3.2.

The next length scale, labeled "Level 1," is a Matlab® model simulating the tensile response caused by multiple fibers at a predefined crack within a cementitious matrix. Figure 3 shows fibers crossing the predefined crack plane in red; the remaining fibers are shaded out for clarity. The model accounts for fiber volume fraction, V_{fiber}, fiber orientation to the crack plane, and each fiber's pullout response calculated from the single fiber length scale. Results from this model include the quasi-static maximum tensile strength and the dissipated energy density. Details of the model and results generated by the model are presented in Section 3.3.

The coarsest length scale, labeled "Level 0," is a three-dimensional finite element model simulating the response of a UHPC panel subject to blast loading. The model

accounts for dynamic loading conditions, dynamic material properties, and a distribution of the material's dynamic properties, as shown by the spectrum of red from light pink to dark red indicating lower and higher values of interfacial tensile strengths. The gray bars at the top and bottom of the panel are steel restraints used as boundary conditions. Details of the model and results generated by the model are presented in Section 3.4.
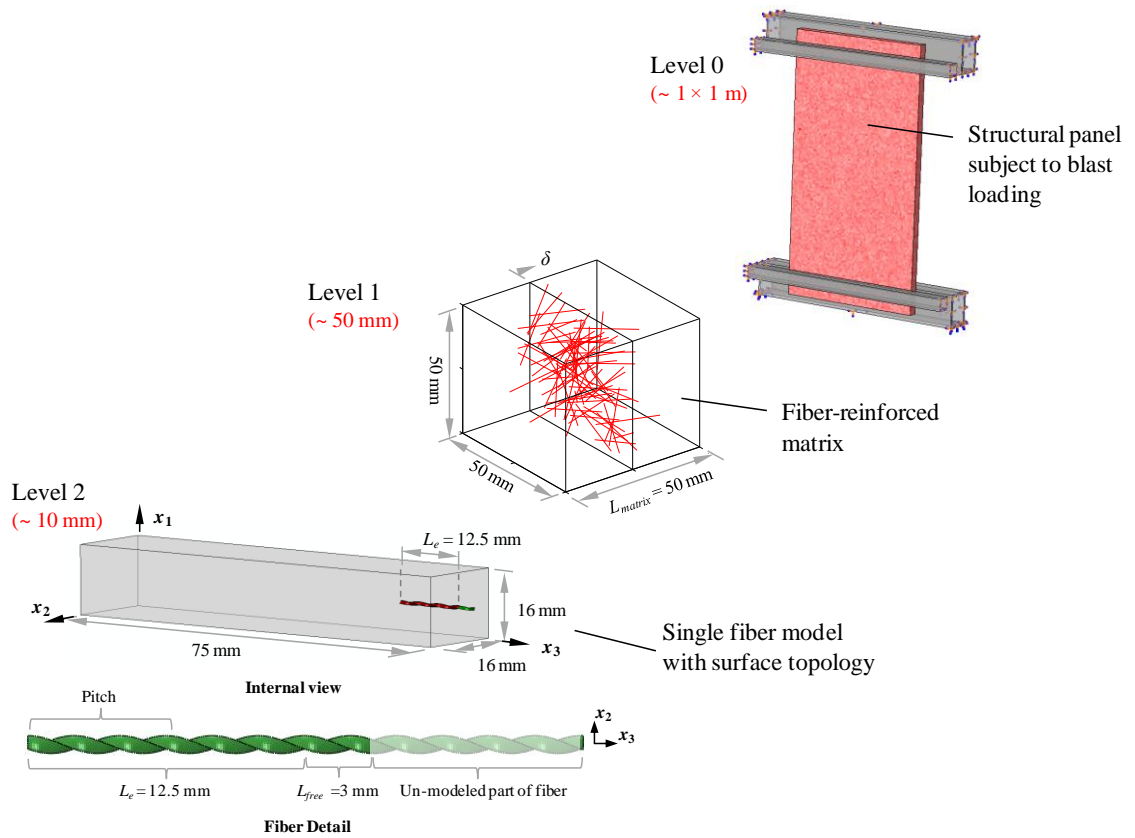
Figure 3.   Hierarchical multiscale models for UHPC subjected to blast loading.

3.1   Constitutive Framework

The model considers finite deformation. A material point initially at a fixed reference coordinate $\underset{\sim}{x}$ moves to a deformed coordinate $\underset{\sim}{x}^{*}$. The mapping between $\underset{\sim}{x}^{*}$ and $\underset{\sim}{x}$ is

35

specified by the displacement vector $\underset{\sim}{u} = \underset{\sim}{x}^* - \underset{\sim}{x}$. The deformation gradient is defined by

$\underset{\sim}{F} = \dfrac{\partial \underset{\sim}{x}^*}{\partial \underset{\sim}{x}}$. For elastic-plastic materials, the deformation gradient is multiplicatively

decomposed via $\underset{\sim}{F} = \underset{\sim}{F}^e \cdot \underset{\sim}{F}^n$, where $\underset{\sim}{F}^e$ and $\underset{\sim}{F}^n$ are the elastic and inelastic deformation

gradients, and $\cdot$ represents the inner product (i.e., $\underset{\sim}{A} \cdot \underset{\sim}{B} = A_{ij} B_{jk}$). The deviatoric stress $\underset{\sim}{S}$

is defined by $\underset{\sim}{S} = \underset{\sim}{\sigma} + p\underset{\sim}{I}$, where $\underset{\sim}{\sigma}$, p, and $\underset{\sim}{I}$ are the Cauchy stress tensor, the

hydrostatic pressure, and the second rank identity tensor, respectively. The pressure is

given by $p = -\tfrac{1}{3}\underset{\sim}{\sigma} : \underset{\sim}{I}$, where $:$ is the scalar product (i.e., $\underset{\sim}{A} : \underset{\sim}{B} = A_{ij} B_{ij}$). All tensors are

indicated with tildes underneath the tensor (e.g., $\underset{\sim}{u}, \underset{\sim}{F}$). In general, first rank tensors are

indicated with lower case letters; second and higher rank tensors are indicated with upper

case letters.

3.1.1 *Constitutive Relations - Matrix*

The matrix is represented by a pressure sensitive and strain-rate insensitive

extended Drucker-Prager constitutive relation included in Abaqus/Explicit v6.10 (2010).

The extended Drucker-Prager constitutive relation assumes the yield condition

$$F = t - p\tan(\beta) - d \leq 0, \tag{1}$$

where

$$t = \frac{1}{2}q\left[1 + \frac{1}{K} - \left(1 - \frac{1}{K}\right)\left(\frac{r}{q}\right)^3\right]. \tag{2}$$

Here, β is the internal friction angle in the meridional stress plane, and d is the

cohesion of the material under pure shear. In Eq. (2), q is the Mises equivalent stress

defined by $q = \sqrt{\frac{3}{2}(\underset{\sim}{S} : \underset{\sim}{S})}$, K is the ratio between the yield stress in triaxial tension and

the yield stress in triaxial compression and must be in the range $0.778 \leq K \leq 1.0$, and r is

the third invariant of the deviatoric stress defined by $r = \left(\frac{9}{2}\underset{\sim}{S} \cdot \underset{\sim}{S} : \underset{\sim}{S}\right)^{\frac{1}{3}}$. Setting $K = 1$

allows the original Drucker-Prager (1952) yield condition to be recovered due to the lack

of dependence on the third invariant of deviatoric stress. The von Mises yield condition

is recovered when $K = 1$ and $\beta = 0$.

When the yield condition is satisfied (i.e., $F = 0$), a non-associative material

yields according to the flow rule

$$\underset{\sim}{D}^p = \frac{\dot{\bar{\varepsilon}}^p}{c} \frac{\partial G}{\partial \underset{\sim}{\sigma}}, \tag{3}$$

where $\underset{\sim}{D}^p$ is the plastic part of the rate of deformation tensor, $\dot{\bar{\varepsilon}}^p$ is the equivalent

plastic strain rate defined by $\dot{\bar{\varepsilon}}^p = \sqrt{\frac{2}{3}\underset{\sim}{D}^p : \underset{\sim}{D}^p}$, c is a constant defined by

$c = 1 - \frac{1}{3}\tan(\psi)$, G is the flow potential

$$G = t - p\tan(\psi), \tag{4}$$

and ψ is the dilation angle.

A cementitious matrix is considered with a mass density, ρ_m, of 2.4 g/cm^3 and an

unconfined compressive strengths, f_m, of 44 MPa. The elastic stiffness of the

cementitious matrix, E_m, is calculated using the empirical relation

$$E_m = 2.15 \times 10^4 \left(\frac{f_m}{10}\right)^{1/3} \tag{5}$$

where f_m is specified in MPa. Equation (5) is from CEP-FIP Model 1990 (1998), which

is valid for normal weight concrete containing quartz aggregate and 28-day unconfined

compressive strengths less than 80 MPa (Mehta & Monteiro, 2005). For $f_m = 44$ MPa,

the calculated elastic stiffness values is 35.2 GPa. Possible softening of the matrix during

large deformations is not considered.

   The ratio of the yield stress in triaxial tension to the yield stress in triaxial

compression and the internal friction angle are assumed to be $K_m = 0.8$ and $\beta_m = 28°$, as

determined by Park, Xia, and Zhou (2001). The dilation angle is used as a calibration

coefficient to fit the model to experimental data presented in Sujivorakul (2002). The

choice of possible dilation angles is guided by Vermeer and de Borst (1984), who showed

that the $\psi < \beta$ in all cases and observed that the dilation angles of concrete are between

0 and 20. From the calibration, the dilation angle of the cementitious matrix is set to a

constant value of 2°. Table 2 summarizes the material parameters used for the two

different cementitious matrices considered.

Table 2. Material parameters used for cementitious matrix.

f_m MPa	ρ_m g/cm^3	E_m GPa	K_m	β_m °	ψ_m °
44	2.4	35.2	0.8	28	2

3.1.2 Constitutive Relations - Interfacial Transition Zone (ITZ)

The constitutive relations for the ITZ follow those of the cementitious matrix except that elastic stiffness of the ITZ, E_{ITZ}, is reduced based on the work of Simeonou and Ahmad (1995) and Cohen, Lee, and Goldman (1995). Simeonou and Ahmad (1995) compared the elastic stiffness of concrete predicted by Hashin-Shtrikman limits (Hashin & Shtrikman, 1963) for a two-phase composite of aggregate and cementitious matrix to the experimentally measured elastic stiffness's published by five different researchers. The concretes were NSCs sans silica fume made with w/cm ratios between 0.3 and 0.6. Results indicate that the measured elastic stiffness of concrete, E_c, falls within the Hashin-Shtrikman limits for w/cm ratios less than 0.41. However, for w/cm greater than or equal to 0.41, the measured E_c is less than the Hashin-Shtrikman lower limit. Thus, a third more compliant phase is present in the microstructure. Using a three-phase Hashin-Shtrikman model (Hashin, 1992), Simeonou and Ahmad (1995) calculated that the elastic stiffness of ITZ is 25% to 50% that of the elastic stiffness of the matrix for an assumed 20 μm thickness. The three-phase Hashin-Shtrikman model assumes spherical aggregate with a uniform ITZ thickness.

Cohen, Lee, and Goldman (1995) measured the dynamic moduli of elasticity of four mixtures: Portland Cement mortar, Portland Cement paste, a blended mortar with 10% of the Portland Cement replaced with silica fume, and a blended paste with 10% of the Portland Cement replaced with silica fume. All four mixtures had a w/c ratio of

0.52. The elastic modulus of ITZ, E_{ITZ}, was calculated using the logarithmic rule of mixtures, i.e.,

$$E_{mortar} = \left(E_{sand}\right)^{V_{sand}} \left(E_{paste}\right)^{V_{paste}} \left(E_{ITZ}\right)^{V_{ITZ}},$$ (6)

where E is the measured dynamic moduli of the four constituents –mortar, sand, paste, and ITZ – and V is the volume fraction of the constituent. The ratios of E_{ITZ}/E_{paste} are shown in Table 3.

Table 3. Calculated E_{ITZ}/E_{paste} ratios as a function of assumed ITZ thickness using logarithmic rule of mixtures (Cohen et al., 1995).

Material	t_{ITZ} (μm)	E_{ITZ}/E_{paste}
	50	0.75
100% PC	30	0.59
	10	0.15
	50	0.88
10% SF + 90% PC	30	0.80
	10	0.48

In the model at the single fiber length scale, it is assumed that $t_{ITZ} = 50$ μm and that $E_{ITZ}/E_{paste} = 0.80$. The assumed value of t_{ITZ} is driven by modeling convenience, resulting in larger values for the minimum characteristic element size.

The dilation angle in the ITZ, ψ_{ITZ}, is used as a calibration constant and assumed to have a more restrictive upper bound than the bounds defined in Section 3.1.1, namely $\psi_{ITZ} \leq \psi_m$. Calibration of the model indicates that $\psi_{ITZ} = 1$.

3.1.3 Constitutive Relations - Fiber

The fiber is assumed to be an elastic-plastic pressure- and rate-independent

material. Yielding of the fiber is assumed to follow the Von Mises yield criterion, i.e.,

$$F(\underset{\sim}{\sigma},\underset{\sim}{\alpha},\sigma^o) = \sqrt{\frac{3}{2}\left(\underset{\sim}{S}-\underset{\sim}{\alpha}^{dev}\right):\left(\underset{\sim}{S}-\underset{\sim}{\alpha}^{dev}\right)} - \sigma^o = 0, \tag{7}$$

where $\underset{\sim}{S}$ is the previously defined deviatoric stress tensor, $\underset{\sim}{\alpha}$ is the back stress tensor,

$\underset{\sim}{\alpha}^{dev}$ is the deviatoric part of the back stress tensor defined as $\underset{\sim}{\alpha}^{dev} = \underset{\sim}{\alpha} - \frac{1}{3}\underset{\sim}{\alpha}:\underset{\sim}{I}$, and σ^o

is the yield stress. The yield surface evolves through the evolution of the back stress

tensor, i.e.,

$$\dot{\underset{\sim}{\alpha}} = \frac{C}{\sigma^o}\left(\underset{\sim}{\sigma}-\underset{\sim}{\alpha}\right)\dot{\bar{\varepsilon}}^{pl} - \gamma\underset{\sim}{\alpha}\dot{\bar{\varepsilon}}^{pl}, \tag{8}$$

where C and γ are material parameters and $\dot{\bar{\varepsilon}}^{pl}$ is the equivalent plastic strain rate

defined as $\dot{\bar{\varepsilon}}^{pl} = \sqrt{\frac{2}{3}\dot{\underset{\sim}{\varepsilon}}^{pl}:\dot{\underset{\sim}{\varepsilon}}^{pl}}$. Because the inelastic flow is assumed to be associative,

the evolution equation for plastic strain is given by

$$\dot{\underset{\sim}{\varepsilon}}^{pl} = \dot{\lambda}\frac{\partial F}{\partial \underset{\sim}{\sigma}}, \tag{9}$$

where $\dot{\lambda}$ is the plastic multiplier obtained from the consistency condition $dF = 0$.

Damage initiation and damage evolution are not considered.

The fiber density, ρ_f, elastic stiffness, E_f, and Poisson ratio, ν_f, are assumed to

be 7.85 g/cm^3, 190 GPa, and 0.33. The remaining material parameters were determined

from monotonic uniaxial tensile data of a non-twisted triangular fiber reported in

Sujivorakul (2002). The triangular fiber was manufactured by shaping music wire,

initially with a round cross section and confirming to ASTM A228 (2007). The

41

triangular shape is approximately the shape of an isosceles triangle with an equivalent

diameter, ϕ_e, of 0.5 mm. Here, the equivalent diameter is defined as $\phi_e = A_{fiber}/\pi$,

where A_{fiber} is the cross-sectional area of the triangular fiber.

Figure 4 compares the engineering stress as a function of engineering strain for

experimental data and numerical simulations of a uniaxial monotonically loaded

triangular shaped fiber which was not twisted prior to testing. In Figure 4, the black line

represents the experimentally observed behavior presented by Sujivorakul (2002), the red

dashed line represents the engineering stress-engineering strain behavior of numerical

simulations. The calibration constants used were $C = 260$ GPa, $\sigma^o = 1.15$ GPa, and

$\gamma = 195$.
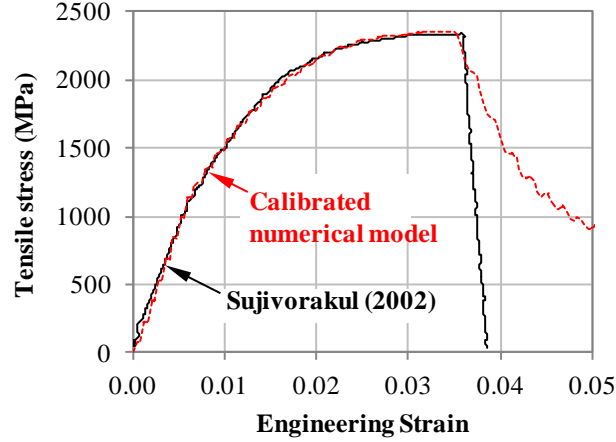
Figure 4.   Comparison of experimental (solid black) and simulation (dashed red) stress-strain data for monotonically loaded tensile specimens. The fibers have a cross section in the shape of an isosceles triangle with $\phi_e = 0.5$ mm. The gage length for the experimental data is unknown; the gage length for the numerical simulation is 25.4 mm.

3.1.4   Constitutive Relations - Interfacial Friction

A rate-independent, isotropic Coulomb friction law is employed. In this model, relative motion between two surfaces is allowed when the equivalent shear stress

$$\tau_{eq} = \sqrt{\tau_1^2 + \tau_2^2} \tag{10}$$

reaches or exceeds the critical stress

$$\tau_{crit} = \mu p_{contact}, \tag{11}$$

where τ_1 and τ_2 are mutually orthogonal shear stresses at the interface, μ is the coefficient of friction, and $p_{contact}$ is the normal contact pressure between the two surfaces. Because the model is assumed to be isotropic, the magnitudes of the shearing rates

43

$$\dot{\gamma}_1 = \sqrt{\dot{\gamma}_1^2 + \dot{\gamma}_2^2}\ \frac{\tau_1}{\tau_{eq}}\ \ \text{and}$$

$$\dot{\gamma}_2 = \sqrt{\dot{\gamma}_1^2 + \dot{\gamma}_2^2}\ \frac{\tau_2}{\tau_{eq}}$$

(12)

are proportional to the shear stresses τ_1 and τ_2.

The coefficient of Coulomb friction is determined from the experiments of Baltay and Gjelsvik (1990), who found that the coefficient of friction between steel and concrete depends on the surface finish of the steel. For machined surfaces, the mean coefficient of friction is measured over the range of normal pressures from 13.8 kPa to 55 MPa. Although Baltay and Gjelsvik (1990) assigned a mean value of 0.47, the data for machined steel surfaces indicate a parabolic response with the maximum value of $\mu =$ 0.58 for a normal stress of 3.4 MPa and a minimum value of $\mu = 0.35$ for $p_{contact} \le 3.4$ MPa and $p_{contact} \ge 55$ MPa. For steel surfaces with mill scale, Baltay and Gjelsvik (Baltay & Gjelsvik, 1990) reported that the coefficient of friction is 0.2 for $p_{contact} = 10$ kPa and increases to 0.53 for $p_{contact} = 34.5$ MPa. In this work, a pressure-independent coefficient is assumed to be 0.45 at steel-ITZ interfaces.

For cementitious materials in contact with other cementitious materials, the American Concrete Institute ACI 381 (2008a) recommends higher pressure-independent coefficients of friction, namely 1.0 for normal-weight concrete placed against another hardened concrete with an intentionally roughened surface, and 1.4 for cementitious surfaces formed within a monolithically placed structure. In this work, a pressure-independent coefficient is assumed to be 1.05 at interfaces formed as a result of fracture within cementitious materials.

3.2   Model at the single fiber length scale

The model at the single fiber length scale is implemented in three dimensions with a single fiber embedded in a 50-μm-thick ITZ, which is then embedded within a cementitious matrix. Figure 5 shows a sample instantiation of the reference configuration of the model with the matrix shaded in gray, ITZ shaded in red, and fiber shaded in green. In Figure 5, the triangular fiber has a 0.5-mm equivalent diameter, a 6.35-mm pitch, and a total length of 15.5 mm, of which 12.5 mm has been embedded into the matrix. The remaining 3 mm is classified as the free length, L_{free}, of the fiber. The numbers 1-6 in yellow rectangles define faces of the model for future reference. Relative displacements between the nodes on the external surface of the fiber and the nodes on the internal surface of the ITZ are permitted; however, relative displacements between the nodes on the external surface of the ITZ and the nodes on the internal surface of the matrix are not permitted.
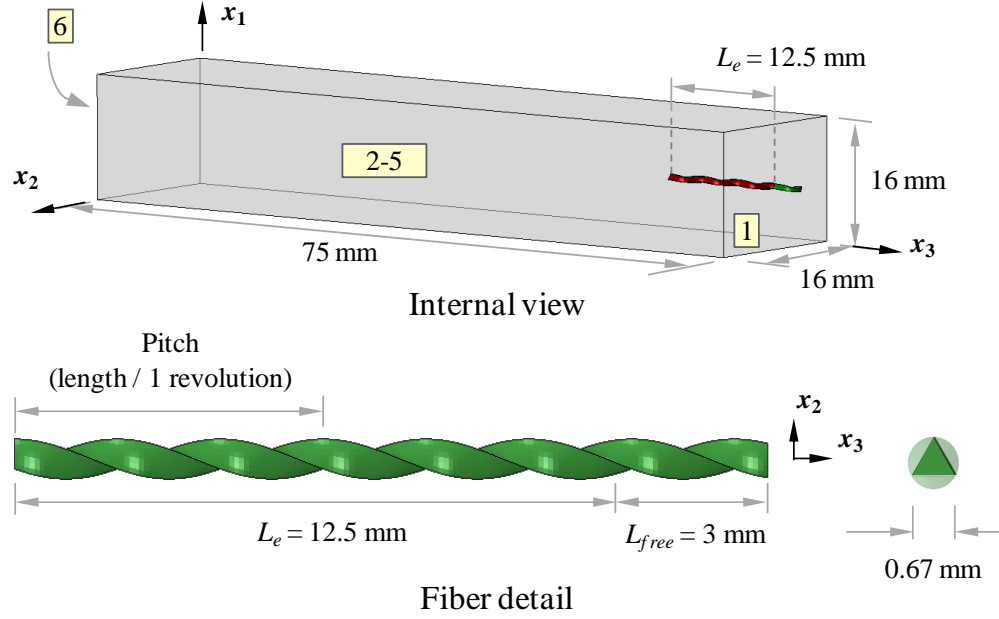
Figure 5.   Illustration of the model at the internal view showing the matrix (gray), ITZ (red), and fiber (green). The $\phi_e = 0.5$ mm triangular cross-section fiber has a pitch of 6.35 mm and total length of 15.5 mm, of which 12.5 mm was embedded into the cementitious matrix.

All fibers are assumed to have cross sections in the shape of isosceles triangles which are not warp as a result of the manufacturing process, equivalent diameters of 0.5 mm, and isotropic material properties. Furthermore, it is assumed that the fiber-ITZ and ITZ-matrix interfaces experience perfect geometrical contact (i.e., no voids or non-uniformity in bonding) in the reference configuration. Chemical adhesion between the fiber and the ITZ is not considered.

3.2.1   Boundary and Loading Conditions

The boundary conditions are applied in two steps. In the first step, face 1 of the fiber is fixed in the x_3 direction while the matrix and ITZ domains undergo an isotropic

volumetric reduction of 840 µm/m through a linear shrinkage of -280 µm/m in each of the three directions. Rigid body translation is prevented by fixing the center point of the fiber's positive x_3 face in the x_1 and x_2 directions. The choice of -280 µm/m linear shrinkage is based on the recommendation of CEB-FIB Model Code 1990 (1998) for the shrinkage of a cementitious composite after two days of curing in a normal hardening cement. The linear shrinkage is applied via a smooth step function prebuilt in Abaqus such that the linear shrinkage is 0 µm/m at 0 ms, -280 µm/m at 0.008 ms, and the partial derivative of shrinkage with respect to time is zero at 0 and 0.008 ms.

In the second step, the fiber is pulled from the ITZ and matrix. Matrix faces 1-5 are traction-free; face 6 of the matrix is fixed in the x_1, x_2, and x_3 direction. Face 1 of the fiber is pulled in the x_3 direction at a velocity that linearly increases via a smooth step function from 0 m/s at 0 ms to 10 m/s at 0.125 ms and remains constant thereafter. As it is being pulled from the ITZ and matrix, the fiber is prevented from rotating about the x_3 axis.

3.2.2 *Meshing and numerical algorithm*

Meshes were generated using Abaqus's (Dessault Systemes, 2010) native meshing algorithm. The matrix was meshed by 4-node tetrahedral elements using an unstructured, graduated mesh with a maximum characteristic element length of 1 mm at matrix faces 2-5 that decreased to 110 µm at the matrix-ITZ interface. The ITZ was meshed by 4-node linear tetrahedral elements, with a characteristic element length of 110 µm. The fiber was meshed by 8-node linear reduced integration hexahedral elements with a characteristic element length of 110 µm. The meshing resulted in approximately

90,000 matrix elements, 14,000 ITZ elements, and 4,000 fiber elements. It is noted that this numerical model is mesh sensitive: the mesh density alters the surface roughness at the fiber-ITZ interface, causing different levels of tractions during slip. The different levels of traction then lead to varying amounts of plasticity in the matrix and the ITZ. To account for mesh-sensitivity, the model is calibrated in Section 3.2.3.

Numerical results were calculated by Abaqus/Explicit v6.10-1 running on 40 AMD 2350QC processing cores. For instantiations with $L_e = 12.5$ mm, the processing time varied from 48 to 300 hours depending on the severity of contact and distortion of the ITZ and matrix elements.

3.2.3 *Model Calibration and Validation*

The model was calibrated to experimental data reported by Sujivorakul (2002), who reported pullout forces as a function of end slip for twisted fibers with triangular cross sections pulled from $f_c = 44$ MPa cement mortar. The fibers had been embedded 12.7-mm into the cement mortar. The two data sets chosen from Sujivorakul (2002) for calibration and validation had pitches of 12.7 and 38.1 mm.

In physical experiments, the free length of each fiber was minimized, leading to an unknown, yet positive distance between the face of the cementitious material and the point that the fiber was pulled from. This positive value of free length was not necessarily constant for the three fibers considered for calibration. In contrast, the numerical simulations assume a fixed free length of 3.0 mm unless specified otherwise.

The model was calibrated by adjusting the dilation angles of the matrix and the ITZ such that the pullout force as a function of end slip of the numerical simulation

48

matched that of the aforementioned physical experiments. Here, pullout force is defined

as the total traction in the positive x_3 direction on the x_3 face of the fiber (cf. Figure 5);

end slip is defined as the displacement in the x_3 direction of the x_3 face of the fiber with

the reference position taken from the reference configuration. Starting with the 12.7-mm

pitch fiber, dilation angles of 2º and 1º were chosen for the matrix and the ITZ.

Subsequently, the model was validated by simulating a fiber-ITZ-matrix system with the

same material parameters and a 38.1-mm fiber pitch. Results of the simulations

generated in this work and experimental data generated by Sujivorakul (2002) are

compared in Figure 6. In Figure 6, numerical data are shown as thin dashed lines shaded

red for the 12.7-mm pitch and blue for the 38.1-mm pitch. Data generated by physical

experiments are shown as thick solid lines and are shaded the same color as their

corresponding experimental data with the same pitch. For comparison, a third pair of

curves, shaded black, indicate data for straight, smooth fibers with 0.5-mm-diameter

circular cross sections. The dashed black line was generated using a numerical

simulation similar to the model shown in Figure 5, except that the fiber was straight and

smooth with a 0.5-mm-diameter cross section. The mesh at the fiber-ITZ interface of the

circular fiber had a characteristic element length of 55 μm, which is smaller than the

characteristic element length used for the twisted triangular fibers. It is assumed that the

need for the finer mesh is attributable to discretization errors introduced in three-

dimensional meshing. The thick solid black line corresponds to experimental

measurements in Sujivorakul (2002).
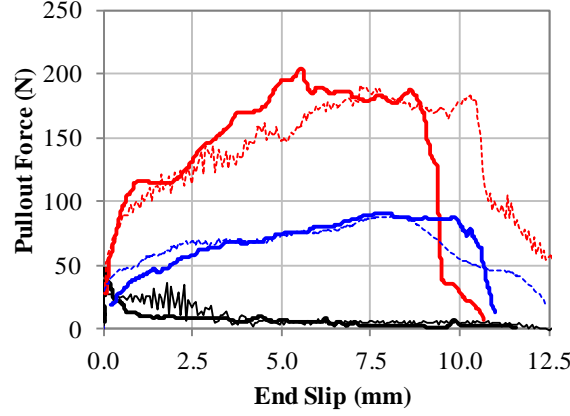
Figure 6.   Calibration curves for triangular fibers with initial pitches 12.7 (blue) and 38.1 (green) mm. The black pair of lines represent data for straight, smooth fibers with circular cross sections. Experimental data of Sujivorakul (2002) are shown as solid lines, and data from numerical simulations are shown as dashed lines.

Experimental and numerical results can also be compared by the maximum pullout force and the total work of pullout. Here, the total work is defined as the integral of pullout force integrated over the end slip for end slips between zero and L_e. Figures 7a and 7b compare the maximum pullout force and work during pullout for experimental data of Sujivorakul (2002) and the numerical simulations utilizing the model at the single fiber length scale. In Figure 7, data points representing experiments are shown as squares shaded red; data points representing numerical simulations are shown as circles shaded green. The two dashed lines at the bottom of each figure have a constant value, representing the value for a straight, smooth fiber. For the twisted fibers considered, the numerical simulation under-predicts the maximum pullout for by a maximum of 13%, and over-predicts the total work by 16%.

50

(a) Maximum pullout force   (b) Total work during pullout
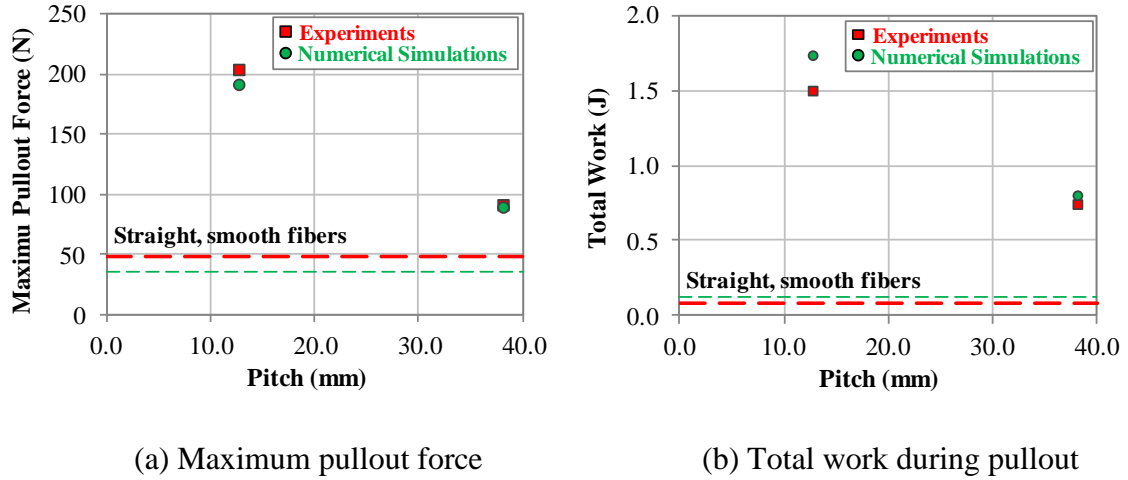
Figure 7.   (a) Maximum pullout force and (b) total work during pullout as functions of fiber pitch comparing data from experiments (Sujivorakul, 2002) (shaded red) and numerical simulations (shaded green) for $L_e = 12.5$ mm and $f_c = 44$ MPa. The two dashed horizontal lines at the bottom represent the value for a straight smooth fiber.

3.2.3.1   Replication of experimental phenomena

Although the mechanisms in the numerical simulations cause slip-hardening and matrix tunneling, it is not assumed that the numerical model presented here provides a unique solution predicting these phenomena. In lieu of an exhaustive analysis, Figure 8 compares the pullout forces as a function of end slip computed by the model utilizing different constitutive relations for the matrix and ITZ. The solid red curve indicates the pullout response of the elastic-plastic matrix and ITZ constitutive relations as described in Sections 3.1.1 and 3.1.2. In comparison, the dashed black line shows the pullout response of the model assuming a purely elastic response for the matrix and ITZ. At end slips less than 2 mm, the pullout responses are indistinguishable. However, for end slips between 2 and 12.5 mm, the pullout force of the model using purely elastic constitutive

relations for the matrix and ITZ displays slip-softening. Additionally, the elastic curve does not display any tunneling effects described previously.
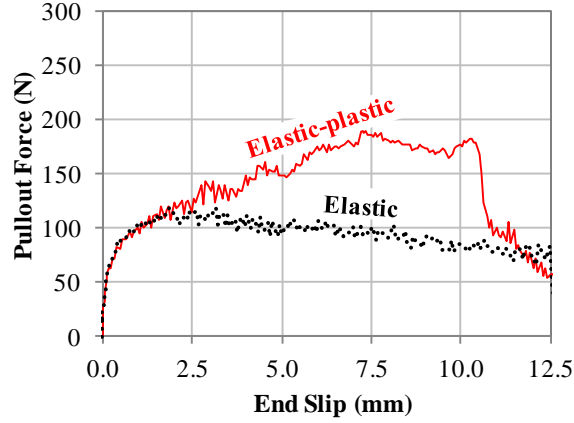
Figure 8.   Pullout force as a function of end slip for utilizing an elastic-plastic elastic ITZ-matrix (dashed black) and a elastic-plastic (solid red) ITZ-matrix system.

Beyond reproducing the experimental pullout curves, maximum pullout force, and total work, the model reproduces the untwisting of fibers during pullout. Here, untwisting is defined as the increase of a fiber's pitch from the initial pitch to a finite pitch greater than the initial pitch. To illustrate this phenomenon, Figure 9 shows the deformation and evolution of plastic strain of the outside of a 12.7-mm initial pitch fiber at end slip increments of 2.5 mm. For clarity, the ITZ and $f_c = 44$ MPa matrix surrounding the fiber are not shown; however, the positive x_3 face of the cementitious matrix is marked with a light gray vertical line. At each increment of end slip, the portion of the fiber within the cementitious material is to the left of the light gray line, and is marked as the "Embedded portion of fiber." In Figure 9, the image of the fiber at the top left of the figure represents the fiber's deformation and equivalent plastic strain after the matrix and ITZ have shrunk, but before the fiber has been pulled from the

matrix. The image of the fiber at the bottom right represents the fiber at an end slip of

12.5 mm. At an end slip of 12.5 mm, the fiber has been removed from the matrix, but has

not come to rest and may subsequently relax.
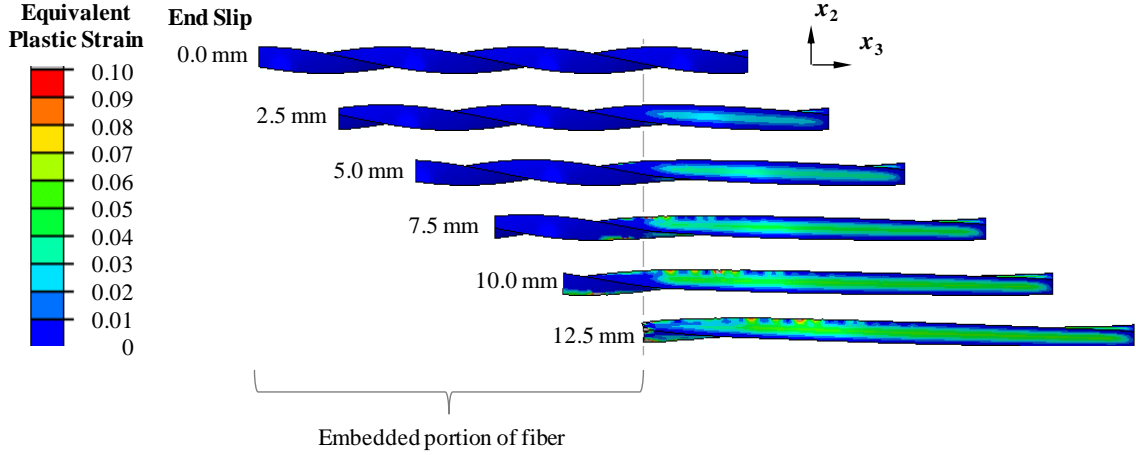
Figure 9.   Evolution of deformation and equivalent plastic strain as a function of end slip for a triangular fiber with an initial 12.7-mm pitch pulled from a $f_c = 44$ MPa matrix.

Similar to physical experiments, numerical simulations indicate that the fiber

untwists due to mechanical pullout from the matrix. From Figure 9, it is observed that

equivalent plastic strain primarily accumulates in longitudinal bands positioned at the

center of each of the three flats. The longitudinal bands extend from the free tip of the

fiber to the point at which the fiber exits the matrix. From this observation, it is

determined that the fiber exhibits primarily an elastic behavior within the matrix and ITZ.

On the triangular fiber shown, there are three such longitudinal bands with maximum

equivalent plastic strain values of 0.05.

3.2.4 Results

The numerical model focus was utilized to investigate dissipative mechanism active during fiber pullout, determine the behavior of a fiber at an in situ crack, and estimate the pullout response of twisted fibers from cementitious matrices with unconfined compressive strengths between 80 and 200 MPa..

3.2.4.1 Active mechanisms in the numerical model

In this section, mechanisms of the numerical model are investigated to gain insight into possible mechanisms in the physical experiments. In particular, the mechanisms of interest are the transfer of tractions at the fiber-ITZ interface, causes of the slip-hardening response and tunneling response, and the interplay of the different dissipation mechanisms.

The transfer of tractions at the fiber-ITZ interface can be observed in the evolution of σ_{33}, as seen in Figure 10 for a 12.7-mm pitch fiber. For reference, Figure 10 shows results of the same set of material properties and initial fiber geometries as the results shown in Figure 9. Similar to Figure 9, the ITZ and matrix surrounding the fiber have been removed for clarity and replaced with the farthest right vertical gray line marking the positive x_3 face of the matrix.
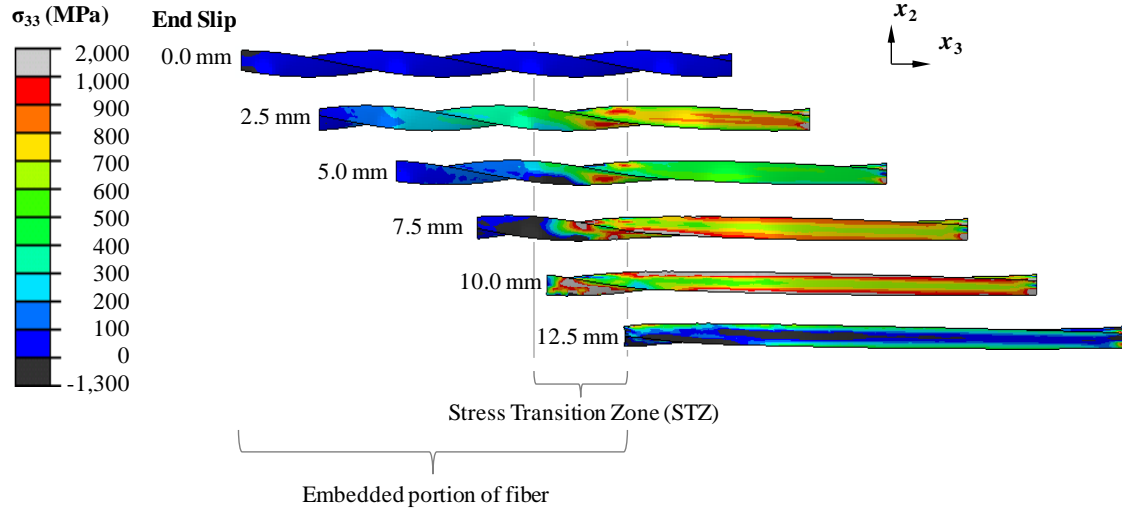
Figure 10. Evolution of σ_{33} as a function of end slip for a triangular fiber with an initial 12.7-mm pitch pulled from a $f_c = 44$ MPa matrix.

For end slips between 5.0 and 10.0 mm inclusive, there is of gradient of σ_{33} starting approximately 3 mm into the matrix and ending at the positive x_3 face of the matrix. In Figure 10, the location of the gradient is identified as the "Stress Transition Zone (STZ)." The function of the STZ is to transfer tractions from the twisted fiber to the matrix. For example, consider the distribution of σ_{33} along the x_3 axis shown in Figure 10 at an end slip of 5.0 mm.   At the left edge, or the beginning, of the STZ, $\sigma_{33} = 200$ MPa, whereas $\sigma_{33} = 500$ MPa at the right edge, or conclusion, of the STZ. The significance of the STZ is that a small domain of material controls the global response of the fiber. Although similar in name, the STZ is fundamentally different than the ITZ: STZ is an inhomogeneous region composed of fiber, ITZ, and bulk matrix with a location that can only be determined only after a crack plane in the matrix has been established.

The ITZ is a result of processing conditions and exists regardless of a crack plane in cementitious materials.

The slip-hardening and tunneling responses observed in Figure 6 are direct consequences of the STZ. For example, Figure 11 shows evolution of σ_{33} and the equivalent plastic strain in the ITZ and matrix as a function of end slip in a 12.7-mm-pitch fiber-ITZ-matrix system at a $x_1 = 0$ mm section view.
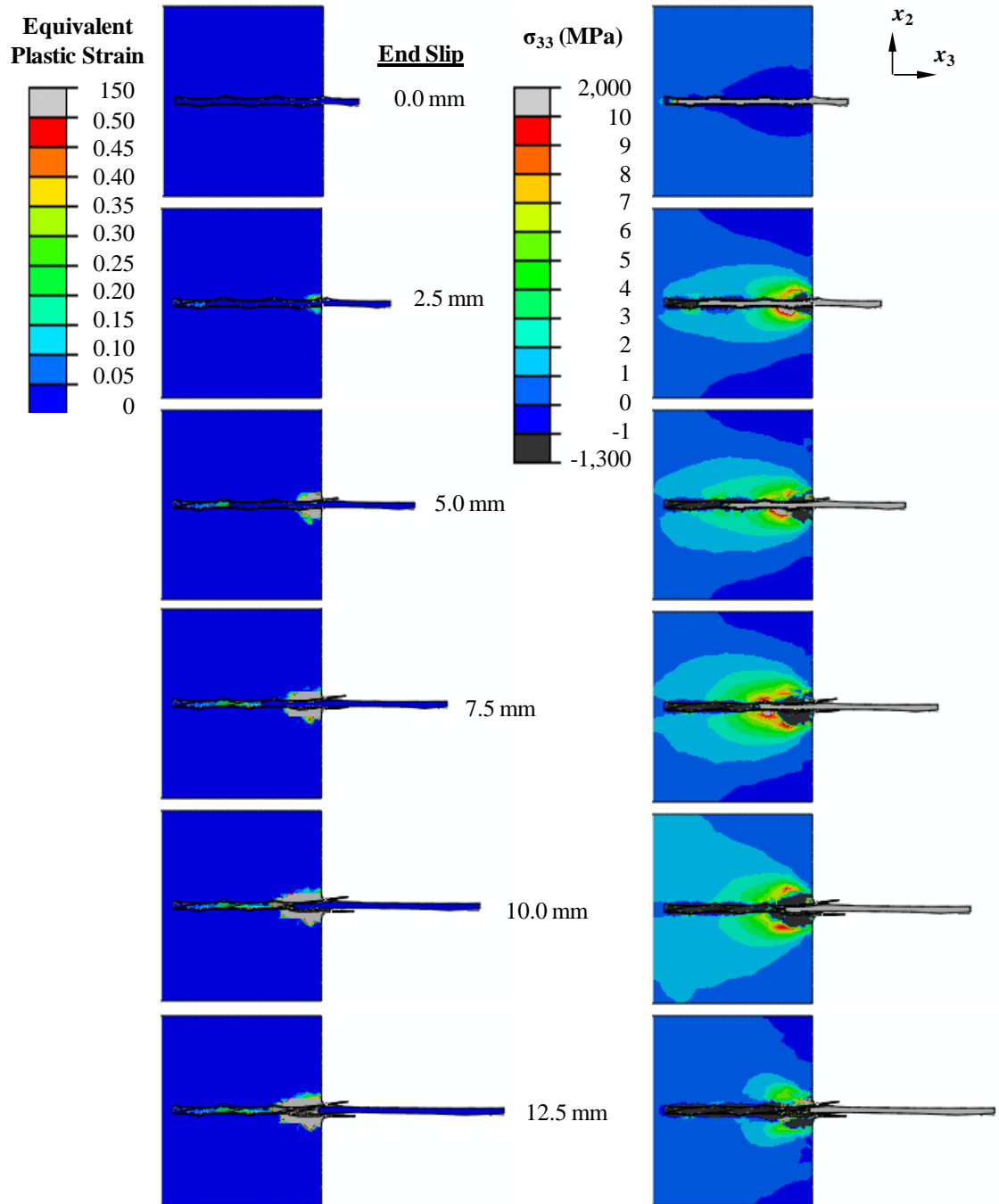
Figure 11. Evolution of equivalent plastic strain and σ_{33} as a function of end slip in the fiber-ITZ-matrix system. The fiber has a triangular cross section with a pitch of 12.7 mm and an embedded length of 12.5 mm in a $f_c = 44$ MPa matrix.

The equivalent plastic strains within the STZ in Figure 11 cause the numerical model to predict slip-hardening and tunneling via the following sequence of events. First, the ITZ plastically deforms via granular flow causing the matrix to dilate. The dilation of the ITZ leads to plastic deformation and dilation of the matrix within an approximate 1.25 mm radius of the fiber. This local dilation of the matrix is confined by regions of the matrix further from the fiber, ultimately causing the normal tractions at the fiber-ITZ interface to increase. The increase in the fiber-ITZ normal tractions increase frictional resistance via the isotropic Coulomb relations, which in combination with the plasticity of the ITZ and matrix, cause the observed slip-hardening.

The tunneling response is also a consequence of granular flow of the ITZ and matrix. For example, the granular flow and dilation of the ITZ and matrix elements leads to the erosion, or displacement from the fiber bed, of a small number of elements, as visible in Figure 11 for end slip values greater than or equal to 5.0 mm. After a sufficient number of ITZ and matrix elements erode, the fiber bed surrounding the matrix no longer remains in contact with the fiber, thus leading to tunneling.

Unlike physical experiments, numerical models allow the total work to be partitioned into different mechanisms. Figure 12 partitions the total work into friction, plastic dissipation of the combined fiber-ITZ-matrix system, and strain energy for systems containing 12.7- and 38.1-mm pitch fibers. The plastic dissipation of the combined system is further partitioned in Figure 13, which partitions total plastic dissipation into the plastic dissipation due to the granular flow of the ITZ, plastic deformation of the fiber, and granular flow of the matrix material.
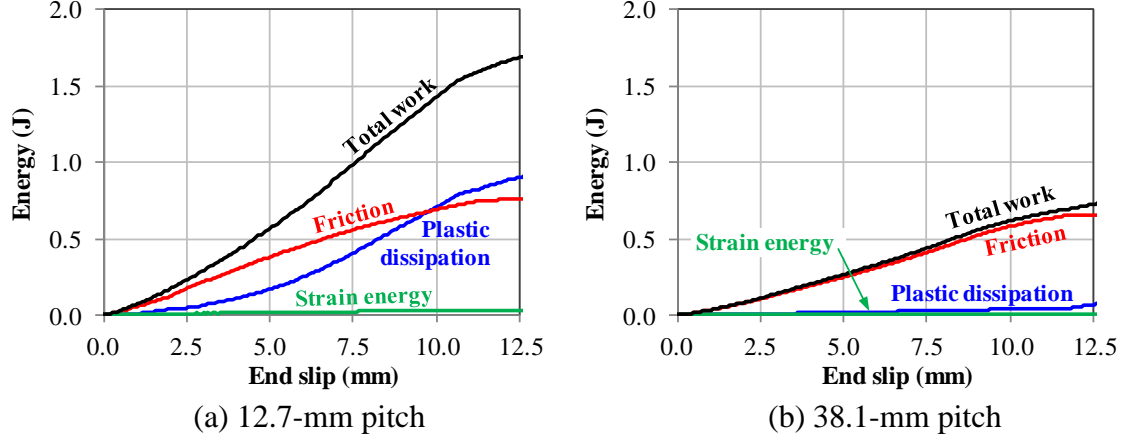
Figure 12. Partition of total work as a function of end slip for fibers with (a) 12.7-mm and (b) 38.1-mm pitches. Each fiber was embedded 12.5 mm into an ITZ-matrix system with $f_c = 44$ MPa.
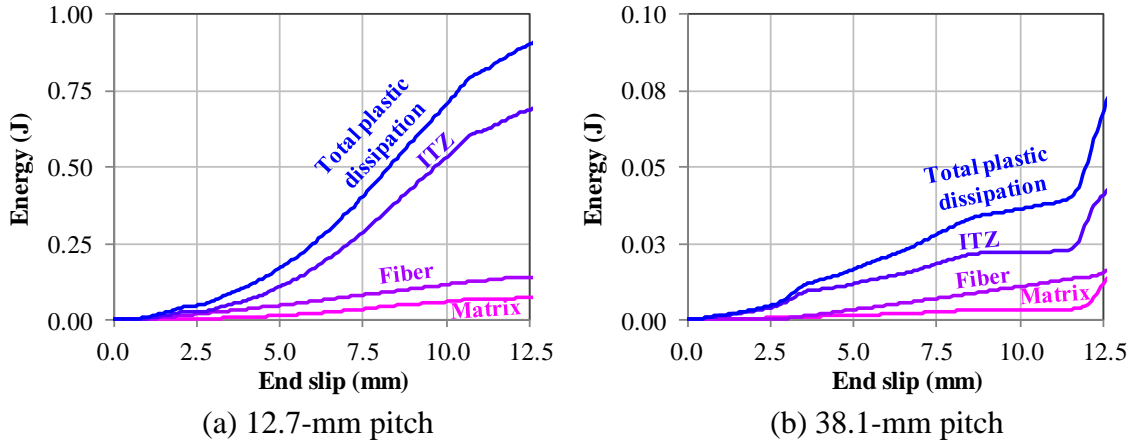
Figure 13. Partition of total plastic dissipation as a function of end slip for (a) 12.7-mm and (b) 38.1-mm pitched fibers. Each fiber was embedded 12.5 mm into an ITZ-matrix system with $f_c = 44$ MPa.

The work partitions shown in Figures 12 and 13 indicate that the model is highly dissipative, with less than 1% of the total work stored as strain energy. Of the remaining 99% of the total work, friction is the dominant energy dissipation mechanism during the

first 80% of end slip. This observation is significant in that both the numerical model

presented here and the analytical model presented by Sujivorakul (2002) primarily

account for pullout forces through frictional effects. The primary difference between the

models is that the numerical model accounts for increased pullout resistance by including

plasticity and dilation of the ITZ and matrix materials, instead of adding a torque

component to the embedded end of the fiber.

Interestingly, plastic dissipation of the 12.7- and 38.1-mm fibers accounts for only

8% and 2% of the total work within each respective system. To further explore this

observation, a numerical model was constructed of a 12.5-mm long, straight, triangular

shaped fiber utilizing the same constitutive relation given in Section 3.1.3. The straight

fiber was then twisted about its primary axis, i.e., the x_3 axis as shown in the Fiber Detail

view of Figure 5, in order to form twisted fibers with 12.7- and 38.1-mm pitches. The

positive x_3 face of the fiber was fixed; the negative x_3 face was rotated either 8.2 or 4.9

radians, depending on whether the final pitch was 12.7 or 38.1 mm, during a smooth step

function with a duration of 1 ms. During rotation, the negative x_3 face of the fiber was

permitted to translate in the x_3 direction. The fiber was then allowed to relax for 1 ms

before being untwisted the same number of radians as the fiber was previously twisted.

Note that the angle of applied twist, i.e., 8.2 or 4.9 radians, was greater than the final

desired twists of 2π or $\frac{2}{3}\pi$ for the 12.7- and 38.1-mm pitched fibers due to elastic

recovery.

The applied torque and work required to twist the straight fibers to pitches of 12.7

and 38.1 mm are shown in Figure 14. In Figure 14 torque data are shown as thin dashed

lines; data for the work, defined as the integral of the torque over the angle of twist, are

60

shown as solid lines. The numerically calculated torque values are slightly greater than

the theoretical fully plastic torque value of 35 N-mm, which is calculated by

$$T_0 = \frac{2}{3} \frac{\sigma_{yield}}{\sqrt{3}} \left(\frac{b}{2}\right)^3,$$ (13)

as determined by Chakrabarty (2006). In the preceding equation, σ_{yield} is the yield

strength of the fiber, i.e., 2,412 MPa, and b is the width of the fiber, i.e., 0.67 mm for the

$\phi_e = 0.5$ triangular shaped fiber shown in Figure 5. A comparison of the work required

to twist a triangular fiber, as shown in Figure 14, and the total work required to pull a

twisted fiber from a cementitious material, as shown in Figure 12, indicates that twisted

fibers require more work to be removed from a cementitious matrix than work to be

twisted.
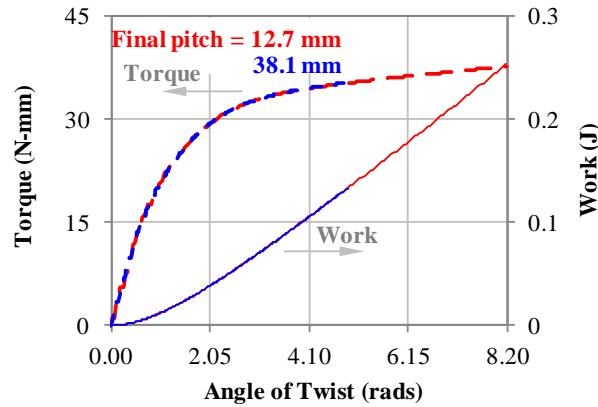
Figure 14. Applied torque and work required to twist fibers to 12.7- and 38.1-mm
           pitches. Fibers have ultimate tensile strengths of 2,412 MPa and lengths of
           12.5 mm.

3.2.4.2   Behavior of an in situ fiber at a crack face

Physical experiments are limited by the lack of control of all parameters. For example, the free length of the fiber, L_{free} , can be minimized in experiments, but never eliminated (cf. Figure 5). This specific limitation prevents researchers from experimentally determining the in situ behavior of twisted fibers at a crack face, where the fiber experiences a free length of 0 mm. In this section, the validated numerical model is utilized to gain insights into the pullout response at a crack face by simulating twisted fibers with zero free lengths.

Figures 15a and 15b show the pullout responses of 12.7- and 38.1-mm pitch fibers comparing the pullout force versus end slip data from experiments (solid line) to those generated by numerical simulations having 3.0- and 0.0-mm free lengths.

(a) pitch = 12.7 mm   (b) pitch = 38.1 mm
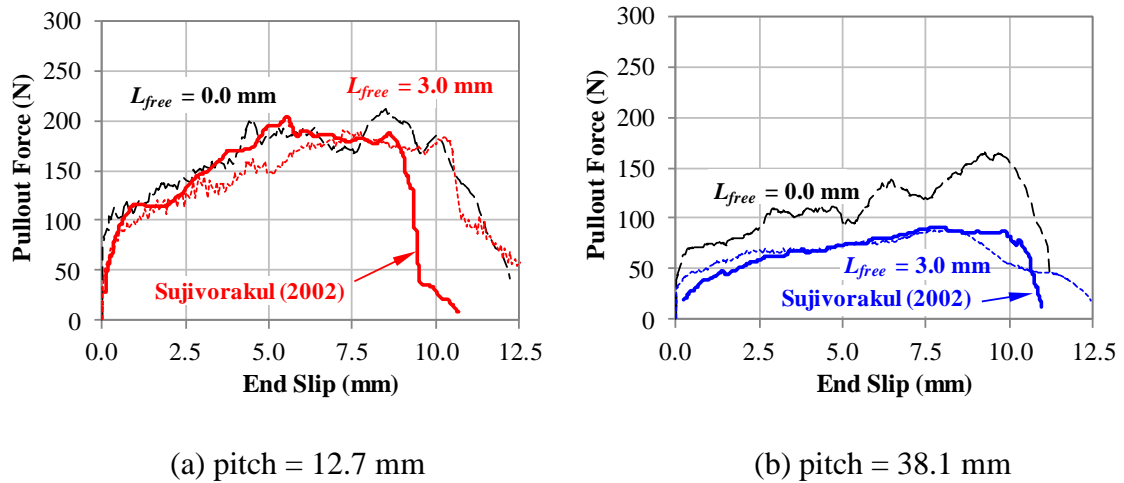
Figure 15.   The effect of free length of fiber quantified by the pullout force as a function of end slip for initial fiber pitches of (a) 12.7 mm and (b) 38.1 mm embedded in a $f_c = 44$ MPa matrix. Experimental data of Sujivorakul (2002) show as solid lines; numerical simulation data with L_{free} = 3.0 mm shaded the same color as the experimental data with dashed lines; numerical simulation data with $L_{free} = 0.0$ mm are shaded as black dashed lines.

The numerical simulations indicate that the effect of free length is more pronounced for the fiber's having larger initial pitches. In particular, the fiber with an initial pitch of 38.1 mm and L_{free} = 3.0 mm exhibits a maximum pullout force of 90 N; whereas the same fiber-ITZ-matrix system had a maximum pullout force of 165 N. This 83% increase in pullout force is not observed in the fiber-ITZ-matrix system with 12.7-mm pitch, which shows a more modest 17% increase in maximum pullout force. The primary significance of this finding is that experimental single fiber pullout tests provide a lower bound to the pullout forces experienced in-situ at a crack face.

3.2.4.3 *Extended model for mortars containing silica fume and higher unconfined compressive strengths*

For higher strength matrices, experimental data indicate that the pullout response changes from a slip-hardening response to either a slip-neutral or slip-softening response for end slips between 10 and 80% of the fiber's embedded length. Therefore, it is postulated that the previously identified STZ does not sufficiently dilate to increase the cause slip-hardening responses. Instead, the higher strength ITZs and matrices experience yielding and dilation such that either the slip-neutral or slip-softening behavior is present. For example, consider the experimental responses reported by Sujivorakul (2002) shown in Figure 16 for a 12.7-mm initial pitch fiber embedded 12.7 mm deep into two different matrices: $f_c = 44$ MPa and $f_c = 84$ MPa.
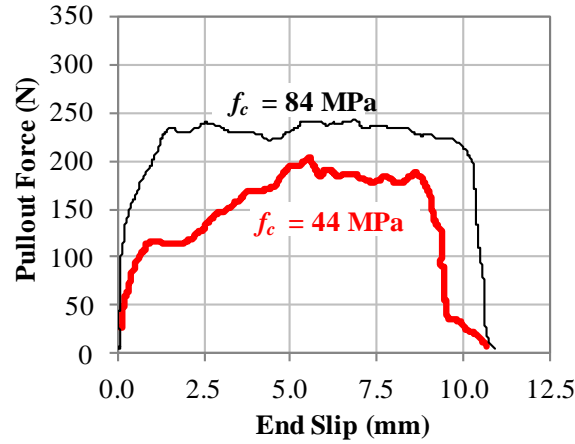
Figure 16. Experimentally measured pullout force versus end slip displacement for fibers with an initial pitch of 12.7 mm (adapted from Sujivorakul (2002)).

Recalling Figure 8, the numerical model predicts slip-hardening behavior if the ITZ and matrix are assumed to have purely elastic responses. This observation motivates the modeling of fiber-ITZ-matrix systems with higher strength matrices, such as the $f_c = 84$ MPa response in Figure 16. However, changing the matrix and ITZ to elastic constitutive relations with $E_m = 43.7$ GPa, $v_m = 0.2$, $E_{ITZ} = 35.0$ GPa, and $v_{ITZ} = 0.2$, and the linear shrinkage to -140 μm/m, per the CEB-FIB model code shrinkage estimates, under-predicts the pullout force at all end slips. A possible explanation for the under-prediction is found in the results of Chan and Chu (2004b), who showed cementitious material attached to straight, smooth circular fibers after being pulled from a cementitious material containing 30% silica fume by weight. The silica fume enhanced the chemical bond to the fiber, thus causing a fracture surface within the monolithically poured cementitious material. Therefore, the assumed 0.45 coefficient of friction at a steel-concrete interface is no longer valid; instead, it is assumed that the coefficient of friction increases to 1.05, which is between 1.0 for concrete placed against intentionally

roughened concrete surfaces and 1.40 for concrete placed monolithically, as recommended by the American Concrete Institute's (ACI) Building Code Requirements ACI 318 (2008a).

From this assumed coefficient of friction, a simplified version of the model with elastic ITZ and matrix constitutive relations is utilized to estimate the pullout response of fibers from the matrix. The other significant change is the change to the Young's modulus brought by changes in the measured compressive strength. Figure 17 shows the calculated pullout response from simulations as dashed lines and the measured experimental data of Sujivorakul (2002) as solid lines.
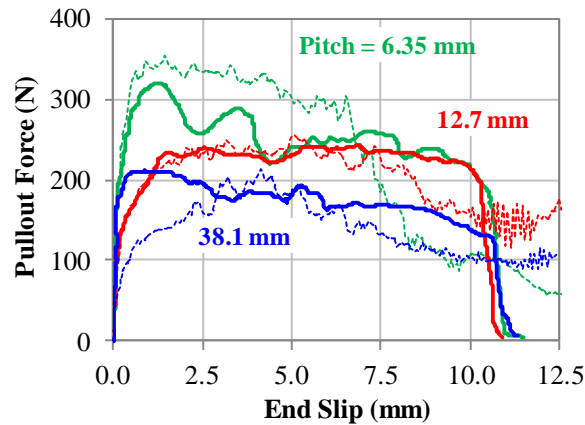
Figure 17. Pullout force as a function of end slip for $f_c = 84$ MPa. Experimental data shown as solid line and numerical data shown as dashed lines.

A comparison of the simulated and experimental data indicate that the simulation data are in the same rank order as the experimental data. To examine the differences quantitatively, Figures 18a and 18b compare the maximum pullout force and the total work during pullout for fibers with pitches of 6.35, 12.7, and 38.1 mm after being pulled from a $f_c = 84$ MPa matrix. For a given pitch, the maximum difference between the

maximum pullout force of the experiments and that of the numerical simulation is 11%;

the maximum difference between the total work of the experiments and that of the

numerical simulations is 7%.

(a) Maximum pullout force   (b) Total work
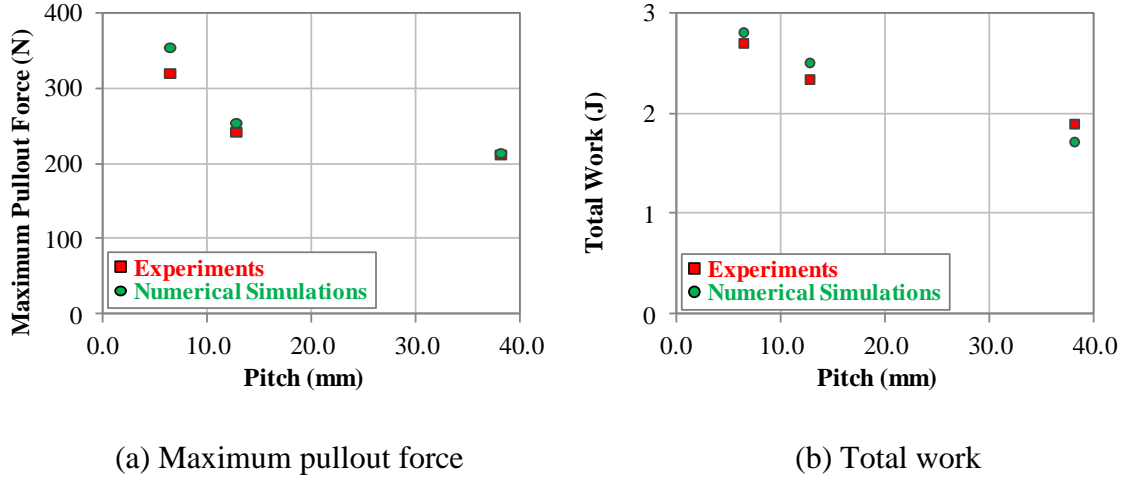
Figure 18. (a) Maximum pullout force and (b) total work during pullout for twisted
fibers with an embedded length of 12.5 mm after pullout from $f_c = 84$ MPa
matrix.

Experimental data are not available for the single fiber pullout of twisted fibers

from matrices with unconfined compressive strengths in excess of 84 MPa; however, an

estimate of the pullout response can be provided by altering material parameters of the

numerical model to understand the pullout response of higher strength matrices. Here it

is assumed that the mechanisms of pullout from higher strength matrices match those of

the $f_c = 84$ MPa, resulting in assumed elastic behavior of the matrix and ITZ with a

coefficient of friction value representative of concrete to concrete sliding. For a $f_c = 200$

MPa matrix, the material parameters are $E_m = 58.4$ GPa, $v_m = 0.2$, $E_{ITZ} = 35$ GPa,

$v_{ITZ} = 0.2$, and linear shrinkage of 0 μm/m. The elastic moduli are estimates utilizing

Eq. (5); the Poisson ratios are assumed values; and the coefficient of linear shrinkage is estimated from the CEB-FIB 1990 model code (1998). The assumed 1.05 coefficient of friction matches the coefficient of friction value assumed for the $f_c = 84$ MPa matrix materials.
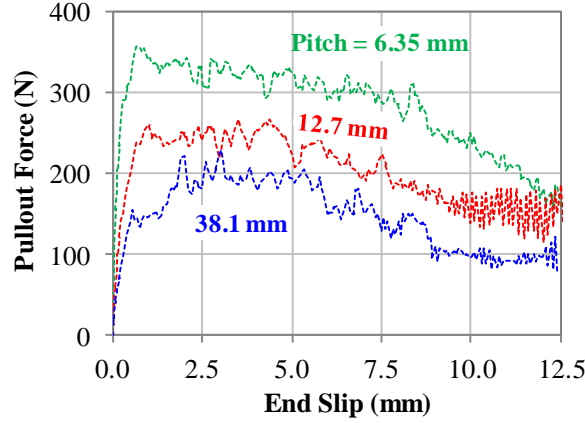
Figure 19. Pullout force as a function of end slip calculated in numerical simulations for $f_c = 200$ MPa.

3.2.4.4 *Effect of fiber pitch and matrix unconfined compressive strength*

The effects of fiber pitch and unconfined compressive strength of the matrix are explored for a fiber with a triangular cross section that has been twisted at a pitches between 6.35 and 38.1 mm. All the numerical simulations were run with 3.0-mm free lengths. Figures 20a and 20b summarize results of numerical simulations for the (a) maximum pullout force and (b) total work as a function of fiber pitch and f_c.

(a) Maximum pullout force   (b) Total work
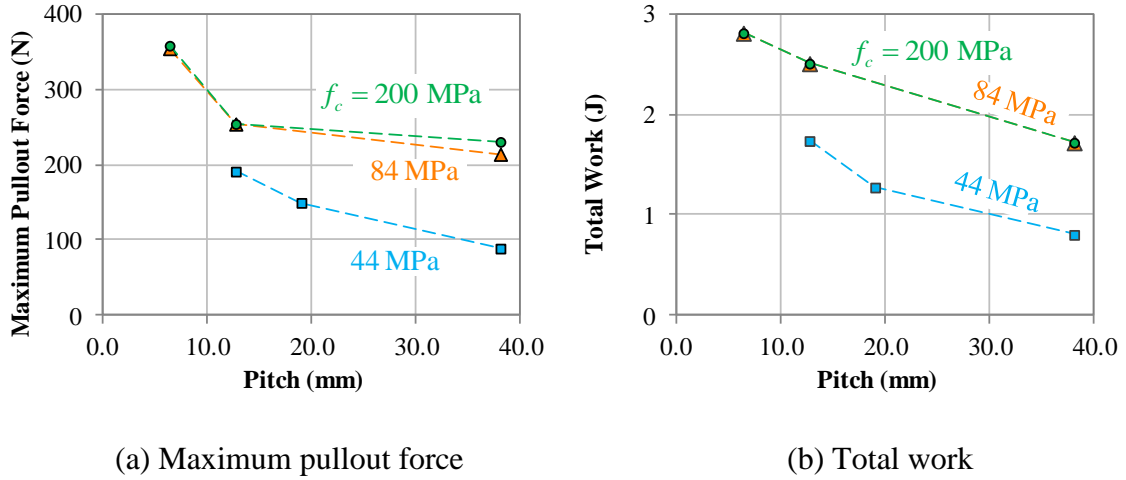
Figure 20. Effect of fiber pitch and f_c on the (a) maximum pullout force and (b) total work during pullout.

3.2.4.5 *Effect of Fiber Length*

The effect of fiber length is explored in this section for a fiber with a triangular cross section that has been twisted at a pitch of 12.7 mm with a free length of 3.0 mm. The embedded length ranges from 2.5 to 12.5 mm at increments of 2.5 mm. Results are shown in Figure 21. The results indicate that all fibers experience slip-hardening followed by slip-softening behavior in the last 2 mm of pullout. For this combination of cementitious and fiber materials and fiber geometry, only the fibers embedded 7.5 mm or greater have maximum pullout forces greater than or equal to 150 N.
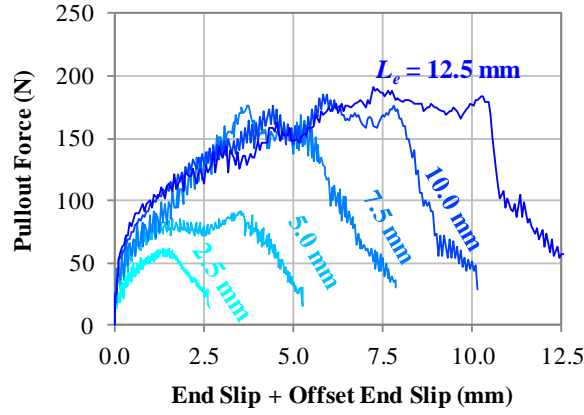
Figure 21. Numerically calculated pullout force as a function of end slip for triangular cross section fibers twisted at *pitch* = 12.7 mm and pulled from $f_c = 44$ MPa.

3.2.5 Treatment of fibers with arbitrary embedded lengths

Calculations at the single fiber length scale are resource intensive, requiring up to 400 hours to compute a single instantiation. This relatively long computation time combined with the infinite number of possible fiber embedded lengths at the multiple fiber length scale presents a problem: the extensive time required to compute all the pullout responses for the multiple fiber length scale is impracticable.

As a solution to this problem, the pullout force, P, as a function of end slip, Δ, is calculated for each combination of fiber and matrix parameters of interest using the maximum fiber embedded length, $L_{e,\max} = L_{fiber}/2$. Then an offset end slip, defined as $\Delta_{offset} = L_{e,\max} - L_e$, is added to the actual end slip Δ of fibers with $L_e < L_{e,\max}$. The pullout force as a function of an arbitrary embedded length L_e and end slip Δ is approximately equal to the pullout force at $L_{e,\max}$ and the combined end slip $\Delta_{comb} = \Delta + \Delta_{offset}$, i.e.,

$$P(L_e, \Delta) \approx P(L_{e,\max}, \Delta + \Delta_{offset}).$$

(14)

Figure 22 shows data from numerical simulations for the pullout force as a function of combined end slip for a 12.7-mm pitch fiber embedded 2.5-, 5.0-, 7.5-, 10.0-, and 12.5-mm deep into a matrix. The matrix strengths are 44-, 84-, and 200-MPa for Figures 22a, 22b, and 22c, respectively. In each plot, data for the 12.5-mm embedded fiber and 2.5-mm embedded fiber are shaded dark and light blue, respectively. Data at intermediate fiber embedded lengths are shaded in colors graded between dark and light blue. By plotting the pullout forces as a function of the combined end slip, the validity of Eq. (14) can be assessed. Although the $f_c = 44$ MPa does not overlay well for $L_e = 2.5$ and 5.0 mm, the $f_c = 84$ and $f_c = 120$ MPa are of greatest interest.

(a) $f_c = 44$ MPa   (b) $f_c = 84$ MPa
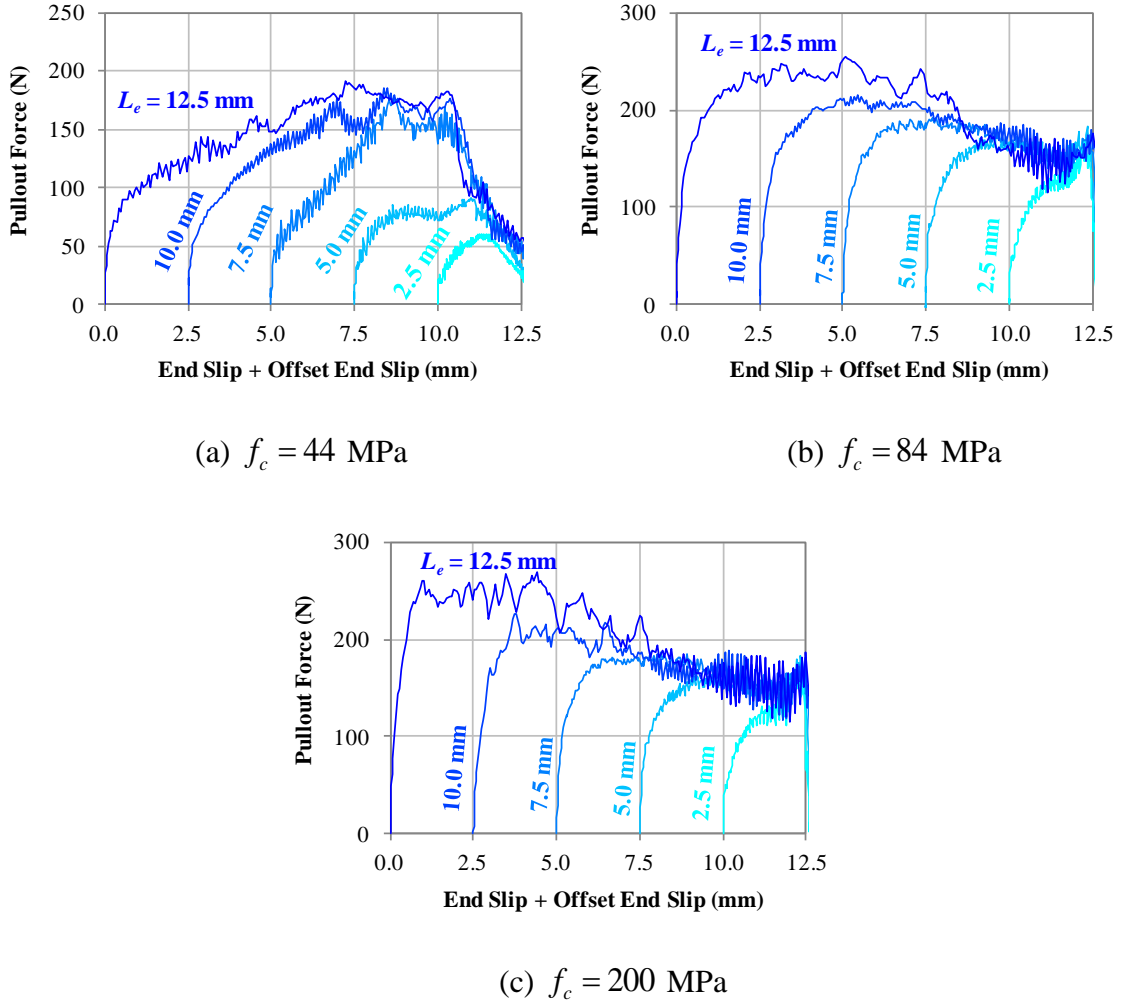
(c) $f_c = 200$ MPa

Figure 22. Pullout force as a function of the addition of end slip and offset end slip for fibers with uniform 12.7-mm pitch for $2.5 \leq L_e \leq 12.5$ mm embedded within (a) $f_c = 44$ MPa, (b) $f_c = 84$ MPa, and (c) $f_c = 200$ matrix.

3.3   Multiple fiber length scale

A two-element Rigid-Body-Spring-Model (RBSM) is adopted at the multiple fiber length scale to define the traction-separation response of an interface bridged by fibers. The RBSM assumes that after the matrix at a given interface cracks, the entire load is carried by the fibers (Bolander Jr. & Saito, 1997). Here, RBSM is introduced as

part of a multiscale model, instead of a standalone model at the structural length scale (e.g., Bolander, Choi, & Duddukuri, 2009).

As shown in Figure 23, the RBSM model consists of two rigid elements, labeled 1 and 2, and a large number of fibers shaded in red that cross the $x_1 = 0$ plane between the two rigid elements. Fibers are independently placed at pseudo-random positions and orientations within the model's three-dimensional domain until the desired volume fraction is reached. Note that the fibers that do not cross the rigid element interface are hidden in Figure 23. During deformation, rigid element 1 is restrained in all directions while rigid element 2 is displaced by δ in the x_1 direction; all other translations and rotations of either rigid element are prohibited. By summing the force of each fiber, a homogenized traction-separation response can be calculated that accounts for fiber orientation, length, volume fraction, and force-end slip relations.
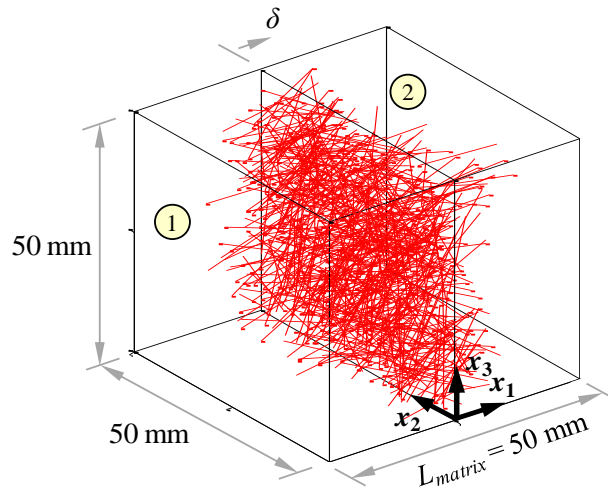
Figure 23. Sample instantiation of the Rigid-Body-Spring-Model (RBSM) at the multiple fiber length scale with $V_{fiber} = 2\%$, 14 mm fiber length, and 0.185 mm fiber diameter.

This model simplifies the multiple fiber length scale problem through several key assumptions. It is assumed that the matrix crack plane is predetermined, that the stress field around one fiber does not influence the stress field of other fibers (Bolander et al., 2009), that all fibers uniformly displace during the imposed displacement δ, the response of fibers are strain-rate insensitive, and that after any fiber is removed from the matrix, the forces are instantly and uniformly distributed to the other fibers that bridge the crack plane.

The model is decomposed into two parts: (1) pre-cracking tensile strength and (2) evolution of strength after matrix cracking. During the pre-cracking domain, the elastic stiffness of the composite is defined using a simple rule of mixtures approach, i.e.,

$$E_c = (1 - V_{fiber})E_m + \eta_l \eta_\theta V_{fiber} E_f, \tag{15}$$

where E_c is the elastic stiffness of the two-phase composite, E_m is the elastic stiffness of the matrix, η_l is a parameter accounting for fiber embedded length defined as

$\eta_l = 1 - \frac{\tanh(\beta L_{fiber}/2)}{\beta L_{fiber}/2}$, β is a parameter defined as $\beta = \sqrt{\frac{2G_m}{E_f r^2 \ln(R/r)}}$, G_m is the shear

modulus of the matrix, E_f is the elastic stiffness of the fiber, r is the radius of the fiber, R is the mean radius of the matrix around one fiber, L_{fiber} is the total length of the fiber, η_θ is a parameter associated with orientation of fiber defined as $\eta_\theta = \frac{1}{N_f} \sum_{i=1}^{N_f} \cos^4 \theta_i$,

N_f is the total number of fibers that cross the crack plane, and θ_i is the inclination able of the ith fiber between the fiber's direction and that of the direction of displacement (i.e., x_1). At a displacement of $L_{matrix}\varepsilon_{mu}/2$, the pre-cracking strength is $f_{t,pre} = E_c \varepsilon_{mu}$, where ε_{mu} is the fracture strain of the matrix without fibers.

After cracking of the matrix, the evolution of tensile strength, $f_t(\delta)$, is calculated

by summing the pullout resistance of each fiber that crosses the predefined crack plane,

i.e., $f_t(\delta) = \sum_{i=1}^{N_f} f_{i\theta}(L_e, \delta)$, where $f_{i\theta}$ is the pullout resistance of the ith fiber accounting

for the inclination angle, and L_e is the minimum embedded length in a Euclidian sense.

The relation between $f_{i\theta}$ and the pullout resistance of the ith fiber oriented parallel to the

pullout direction, f_i, is assumed as

$$f_{i\theta}(L_e, \delta) = \begin{cases} f_i(L_e, \delta)/\cos(\theta_i) & \text{for } -45° \leq \theta_i \leq 45° \\ f_i(L_e, \delta)/\cos(45°) & \text{for } |\theta_i| \geq 45° \end{cases}. \tag{16}$$

The form of Eq. (16) is based on experimental work of Li et al. (1990), who

measured the pullout force of straight, smooth fibers at inclination angles between $0°$

and $60°$.

The pullout force f_i can be determined by experiments, analytical models, or

numerical techniques. For straight, smooth fibers, an analytical fiber debonding model is

utilized that assumes the fiber slips out of the matrix and does not rupture. Resistance to

slipping is characterized by the interfacial shear strength, τ_s, which represents the

chemical bonding between the fiber and the matrix, and the frictional shear strength, τ_i,

which represents the mechanical resistance to the fiber slipping. By assuming that τ_s

and τ_i are equal, Gopalratnam and Shuh (1987) showed that f_i increases linearly to the

maximum pullout force, i.e.,

$$f_{\max} = \max\left(\frac{\frac{2\pi r \tau_s}{\beta} \sinh(\beta m L_e / 2) + \pi r L_e \tau_i (1-m) \cosh(\beta m L_e / 2)}{(1-\alpha)\cosh(\beta m L_e / 2) + \alpha} \right), \tag{17}$$

and then decreases linearly to zero at $\delta = L_e$. In Eq. (17), r and β were previously

defined, m is a monotonically increasing parameter that ranges from zero for an

undamaged fiber-matrix interface to one for a completely damaged fiber-matrix interface,

and $\alpha = A_f E_f / (A_m E_m)$ is a non-dimensional parameter relating the area of the fiber, A_f,

and the elastic modulus of the fiber to the area of the matrix, A_m, and the elastic modulus

of the matrix. An approximate solution to Eq. (17) can be found by assuming that

$(1-\alpha)\cosh(\beta m L_e / 2) \gg \alpha$, which results in f_{max} to be found at $m_{cr} \simeq \frac{2}{\beta L_e} a \cosh \sqrt{\tau_s / \tau_i}$.

Material parameters for the matrix are assigned as $E_m = 58.4 \text{ GPa}$, $v_m = 0.2$, and

$\varepsilon_{mu} = 0.20 \times 10^{-3}$, representative of a matrix with 200 MPa unconfined compressive

strength. Values of the interfacial shear strength, τ_i, for uncoated straight, smooth fibers

have been experimentally measured to be 5 (Shannag, Brincker, & Hansen, 1997), 4.8 –

5.5 (Chan & Chu, 2004a), 6 – 8 (Park et al., 2012), and 10 MPa (Orange, Acker, &

Vernet, 1999). Here, it is assumed that $\tau_i = \tau_s = 6 \text{ MPa}$.

3.4   Structural length scale

As shown in Figure 24, the model at the structural length scale is implemented in

three dimensions and consists of a UHPC panel shaded in red constrained by steel

restraints shaded in gray. The face of the panel shown in Figure 24 is denoted the

proximal face; the face not shown is denoted the distal face. The panel consists of bulk

elements and zero-thickness cohesive elements, which connect the two adjacent bulk

elements together. Bulk elements dictate the compressive response of the panel, and the

cohesive elements dictate the tensile response of the panel. In addition to modeling the

mean values of cohesive properties, the model accounts for a Gaussian distribution of

cohesive element properties, as indicated in Figure 24.

The panel is located between the front and back restraints such that there are

neither gaps nor compressive tractions between the panel and the restraints. The front

restraints, top and bottom, represent $76.2 \times 76.2 \times 7.94$ mm square structural steel tubing.

The back restraints, top and bottom, represent $203.2 \times 152.4 \times 12.7$ mm square structural

steel tubing. All four restraints are modeled without internal or external radii.
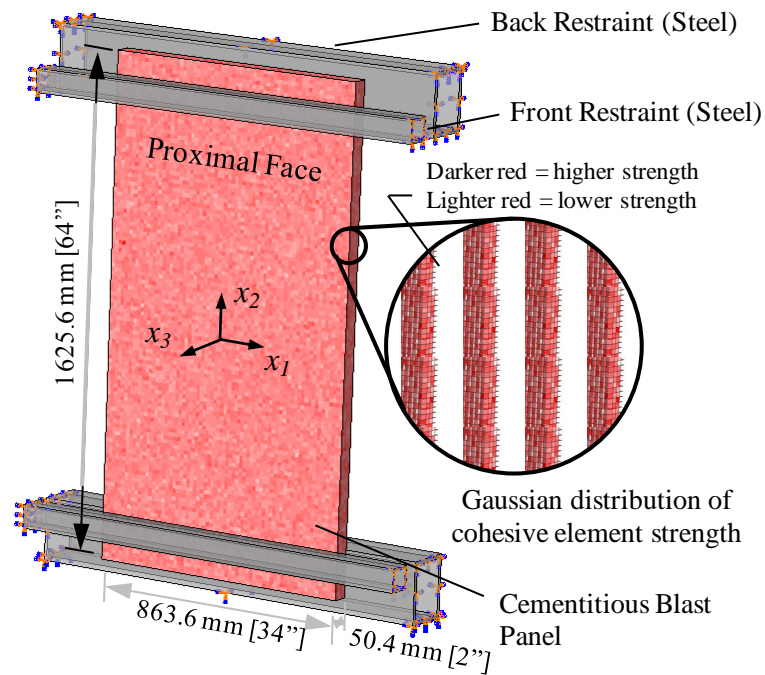
Figure 24. Model at the structural length scale showing the proximal face and restraints.

The constitutive model of the bulk elements in the panel is the extended Drucker-

Prager constitutive model described in Section 0, with $f_c^{'} = 200$ MPa and $E_m = 58.4$ GPa.

The interfacial debonding between two adjacent bulk elements is modeled via zero-thickness cohesive elements. A custom VUMAT (Dessault Systemes, 2010) defines a strain-rate sensitive traction-separation constitutive law used by the cohesive elements. Responses in the normal and tangent directions are uncoupled until the stress exceeds the strain-rate sensitive strength, at which point damage initiates. The isotropic damage internal state variable increases monotonically from zero (i.e., undamaged) to one (i.e., completely damaged) at the maximum rate of damage in the normal or tangent directions. Note that dissipated energy density is rate-insensitive as implied by Kim et al. (2009) for straight, smooth fibers. The structural and multiple fiber length scales through two cohesive element material parameters, namely the maximum quasi-static tensile strength and the dissipated energy density during pullout. The cohesive stiffness is assumed to be 200 GPa. The friction model is the rate- and pressure-independent, isotropic Coulomb friction law described in Section 3.1.4 and uses a 0.45 coefficient of friction. Interpenetration of elements is severely penalized. The restraints are assumed to be linear elastic with a 200-GPa Young's modulus, 0.3 Poisson ratio, and 7.85-g/cm^3 mass density.

Prior to loading, boundary conditions are applied to all four restraints. All four restraints have boundary conditions defined at the positive and negative x_1 faces, which prevent the translation or rotation of all nodes on those faces. Two additional boundaries are defined for the back restraints. First, the nodes on the positive x_2 face on the top back restraint are prevented from translating and rotating, Second, the nodes on the negative x_2 face on the bottom back restraint are prevented from translating and rotating. After applying boundary conditions to the four restraints, the proximal face of the panel is loaded by a time-dependent pressure in the negative x_3 direction. A pressure of p_{max} is

applied at 0 ms and linearly decreases to 0 Pa at 15 ms. From this pressure profile, the

applied specific impulse I is $I = \dfrac{15ms}{2} p_{max}$.

3.4.1 Strain-rate sensitive traction-separation

Interfacial debonding between bulk elements is modeled using zero-thickness cohesive elements and a strain-rate sensitive traction-separation constitutive model implemented via a custom VUMAT subroutine called by ABAQUS/Explicit. If the strain rate, $\dot{\varepsilon}$, is equal to a quasi-static strain rate, the model assumes the bilinear response shown in Figure 25, where T is the traction, δ is the separation, K is the stiffness of the cohesive elements, and G^c is the work of separation defined as the integral of traction from zero separation to the separation at complete failure, δ^f. Subscripts n, s, and t indicate the normal and two tangential directions, respectively. Note that the traction-separation constitutive relation at quasi-static strain rates is the same as the prebuilt traction-separation constitutive relation in ABAQUS (Dessault Systemes, 2010).
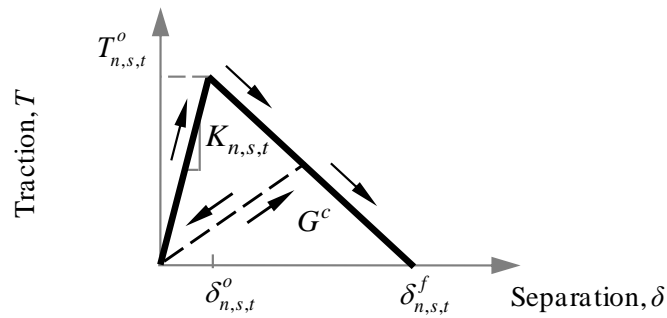
Figure 25. Traction-separation constitutive relation for a quasi-static strain rate.

The strain rate of each element at each time interval is calculated by

$\dot{\varepsilon} = \max\left(\dfrac{d\delta_{n,s,t}}{dt\, L_{elem}}\right)$, where $d\delta_{n,s,t}$ is the incremental separation in the $n, s,$ and t directions,

dt is the time step, and L_{elem} is the characteristic element size. The dynamic tensile

strength, $T_{n,s,t}^{\dot{\varepsilon}}$, is defined as $T_{n,s,t}^{\dot{\varepsilon}} = TDIF \times T_{n,s,t}^{o}$, where the tensile dynamic inflation

factor (from Zhou et al. (2008)) is expressed as

$$TDIF = \begin{cases} 1 & \text{for } \dot{\varepsilon} \le 10^{-4} \\ 2.06 + 0.26\log_{10}\dot{\varepsilon} & \text{for } 10^{-4} < \dot{\varepsilon} \le 1 \\ 2.06 + 2.0\log_{10}\dot{\varepsilon} & \text{for } 1 < \dot{\varepsilon} \le 10^{3} \end{cases} \qquad (18)$$

For $\dot{\varepsilon} > 10^{3}$ a conservative estimate of $\dot{\varepsilon} = 10^{3}$ is assumed. As suggested by Kim

et al. (2009), the work of extracting straight, smooth fibers from a cementitious matrix is

relatively rate insensitive; hence, it is assumed that the work or separation is invariant

with respect to strain-rate.

The initial linear-elastic portion in Figure 25 is decoupled in the normal and tangential

directions (i.e., $T_i = K_i \delta_i$ where $i = n, s, t$ without summation implied, and K_i is the

stiffness in the ith direction). Damage initiation (peak traction in Figure 25) leads to

coupling between the normal and tangential directions and is governed by the quadratic

initiation criterion $\left(\dfrac{\langle T_n \rangle}{T_n^{\dot{\varepsilon}}}\right)^2 + \left(\dfrac{T_s}{T_s^{\dot{\varepsilon}}}\right)^2 + \left(\dfrac{T_t}{T_t^{\dot{\varepsilon}}}\right)^2 = 1$, where the Macaulay brackets are defined by

$\langle x \rangle = 1/2\left(|x| + x\right)$. Damage evolution is calculated by $d = \max\left(\dfrac{\delta_i^f(\delta_i^{max} - \delta_i^o)}{\delta_i^{max}(\delta_i^f - \delta_i^o)}\right)$, where

$i = n, s, t$ without summation implied and δ^{max} is the maximum separation during the

loading history (Dessault Systemes, 2010).

3.4.1.1   Mesh sensitivity

The strain-rate sensitive traction-separation constitutive model introduces a characteristic length scale, i.e., L_{elem}, to reduce the mesh sensitivity of the model. This section examines the mesh sensitivity of the model, as determined by the deflection at the center of the UHPC panel (cf. Figure 24) for a predefined loading condition and fixed material parameters. In this section, a fixed panel thickness of t_{panel} = 50.8 mm was used for all instantiations.

The material parameters used to study mesh sensitivity are as follows. Bulk elements utilized a 2.57-g/cm^3 mass density, 58.4-GPa elastic modulus, 200-MPa unconfined compressive strength, 28º internal friction angle, 22º dilation angle, and 0.8 ratio of triaxial tension yield strength to triaxial compression yield strength. Cohesive elements utilized a 200-GPa stiffness, 11.7-MPa quasi-static tensile strength, and 13.5-kJ/m^2 energy dissipation density. The UHPC panel was meshed with 1, 2, 4, and 6 elements through the thickness of the panel, resulting in L_{char} = 50.8, 25.4, 12.7, and 8.467 mm, respectively. A maximum applied pressure of 273 kPa was applied to the proximal face of the panel, resulting in an applied impulse of 2.05 MPa-ms.

Results of the mesh sensitivity study are shown in Figure 26, which shows the displacement at the center of the panel as a function of time. The calculated displacements as functions of time for L_{char} = 12.7 and 8.47 mm are similar, indicating that the L_{char} = 12.7 mm results in a converged mesh.
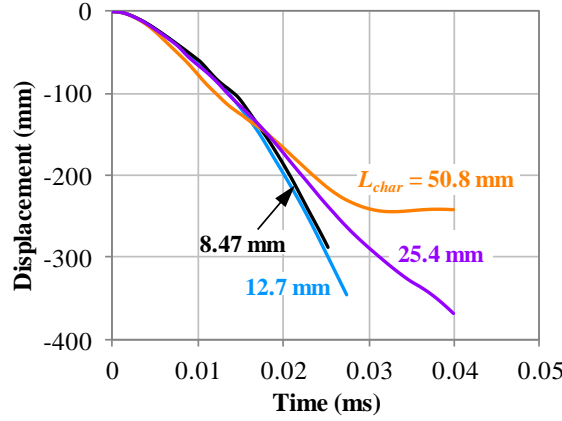
Figure 26.   Deflection at the center of panel as a function of mesh density.

3.4.2   *Validation of the multiscale model at the structural length scale*

The model was validated by comparing simulated results to experimental results

of Ellis, DiPaolo, McDowell, and Zhou (2013), which provide a 0.97 MPa-ms lower

bound and a 1.46 MPa-ms for the critical specific impulse of the panel. Here, critical

specific impulse is defined as the lowest value of specific impulse that fractures the

panel.

3.4.2.1   *Physical experiment setup*

A UHPC slurry was prepared at the United States Army Corps of Engineers

(USACE) Engineering Research and Development Center (ERDC) using Ductal[®]

BS1000 Grey premix, Chryso[®] Fluid Primea 150 high-range water reducing agent, 2%

volume fraction, V_{fiber} , of steel fibers, and water at a 0.19 nominal water to cementitious

material ratio. The fibers were 14 mm-long with 0.185 mm-diameter circular cross-

section and were measured to have a 2.16-GPa tensile strength, 210 GPa elastic stiffness,

81

and 7.85 g/cm^3 mass density. The four constituents were mixed in a Nikko high shear

mixer according to recommendations provided by Lafarge, the manufacturer of Ductal.

The mixed UHPC slurry was poured into four different rectangular cavities each

having dimensions of 1,626 mm (long) × 864 mm (wide) × 50.4 mm (deep). At the

bottom of each cavity, two layers of Hardwire® 3×2-4-12-500 brass reinforcement

(HardwireLLC, n.d.) were placed at +45º and -45º from the direction of the 1,626 mm

length of the cavity. Panels were then cured at 22ºC under wet burlap for 24 hours,

followed by 2 days in a steam cabinet at 91ºC.

The mechanical properties of UHPC were measured fourteen days after pouring

using three 101.6 mm-diameter by 203.2 mm-tall cylinders. The cylinders were poured

from the same UHPC slurry and cured using the same protocol as the panels. Test results

for the density, ρ_{UHPC}, and quasi-static unconfined compressive strength, f_c, are given in

Table 4.

Table 4. Density and unconfined compressive strength for cylindrical specimens.

Sample ID	ρ_{UHPC} (kg/m^3)	f_c (MPa)
125-11DIP #1	2,567	200
125-11DIP #2	2,566	206
125-11DIP #3	2,565	196
Mean	2,566	201
Standard Deviation	1.0	5.0

Figure 27 shows a backscatter scanning electron microscope (SEM) image of the

as-cured UHPC microstructure (Wang, Mattus, & Ren, 2009). In Figure 27, the black

circle represents porosity, the white ellipses represent fibers, the dark grey represents

quartz aggregate, and the regions between the previously listed components represent the

paste. The magnified view at the right of Figure 27 shows that the paste is composed of

unhydrated clinker (white), quartz powder (dark grey), cracks (black) and hydrated Calcium-Silicate-Hydrate (medium grey). Note that SEM images were recorded in a vacuum, which implies that the visible cracks in the magnified view may be due to drying during the preparation of the specimen for SEM studies.
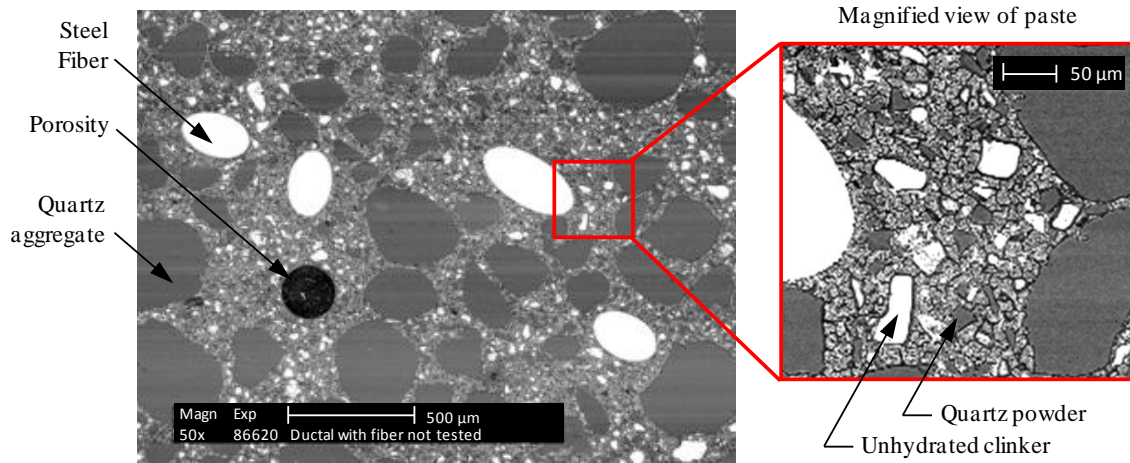
Figure 27. Backscatter scanning electron microscope image of UHPC microstructure (Wang et al., 2009).

Panels were tested at the United States Army Corps of Engineers (USACE) Engineering Research and Development Center (ERDC) Blast Loading Simulator (BLS) located in Vicksburg, MS (DiPaolo et al., 2012). As shown in Figure 28, the BLS is composed of a driver, expansion rings, straight rings, and the target vessel. After the UHPC panel is placed in the target fixture, the target vessel is connected to the straight rings. To initiate the test, a disk between the driver and expansion rings is ruptured, thus releasing the compressed air contained within the driver. The pressure wave travels through the expansion and straight rings before encountering the target located in the target vessel. The BLS produces planar waveforms with peak reflected pressures and impulses of 552 kPa and 11.0 MPa-ms, respectively.
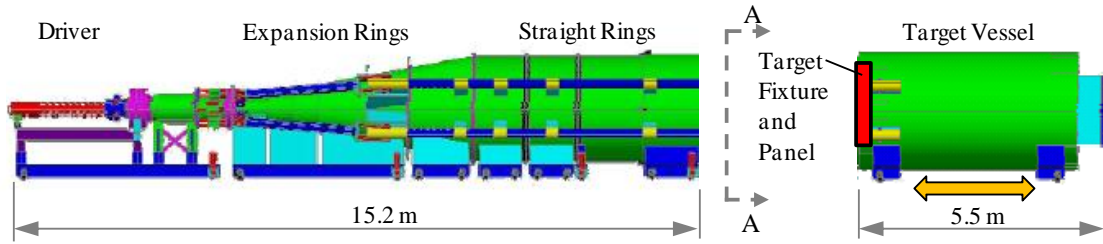
Figure 28. Schematic of Blast Load Simulator (BLS).

The UHPC panel is placed in the target fixture at the location indicated in Figure 28. The target fixture consists of an insert and a cover as shown in Figures 3a and 3b, respectively. The insert consists of two $203.2 \times 152.4 \times 12.7$ mm structural steel tubes and two $50.8 \times 50.8 \times 6.35$ mm structural tubes. The panel is placed in the insert with the Hardwire reinforced surface adjacent to the $50.8 \times 50.8 \times 6.35$ mm steel tubing. The cover keeps the panel in position before and during testing. The target fixture imposes conditions similar to, but not exactly the same as, "simply supported" boundary conditions.

Reflected pressure was recorded by six pressure transducers located at the positions shown as small yellow circles on the target fixture cover in Figure 29b. Displacement of the distal face of the panel was recorded by an accelerometer and laser measurement system at the positions indicated in Figure 29b. Video images of the distal face were recorded at a 1,000 frames per second.

(a) Insert (b) Cover, UHPC panel, and sensor locations
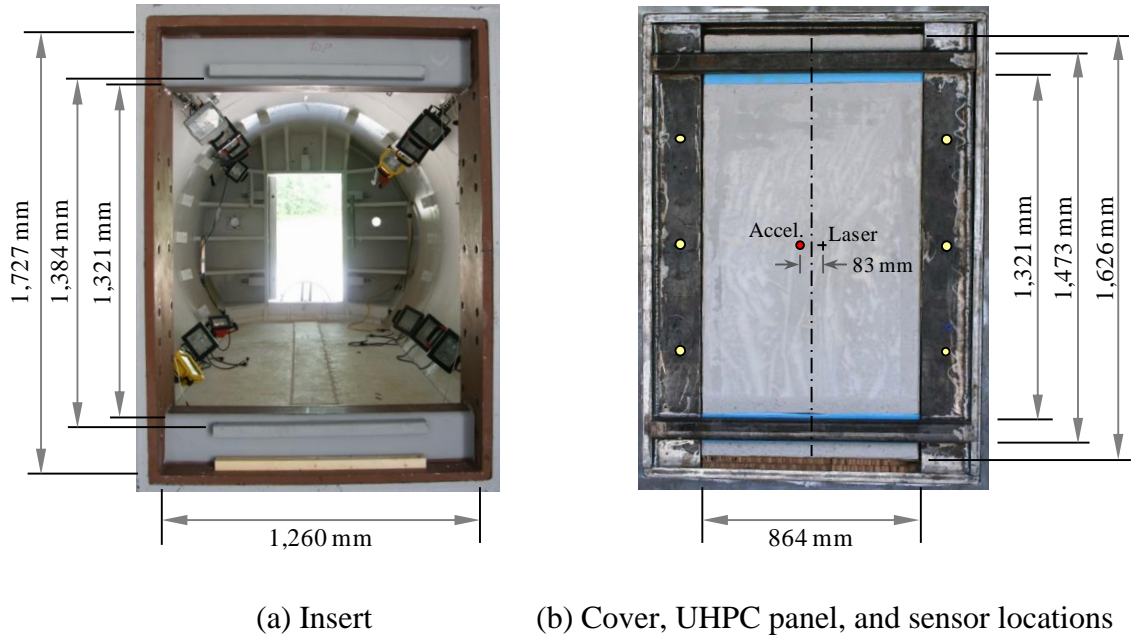
Figure 29. Target fixture as viewed from section A-A (cf. Figure 28) showing the (a) target fixture insert and (b) target fixture cover, proximal face of UHPC panel, and sensor locations.

3.4.2.2   *Parameters estimated by model at the single fiber and multiple fiber length scales*

Validation of the multiscale model starts with the choice of a straight, smooth fiber morphology, with the maximum pullout force given by Eq. (17). Then using 2% fiber volume fraction of 14-mm long by 0.185-mm diameter simulated fibers, 100 realizations of the model at the multiple fiber length was the model at the multiple fiber length scale were used to determine the values of four variables – mean tensile strength, standard deviation of the tensile strength, mean dissipated energy density, and standard deviation of the dissipated energy density – to inform the model at the structural length scale via a hand-shaking scheme. In this manner, the homogenization scheme ensures

that the energy barrier to fracture, i.e., the maximum tensile stress, and the dissipated

energy are consistent between length scales.

Results of the 100 realizations at the multiple fiber length scale are shown in

Figure 30. Figure 30a shows the tensile stress versus displacement, where the dissipated

energy density is the integral of tensile stress over the displacement δ; Figures 30b and

30c show histograms of the maximum tensile strength and the dissipated energy density,

respectively, with Gaussian distribution function overlaid on each histogram.

(a) Tensile stress versus displacement

(b) Histogram of maximum tensile strength

(c) Histogram of dissipated energy density
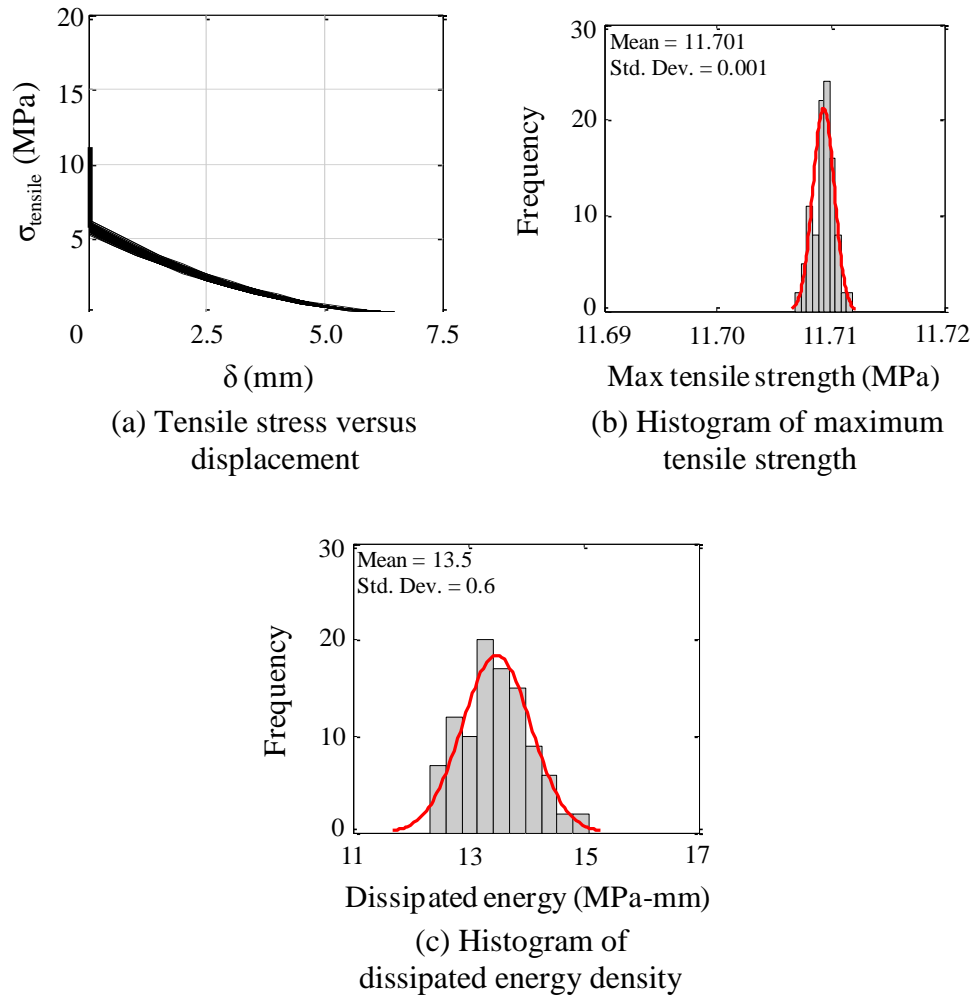
Figure 30. Stochastic variation of (a) tensile stress versus displacement, which leads to mean and standard deviation values of (b) maximum tensile strength and (c) dissipated energy density.

The results shown in Figure 30 from the multiple fiber length scale are used for the cohesive material structural length parameters at the structural length scale, as listed in Table 5.

Table 5. Cohesive element material properties.

$K_{n,s,t}$ (GPa)	$T^o_{n,s,t}$ (MPa)		$G^c_{n,s,t}$ (kJ/m^2)	
	Mean	Std. Dev.	Mean	Std. Dev.
200	11.7	0.0	13.5	0.6

3.4.2.3   Comparison of numerical simulations and physical experiments

The four physical panels were subjected to reflected impulses from 0.77 to 2.05 MPa-ms. Panels 1 and 2 fractured when exposed to reflected impulses of 2.05 and 1.46 MPa-ms, respectively. Panel 3 survived two tests at impulses of 0.77 and 0.97 MPa-ms before fracturing during a third test at an impulse of 1.46 MPa-ms. Panel 4 was intentionally perforated prior to testing, at which the panel fractured when loaded with a 0.97 MPa-ms impulse. From the experiments, the critical impulse that caused an initially intact panel to fracture was between 0.97 and 1.46 MPa-ms. For the four panels tested, fracture created negligible particle debris and led to fracture surfaces containing protruding fibers.

Validation of the multiscale model was based on three criteria: critical impulse to fracture the panel, which created two or more separate sections of the panel; deformation and fracture patterns; and displacement at the mid-height of the panel. Specifically, the multiscale model determined the critical specific impulse to be between a 0.97-MPa-ms lower bound and a 1.21-MPa-ms upper bound, which is within the experimentally determined 0.97-MPa-ms lower bound and 1.46-MPa-ms upper bound.

The remaining two validation criteria were based on experimental results with an experimentally observed impulse of 2.05 MPa-ms after 15 ms, the time at which a through-crack was evident. Figure 31 shows the comparison between the numerically applied pressure shown as a black dashed line and the experimentally observed pressure shown as a solid purple line. The resulting experimental observed and numerically applied impulses are shown as solid blue and dashed orange lines, respectively.
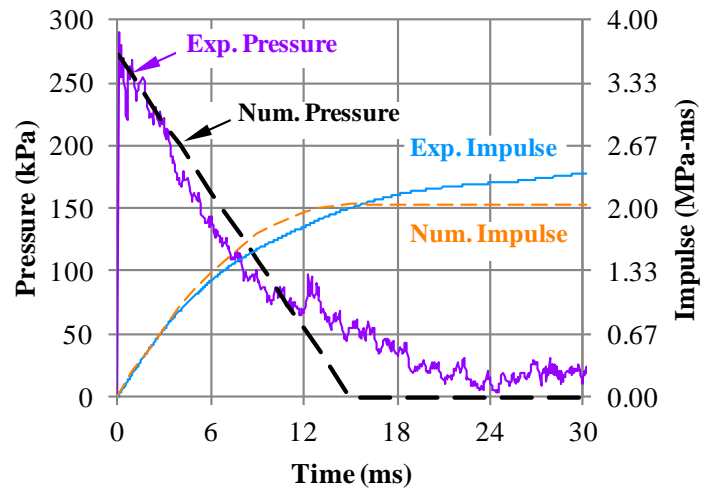
Figure 31. Idealized pressure and impulse compared to the experimentally observed pressure and impulse for validating multiscale model.

Figure 32 shows the deformation and fracture patterns of Panel 1, which was subjected to a 2.05-MPa-ms impulse, and one instantiation of the multiscale model subjected to the same impulse. At 6 ms, the physical experiment and the simulation indicate parabolic deformation; moreover, the simulation exhibits distributed cracking. At 12 ms, the distributed cracking in the simulation has coalesced into two prevailing cracks near the panel's mid-height. Images of the experimental panel indicate similar

phenomenon with the distributed cracking coalescing into a characteristic mid-height fracture. Subsequently, the simulated panel fractured at two additional locations near the top and bottom restraints. Because the video of the physical experiment taken of the distal face, it can only be assumed that the fractures near the top and bottom restraints occurred after the mid-height fracture.
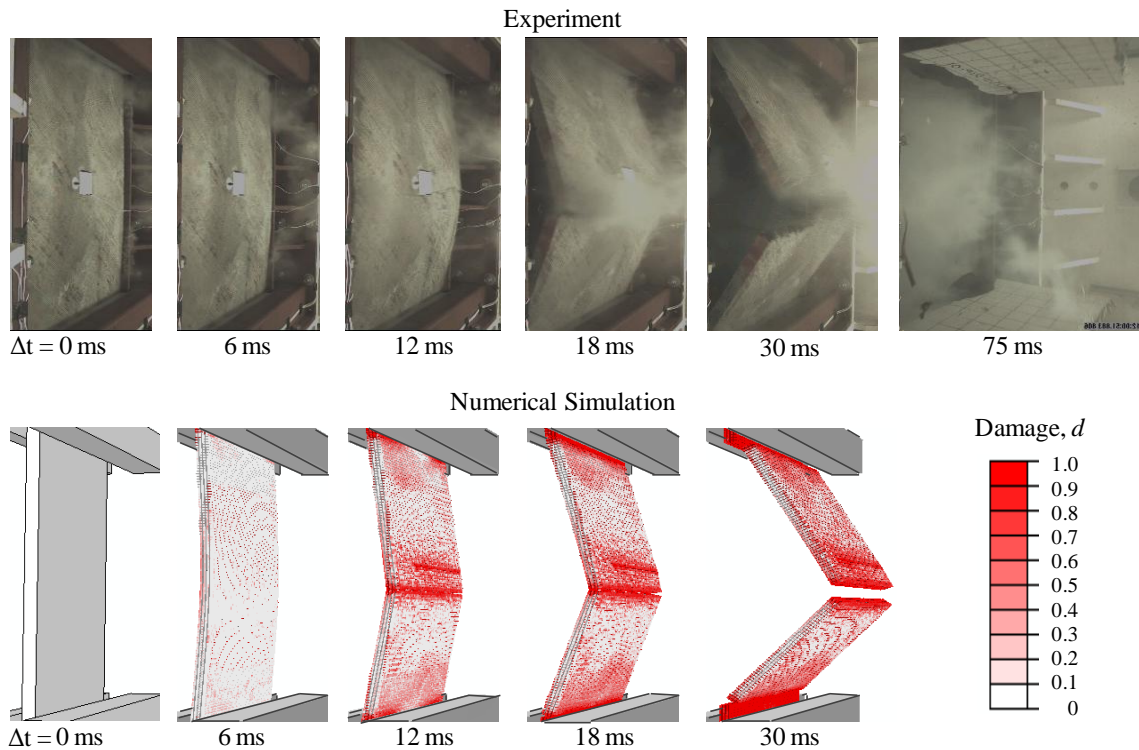
Figure 32. Physical experiment and one instantiation of the multiscale model of a UHPC panel subjected to a 2.05 MPa-ms reflected impulse. The instantiation exhibits distributed cracking at 6 ms before crack coalescence and growth at 12 ms. Both the physical experiments and numerical simulations possess three areas of characteristic fracture – one at the lower restraint, one at the mid-height, and one at the top restraint.

The last criteria for model validation is the displacement of the center of the panel as a function of time, as shown in Figure 33. For times less than 18 ms, the simulation under predicts the displacement measured by the accelerometer by a maximum of 23%.

Several possible reasons for the error include the assumed 0.2×10^{-3} strain of the matrix at failure, ε_{mu}, the assumed strain-rate tensile dynamic inflation factor, and the exclusion of fluid-structure interactions. For times greater than 18 ms, accelerometer data and video images indicate that the numerical simulation over-predicts displacements. This over-prediction is attributed to the exclusion of the distal face mesh from the model. Noting that crack coalescence occurs at 12 ms, it is assumed that the calculated critical specific impulse is relatively unaffected by the lack of the distal face mesh in the model.
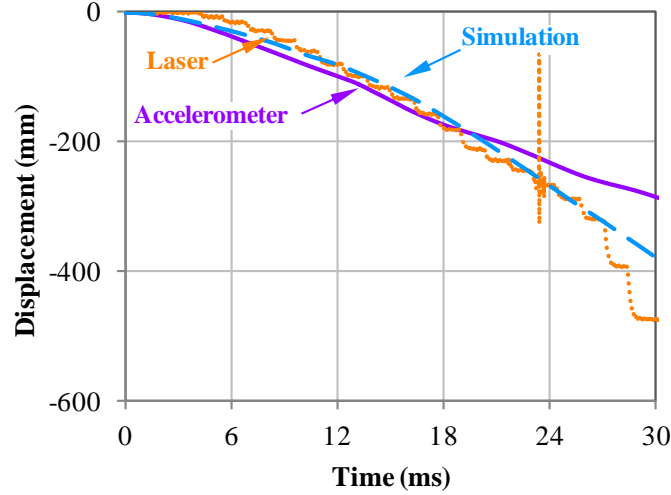
Figure 33. Comparison of displacement of the center of the panel in the x_3 direction (cf. Figure 24) measured by accelerometer and laser interferometer measurement systems and the displacement predicted by the multiscale model ($I = 2.05$ MPa-ms).

3.4.3   Accumulation of damage

After validation, the multiscale model was utilized to predict the damage initiation impulse at which the panel accumulated less than 1% total damage. Here, total damage is defined as the sum of damage of all cohesive elements divided by total number of

elements. As shown by the evolution of total damage for impulses between 0.24- and

2.05-MPa-ms in Figure 34, an impulse of 0.24-MPa-ms produced less than 1% total

damage for the material parameters considered. By determining the damage initiation

impulse, panels may be quickly assessed for damage after subjected to a given impulse

load.
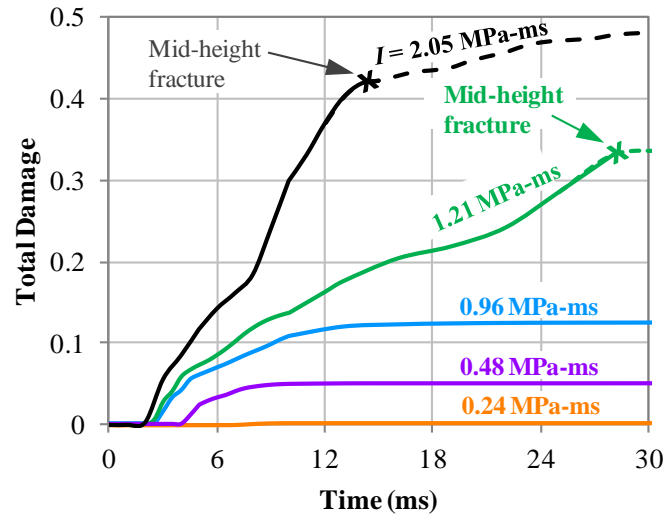
Figure 34.   Total damage for simulated UHPC panel with a mean 11.7-MPa mean $T_{n,s,t}^{o}$
and 13.5-kJ/m2 mean $G_{n,s,t}^{o}$ for impulses between 0.24- and 2.05-MPa-ms.

3.4.4   *Effect of quasi-static tensile strength and dissipated energy density*

The validated multiscale model was used within a parametric study to determine

the influence of mean $T_{n,s,t}^{o}$ and $G_{n,s,t}^{c}$ material properties on the critical specific impulse

required to completely fracture the simulated panel. Results of the parametric study are

shown in Figure 35 with tensile strengths of 14.7, 20, and 40 MPa shown as blue circles,

purple triangles, and orange squares, respectively. The validation point using the

91

material properties from Table 5 is shown as a gray diamond within the experimentally

determined range of 0.97- to 1.46-MPa-ms shown as a yellow rectangle. As expected,

the critical specific impulse increases with both increasing dissipated energy densities at

the interface and the maximum tensile strength. For a dissipated energy density of 20

kJ/m^2, doubling the tensile strength from 20 to 40 MPa increases the critical specific

impulse by only 16%. In comparison, doubling the dissipated energy density from 20 to

40 kJ/m^2 increases the critical specific impulse by 40% for a 14.7 MPa tensile strength.

These results indicate that increases to the dissipated energy density, e.g. changes to fiber

content or fiber geometries, offer the most efficient improvements to the critical specific
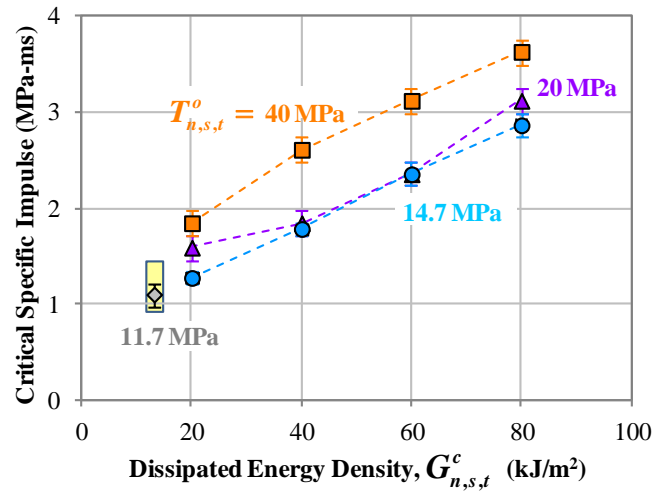
impulse.

Figure 35. Calculated critical specific impulses required to completely fracture the simulated UHPC panel with dissipated energy densities between 20 and 80 kJ/m^2 and tensile strengths of 14.7, 20, and 40 MPa.

3.4.5   *Effect of panel thickness*

The effect of panel thickness is examined in this section. Three panel thicknesses were examined between at thicknesses of 38.1, 50.8, and 63.5 mm. At each panel thickness, four dissipated energy densities – 20, 40, 60, and 80 kJ/m^2 – and three quasi-static tensile strengths – 14.7, 20, and 40 MPa – were examined to determine the critical specific impulse, at which the panel fractures. Critical specific impulses were found through a bisection method to determine the maximum reflected impulses that does not fracture the panel and the minimum reflected impulse that does fracture the panel. Results from the simulation are shown in Figure 36.
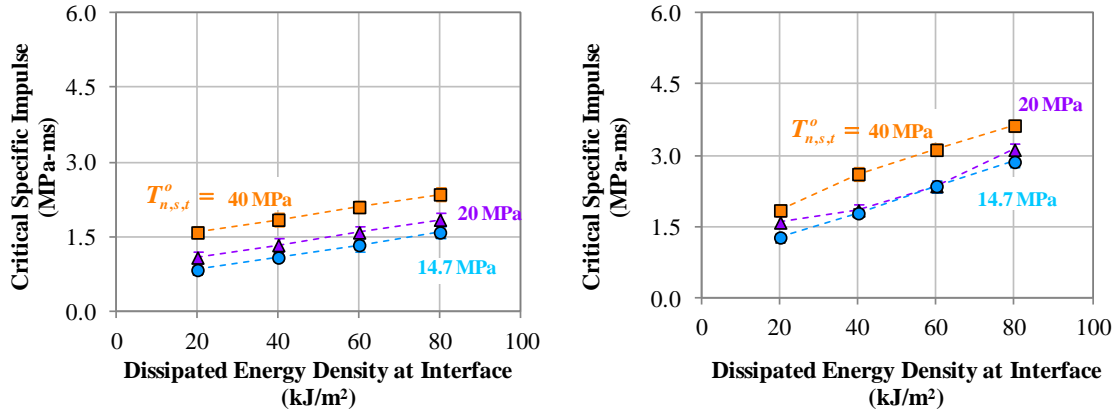
(a) $t_{panel} = 38.1$ mm

(b) $t_{panel} = 50.8$ mm
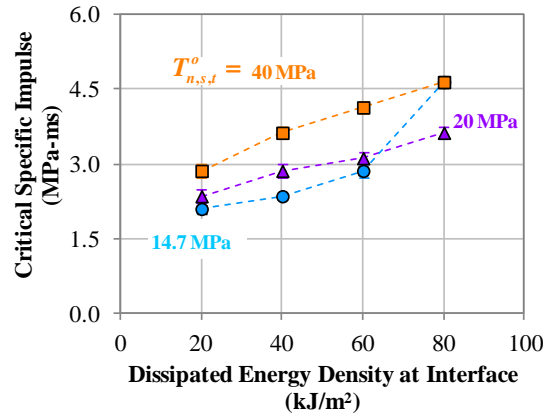
(c) $t_{panel} = 63.5$ mm

Figure 36. Simulated critical specific impulses for panel thicknesses of (a) 38.1 mm, (b) 50.8 mm, and (c) 63.5 mm.

Figure 36c indicates an unexpected increase in critical specific impulse between $G_{n,s,t} = 60$ and 80 kJ/m^2 for simulations with $T_{n,s,t}^0 = 14.7$ MPa. Moreover, the critical specific impulse of 4.65 MPa-ms surpasses the 3.63-MPa-ms critical specific impulse for the $T_{n,s,t}^0 = 20$ MPa panel with the same 63.5-mm thickness and 80-kJ/m^2 energy dissipation density. This change in behavior is a result of the $t_{panel} = 63.5$ mm,

$T_{n,s,t}^0 = 14.7$ MPa, and $G_{n,s,t} = 80$ kJ/m^2 panel instantiation behaving in a ductile manner,

as shown by the damage, deformation, and fracture patterns shown in Figure 37. In

Figure 37a, the $G_{n,s,t} = 60$ kJ/m^2 was loaded with a 3.0-MPa-ms specific impulse, leading

to the characteristic brittle fracture pattern observed in experiments (cf. Figure 32) and in

all the instantiations except the $G_{n,s,t} = 80$ kJ/m^2 shown in Figure 37b. The ductile

response shown in Figure 37b was marked by a pronounced parabolic shape, significant

distributed cracking on the distal face, and fracture initiation at the upper and lower

restraints instead of the mid-height of the panel.

Damage, d

(a) $G_{n,s,t} = 60$ MPa
$I = 3.0$ MPa - ms

(b) $G_{n,s,t} = 80$ MPa
$I = 4.78$ MPa - ms
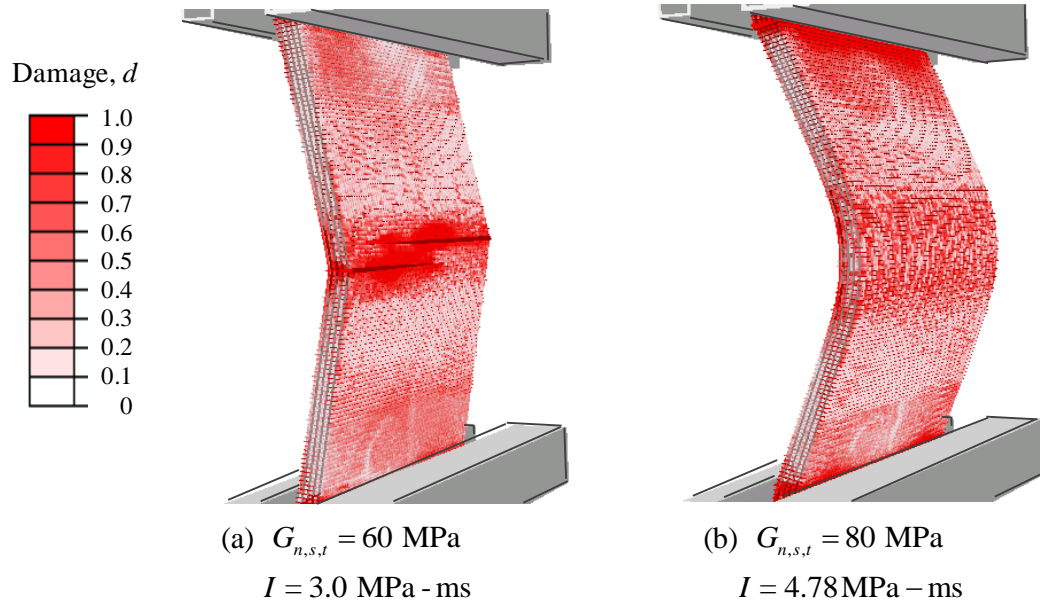
Figure 37. Comparison of damage, deformation, and fracture patterns for 63.5-mm thick simulated panels with $T_{n,s,t}^0 = 14.7$ MPa, and (a) $G_{n,s,t} = 60$ MPa and (b) $G_{n,s,t} = 80$ MPa. Images are shown 12 ms after the initiation of a (a) 3.0 MPa-ms and (b) 4.78 MPa-ms applied impulse.

The implications of these findings extend beyond finding a single instantiation exhibiting relatively higher critical specific impulses. Rather, the ductile response implies that a yet to be determined domain of quasi-static tensile strengths and dissipated energy densities may cause the simulated panel to exhibit a desired ductile response. The second implication is that increasing the dissipation at lower length scales, i.e., the multiple fiber length scale which was homogenized to the cohesive elements at the structural length scale, has a significant influence on the structural response.

3.5   Summary

This chapter presents a multiscale model consisting of three length scales – single fiber, multiple fiber, and structural panel – to simulate the response of UHPC blast panels to reflected impulses between 0.5 and 4.5 MPa-ms.

At the single fiber length scale, a model was developed to predict the pullout force as a function of material properties and fiber morphology, which is expressed via the fiber's cross section, equivalent diameter, and the pitch at which the fiber was twisted along its primary axis. The model accounts for three phases of material: fiber, an Interfacial Transition Zone (ITZ) between the fiber and the surrounding matrix, and the matrix. The dissipation mechanisms considered include plastic deformation of the fiber, friction at the fiber-ITZ interface, and plastic deformation due to granular flow of the ITZ and matrix. The model was calibrated to experimental data using a triangular cross-section fiber with a 0.5-mm equivalent diameter and a 12.7-mm pitch. The surrounding matrix had an unconfined compressive strength, f_c, of 44 MPa. Subsequently, the model

was validated to experimental data for 38.1-mm pitched fibers using the same material properties as the 12.7-mm pitch fiber.

For higher strength matrices containing silica fume, the coefficient of friction was increased from 0.45, representing steel on concrete sliding friction, to 1.05 which is between the range of 1.0 for a concrete surface intentionally roughened and 1.40 for two concrete surfaces formed after a monolithically poured concrete fractures. At the 1.05 coefficient of friction value, the matrix and ITZ are assumed to be elastic. Results of numerical simulation are shown to agree within 11% and 7% of the maximum pullout force and total work during pullout, respectively.

Results at the single fiber length scale indicate that fiber morphology significantly influences the resistance of fibers against pullout from the cementitious material. Specifically, the twisting of fibers around their own axes can increase the maximum pullout force by 5 times and the total work during pullout by over 10 times. The mechanisms responsible for this improvement are enhanced interactions between the fiber and the ITZ caused by granular flow and dilation of the ITZ and matrix. The interactions manifest as a domain identified as the stress transition zone (STZ).

The free length, defined as the portion of the fiber between the cementitious material and the position at which the fiber is pulled from, influences the pullout response of twisted fibers measured in physical experiments. Specifically, numerical simulations indicate that 0.0-mm free lengths, such as the free lengths found at crack surfaces in situ, cause twisted fibers to have higher pullout forces than similar fibers with 3.0-mm free lengths. The level of influence varied by the fiber pitch, decreasing with decreasing fiber

pitch. This finding is significant because it indicates that experimental pullout data may be viewed as conservative compared to in situ performance.

At the multiple fiber length scale, fibers are placed pseudo-randomly and independently within a three-dimensional domain consisting of two elastic elements separated by a predefined crack surface. Each fiber crossing the predefined crack face is assigned a pullout force versus end slip relation, which can be defined via experiments, analytical solutions, or computational solutions. For example, the pullout force versus end slip relation for straight smooth fibers with circular cross-sections is calculated via analytical equations with interfacial shear strengths taken from literature. The pullout force versus end slip relations for triangular cross-sectional fibers twisted along their axes were calculated using the single fiber length scale model. The pullout force of each fiber is adjusted to account for the inclination angle, defined as the angle between the fiber's major axis and the normal of the predefined crack plane. The model at the multiple fiber length scale adds information relating to the fiber volume fraction and fiber orientation relative to a predefined crack. The model homogenizes the response of fibers to calculate a quasi-static tensile strength and the dissipated energy density at each interface. By running 100 instantiations for each combination of fiber and matrix parameters, distribution functions are found for the quasi-static tensile strength and dissipated energy density, which are used for scale transition to the structural length scale.

At the structural length scale, a three-dimensional cohesive finite element model, utilizing a strain-rate sensitive cohesive traction-separation response, was used to simulate the blast response of a 1625.6-mm tall by 863.6-mm wide UHPC panel placed within top and bottom steel restraints. Blast loads are applied to the simulated panel via

an applied pressure of p_{max} at 0 ms that linearly decreases to 0 Pa at 15 ms, resulting in a

reflected impulsive of $I = \dfrac{p_{max}}{2} 15$ ms. Validation of the multiscale model is based on

comparing numerical results to physical experiments of a 50.8-mm thick panel

constructed using a UHPC with a 200 MPa unconfined compressive strength and 2%

fiber volume fraction of 14-mm long by 0.185-mm diameter straight, smooth fibers.

Validation of the numerical model is based upon the calculated deflections at mid-height

of panel being with 23% of the physical experiment, fracture patterns, and the

numerically determined critical specific impulse being within the experimentally

determined critical specific impulse.

Using the validated model, a parametric study was conducted to determined the

critical specific impulse as a function of panel thickness at levels of 38.1, 50.4, and 63.5

mm; quasi-static fiber-reinforced tensile strengths at levels of 14.7, 20, and 40 MPa; and

dissipated energy densities at levels of 20, 40, 60, and 80 kJ/m^2. Results indicate that

combinations of panel thickness, quasi-static fiber-reinforced tensile strength, and

dissipated energy density can change the response of the UHPC system from brittle to

ductile, which significantly increases the critical specific impulse of a panel.

CHAPTER 4:

MODEL OF PERFORATION AT THE STRUCTURAL LENGTH SCALE

The response of cementitious materials to ballistic impact is often framed in terms of penetration depth, scabbing limit, perforation limit, and ballistic limit. These four performance metrics are reasonable when considering rebar-reinforced cementitious materials. However, previous research (Dancygier & Yankelevsky, 1996; Zhang et al., 2005) indicates non-reinforced high strength concretes (HSCs) and UHPCs exhibit a more dangerous response: non-reinforced HSCs and UHPCs may shatter, defined as fractures emanating from the site of impact to the edge of the structure causing catastrophic failure (cf. Figure 5), due to impact and subsequent perforation by projectiles. This chapter reviews the response of HSCs and UHPCs to impact and introduces a model at the structural length scale to determine the cause-and-effect relation between the shattering of cementitious panels due to impact and the material properties, e.g. quasi-static tensile strength or dissipated energy density, of the cementitious panel.

A review of published experimental data in the literature indicates the following trends for the ballistic impact of HSCs and UHPCs. First, significant increases in compressive strength of the cementitious material in the panel cause a projectile's residual velocity to decrease slightly. For example, Hanchak et al. (1992) impacted two sets of rebar-reinforced panels – one with $f_c = 48$ MPa, the other with $f_c = 140$ MPa – with 25.4-mm diameter projectiles impacting the panels at velocities between 300 and

1,100 m/s. For the same impact velocity, the residual velocity of a projectile exiting a f_c = 140 MPa panel was only 20% slower than the residual velocity of a similar projectile exiting a f_c = 48 MPa panel. Second, for projectiles not perforating the cementitious panel, the penetration depth and spall diameter, defined as the diameter of the crater on the proximal face due to impact, decrease as the unconfined compressive strength increases up to approximately 115 MPa (Zhang et al., 2005).   For unconfined compressive strengths greater than 115 MPa, the penetration depth and spall diameter were approximately the same as for cementitious panels with f_c = 115 MPa (Zhang et al., 2005).

Previous work suggests that fibers, even at low fiber volume fractions, significantly reduce or eliminate the growth of radial fractures caused by impact. For example, Zhang et al. (2005) observed shattering of $88 \leq f_c \leq 187$ cementitious panels without fibers, whereas a 1.5% fiber volume fraction of 13-mm long by 0.2-mm diameter fibers reduced the propagation of radial cracks such that cementitious panels made from similar materials did not shatter due to the impact of a 15 g projectile traveling between 620 and 700 m/s. Similar results were found by Dancygier and Yankelevsky (1996), who performed impact experiments on 400-mm by 400-mm plates by 40- to 60-mm thick $95 \leq f_c \leq 110$ MPa cementitious panels with and without 0.8% fiber volume fraction of hooked fibers. In addition to reducing shattering of cementitious materials, Zhang et al. (2005) and Dancygier, Yankelevsky, and Jaegermann (2007) experimentally determined that fibers within cementitious materials reduced the spall diameter. However, Zhang et

al. (2005) showed that the penetration depth is relatively unaffected by the presence of 1.5% fiber volume fraction of 13-mm long by 0.20-mm diameter straight, smooth fibers.

4.1 Model of penetration at the structural length scale

A three-dimensional cohesive finite element model at the structural length scale was used to determine if a UHPC panel would fracture due to ballistic impact. As shown in Figure 38, the model consists of a ballistic projectile shaded orange and a UHPC panel shaded gray. The UHPC panel was 304.8-mm wide by 304.8-mm tall by a uniform, but adjustable, thickness t_{panel} between 38.1 and 76.2 mm at increments of 12.7 mm. The model accounts for compressive properties of the UHPC material via bulk elements utilizing Drucker-Prager constitutive relations (cf. Section 3.1.1); tensile and shear are accounted for via zero-thickness cohesive elements which separate bulk elements. The zero-thickness cohesive elements utilize the strain-rate sensitive traction-separation cohesive relation described in Section 3.4.1. The rigid projectile has properties similar to a 0.50 caliber bullet and impacts the center of the UHPC panel's positive x_3 face at an imposed velocity between 900 and 1,000 m/s.
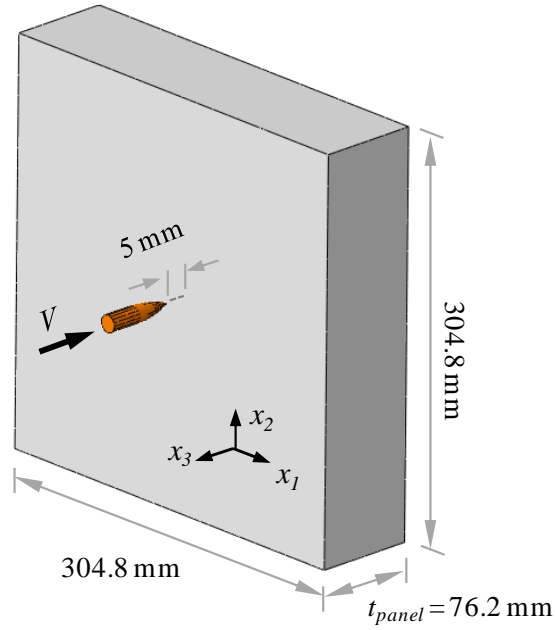
Figure 38. Model of penetration at the structural length scale.

4.1.1   Description of projectile

The projectile was modeled as an analytically rigid three-dimensional part with an ogive-shaped nose, cylindrical body, and center of gravity, CG, as shown in the two-dimensional sketch in Figure 39. The 58.69 mm overall height of a 0.50 caliber bullet (DiPaolo et al., 2012) was reduced to 55.50 mm for the simulated projectile in order to enforce a projectile mass of 42.8 grams and the assumed 7.85-g/cm^3 mass density, ρ. The mass moments of inertia about the center of gravity are defined as

$$I_{11} = \int_V \rho \left(x_2^2 + x_3^2 \right) dV,$$
$$I_{22} = \int_V \rho \left(x_1^2 + x_3^2 \right) dV, \text{ and} \qquad (19)$$
$$I_{33} = \int_V \rho \left(x_1^2 + x_2^2 \right) dV,$$

where x_1, x_2, and x_3 are positioned about the center of gravity of the projectile. The values of I_{11}, I_{22}, and I_{33} used for the simulated projectile were 7,656; 826; and 7,656 g-mm³, respectively.
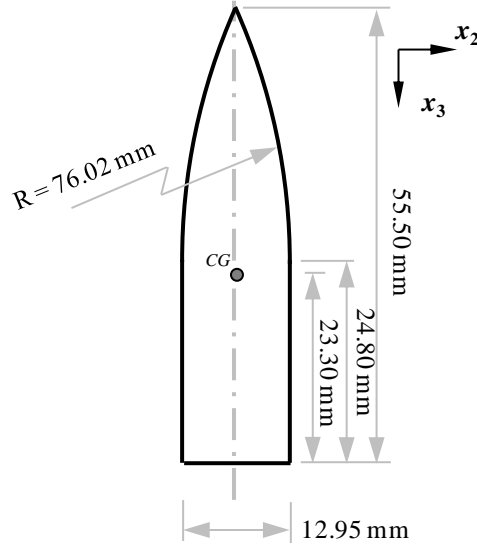
Figure 39. Geometry of modeled projectile.

4.1.2 Boundary and loading conditions

The projectile was initially located such that the tip of the ogive nose was 5 mm from the center of the proximal face of the UHPC panel. The projectile was oriented such that the major axis of the projectile was normal to the plane of the UHPC panel's proximal face. The projectile was linearly accelerated in the negative x_3 direction from an initial velocity of 0 m/s to an imposed velocity V with a fixed magnitude between 900 and 1,000 m/s at 1 μs. After 1 μs, the imposed velocity V was held constant for the duration of the simulation. During the entire simulation, the rigid projectile's remaining 5 degrees of freedom were fixed, thus imposing an obliquity angle of 0°. The UHPC

panel had traction free boundary conditions on all six external surfaces for the entire 150 μs of simulated time.

4.1.3   *Meshing and numerical algorithm*

The UHPC panel was meshed by ABAQUS's native meshing algorithm (Dessault Systemes, 2010) into bulk and cohesive elements. Bulk elements were meshed by 8-node hexahedral reduced integration linear elements with characteristic element sizes depending on the UHPC panel thickness as shown in Table 6. Between any two adjacent bulk elements, zero-thickness 8-node hexahedral cohesive elements were placed to model the traction-separation response. The projectile was meshed by 4-node rigid tetrahedral elements.

Numerical results were generated by ABAQUS/Explicit v6.10-1 and solved on 24 AMD 2350QC processing cores. For a panel thickness of 76.2 mm, processing times varied from 8 to 16 hours for 150 μs of simulated time.

Table 6. Mesh characteristics by panel thickness.

Panel thickness (mm)	Characteristic element size (mm)	Approximate Number of elements	
		Bulk	Cohesive
38.1	4.76	32,800	93,200
50.8	5.08	36,000	103,200
63.5	5.29	40,400	116,300
76.2	5.44	43,900	127,000

4.1.4 Model validation

The model of penetration at the structural length scale was validated using experimental data of Ren, Mattus, Wang, and DiPaolo (2013), who showed that fiber reinforced UHPC samples were perforated, but not shattered, by a 0.50 caliber bullet travelling at 914 m/s. The UHPC material was reported to have nominal $f_c = 185$ MPa and $V_f = 2\%$ of 14-mm long by 0.185-mm diameter steel fibers. The panel dimensions reported by Ren, Mattus, Wang, and DiPaolo (2013), i.e., $304 \times 304 \times 76$ mm^3, are similar to the model. It is assumed that UHPC panels with $V_f = 0\%$ will shatter as a result of impact.

The bulk elements utilize a Drucker-Prager constitutive model described in Section 3.1.1, with material parameters given in Table 7. In Table 7, f_c is the unconfined compressive strength, ρ is the mass density, E is the modulus of elasticity, K is the ratio between the yield stress in triaxial tension and the yield stress in triaxial compression, β is the internal friction angle in the meriodonal plane, and ψ is the dilation angle. The f_c was chosen to match the experimental data of Ren, Mattus, Wang, and DiPaolo (2013), and ψ was chosen to match experimental results of Park, Xia, and Zhou (2001). The sources for all other material parameters match those described in Section 3.1.1.

Table 7. Material parameters for validating the impact model.

f_c (MPa)	ρ (g/cm^3)	E (GPa)	K	β (^{o})	ψ (^{o})
185	2.57	56.9	0.8	28	22

The cohesive elements utilize the strain-rate sensitive traction-separation relation described in Section 3.4.1. The material properties utilized for validation of the model are given in Table 8. In Table 8, E is the stiffness of the cohesive elements; $T_{n,s,t}^0$ is the quasi-static tensile strength in the n, s, and t directions; and $G_{n,x,t}^{V_f=0\%}$ and $G_{n,s,t}^{V_f=2\%}$ are the dissipated energy densities for UHPCs containing $V_f = 0\%$ and $V_f = 2\%$, respectively. Values for $T_{n,s,t}^0$, $G_{n,s,t}^{V_f=0\%}$, and $G_{n,s,t}^{V_f=2\%}$ were obtained from the model at the multiple fiber length scale for 0.185-mm diameter by 14-mm long fibers at their respective volume fractions.

Table 8. Material parameters of cohesive elements used for validating penetration model.

E	$T_{n,s,t}^0$	$G_{n,s,t}^{V_f=0\%}$	$G_{n,s,t}^{V_f=2\%}$
(GPa)	(MPa)	(kJ/m^2)	(kJ/m^2)
200	11.7	0.1	13.5

The model was validated by confirming that an instantiation using $G_{n,s,t}^{V_f=0\%}$ fractures, whereas an instantiation using $G_{n,s,t}^{V_f=2\%}$ does not fracture. Both instantiations are impacted by projectiles traveling at 914 m/s at the time of impact. Results of the two validation instantiations are shown in Figures 37a and 37b, which show the displacement magnitudes of UHPC panels utilizing $G_{n,s,t}^{V_f=0\%}$ and $G_{n,s,t}^{V_f=2\%}$, respectively, 150 μs after impact. The isometric view in the left of each figure shows the proximal face of the UHPC panel and the resulting spall; the side view in the right of each figure shows the spall from the proximal face and the larger diameter scab material from the distal face of

the panel. As shown in the left of Figure 37a, the panel utilizing $G_{n,s,t}^{V_f=0}$ shows evidence

of large displacements in the x_1 and x_2 directions emanating from the center of the panel.

These large displacements are indicative of fracture and are precursors to the panel

shattering. In contrast, Figure 37b exhibits relatively small displacement magnitudes,

except at a local region within approximately 85 mm of the point of projectile impact.
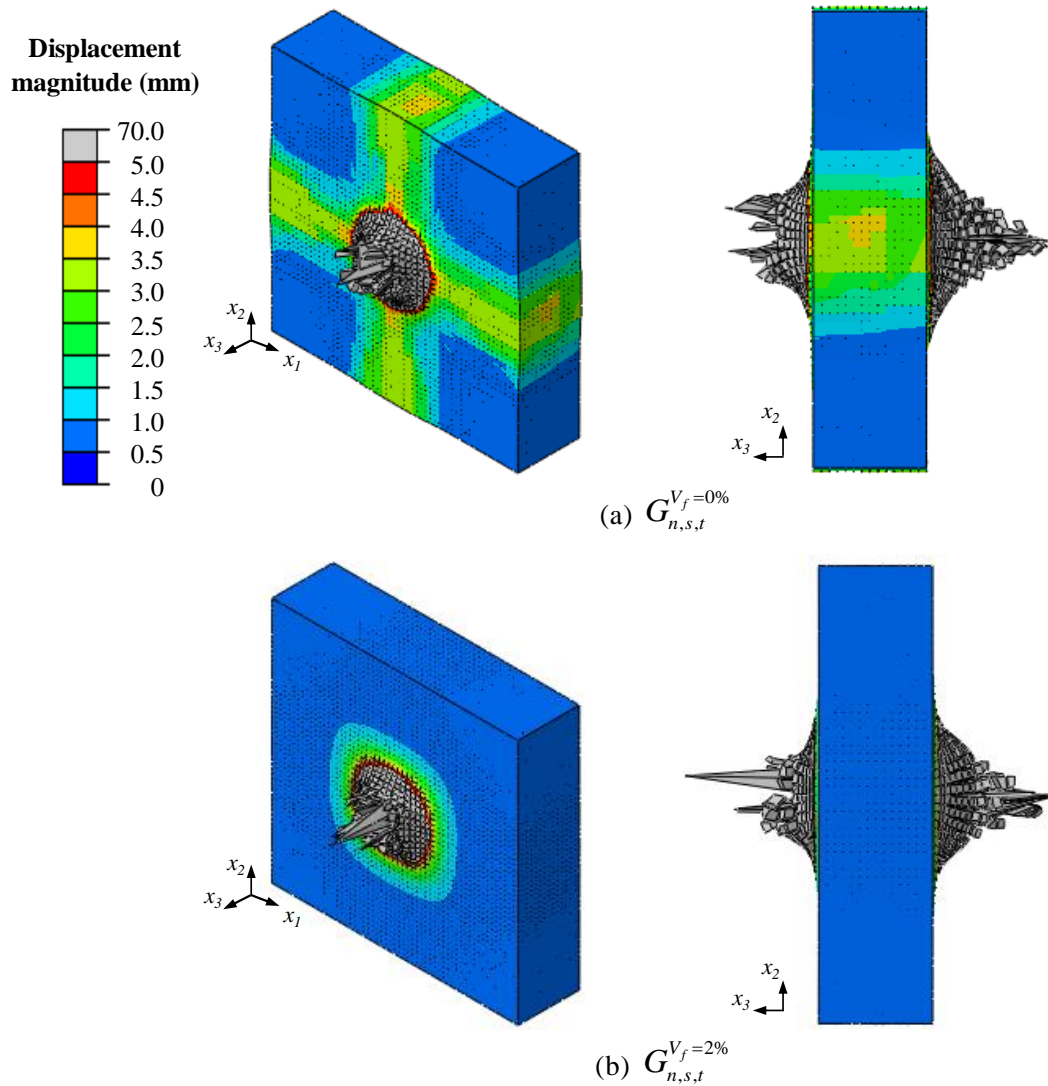
(a) $G_{n,s,t}^{V_f=0\%}$

(b) $G_{n,s,t}^{V_f=2\%}$

Figure 40. Displacement magnitudes for UHPC panels reinforced with (a) $G_{n,s,t}^{V_f=0\%}$ and (b) $G_{n,s,t}^{V_f=2\%}$ of 0.185-mm diameter by 14-mm long steel fibers. Images are shown 150 μs after impact of a projectile with a velocity of at 914 m/s.

A clearer view of the orientation and position of fracture within the UHPC panels can be seen in Figure 41, which shows the evolution of cohesive damage in simulated UHPC panels utilizing $G_{n,s,t}^{V_f=0\%}$ and $G_{n,s,t}^{V_f=2\%}$. The cohesive damage in the $G_{n,s,t}^{V_f=0\%}$ microstructure instantiation indicates severe damage at the center of the panel indicating the ejection of mass from the proximal face of the panel. Surrounding the severe damage at the center of the panel, there are a large number of bands of cohesive damage, indicating the shattering of the panel. The cohesive damage of the $G_{n,s,t}^{V_f=2\%}$ microstructure instantiation also indicates severe cohesive damage at the center of the panel, indicating the ejection of mass from the proximal face. However, the $G_{n,s,t}^{V_f=2\%}$ microstructure instantiation does not indicate connected bands of cohesive damage emanating from the site of impact. Therefore, for the two instantiations examined, the penetration model is capable of discriminating between shattered perforation and intact perforation responses.
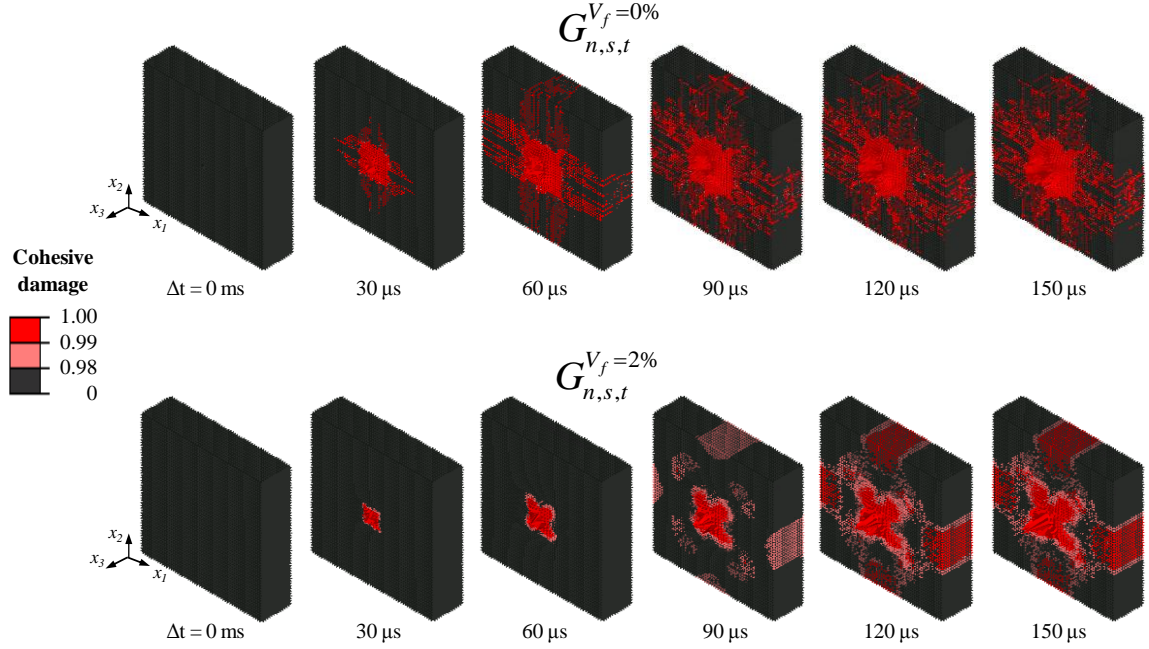
Figure 41. Evolution of cohesive damage for simulated UHPC panels reinforced dissipated energy densities $G_{n,s,t}^{V_f=0\%}$ and $G_{n,s,t}^{V_f=2\%}$, which represent V_f = 0 and 2% of 0.18-mm diameter by 14-mm long steel fibers. Both simulated panels were 76.2-mm thick with $T_{n,s,t}^o$ = 11.7 MPa and impacted by a projectile with a velocity of 914 m/s.

4.2   Results

The penetration model at the structural length scale was used to determine if a simulated panel fractured or remained intact during perforation by projectiles travelling at 9000 and 1,000 m/s. Here, fracture is defined as connected bands of cohesive elements having cohesive damage greater than or equal to 0.98 at simulated times of 90 μs. The 90 μs time was chosen because not all the simulations completed the full 150 μs simulated time due to excessive element distortion and interpenetration. Per the validation study, the 90 μs simulated time was adequate for fracture to be evident.

To determine the fracture response of the panel, a parametric study was conducted utilizing 18 combinations of t_{panel} at levels of 38.1, 50.4, and 63.5 mm, $T^0_{n,s,t}$ at levels of 5 and 12 MPa, and $G_{n,s,t}$ at levels of 0.1, 5, and 10 kJ/m². The remaining material parameters were prescribed as a function of $T^0_{n,s,t}$ and are shown in Table 9.

Table 9. Material parameters in impact simulations.

$T^0_{n,s,t}$ (MPa)	f_c (MPa)	E_m (GPa)	$G_{n,s,t}$ (kJ/m²)	ρ_m (kg/m³)
5	80	43.0	0.1	2,400
12	200	58.3	5.0	2,400

Figure 42 shows cohesive damage for the 18 instantiations simulated at 90 µs after impact. In Figure 42, each column has a constant value of $G_{n,s,t}$, which is shown at the top of the column and increases from 0.1 to 10 MPa-mm moving left to right. Each row in Figure 42 represents instantiations with fixed t_{panel} and $T^o_{n,s,t}$ as shown to the right of each row. Of the 18 instantiations, 16 of the instantiations completed at least 90 µs of simulated time; the remaining two instantiations do not have images shown in Figure 42.

$G_{n,s,t} = 0.1$ MPa-mm $G_{n,s,t} = 5.0$ MPa-mm $G_{n,s,t} = 10.0$ MPa-mm

Cohesive damage

	1.00
	0.99
	0.98
	0

(a)   (b)   (c)

$t_{panel} = 38.1$ mm
$T^0_{n,s,t} = 5$ MPa

(d)   (e)   (f)

$t_{panel} = 38.1$ mm
$T^0_{n,s,t} = 12$ MPa

(g)   (h)   (i)

$t_{panel} = 50.8$ mm
$T^0_{n,s,t} = 5$ MPa

(j)   (k)   (l)

$t_{panel} = 50.8$ mm
$T^0_{n,s,t} = 12$ MPa
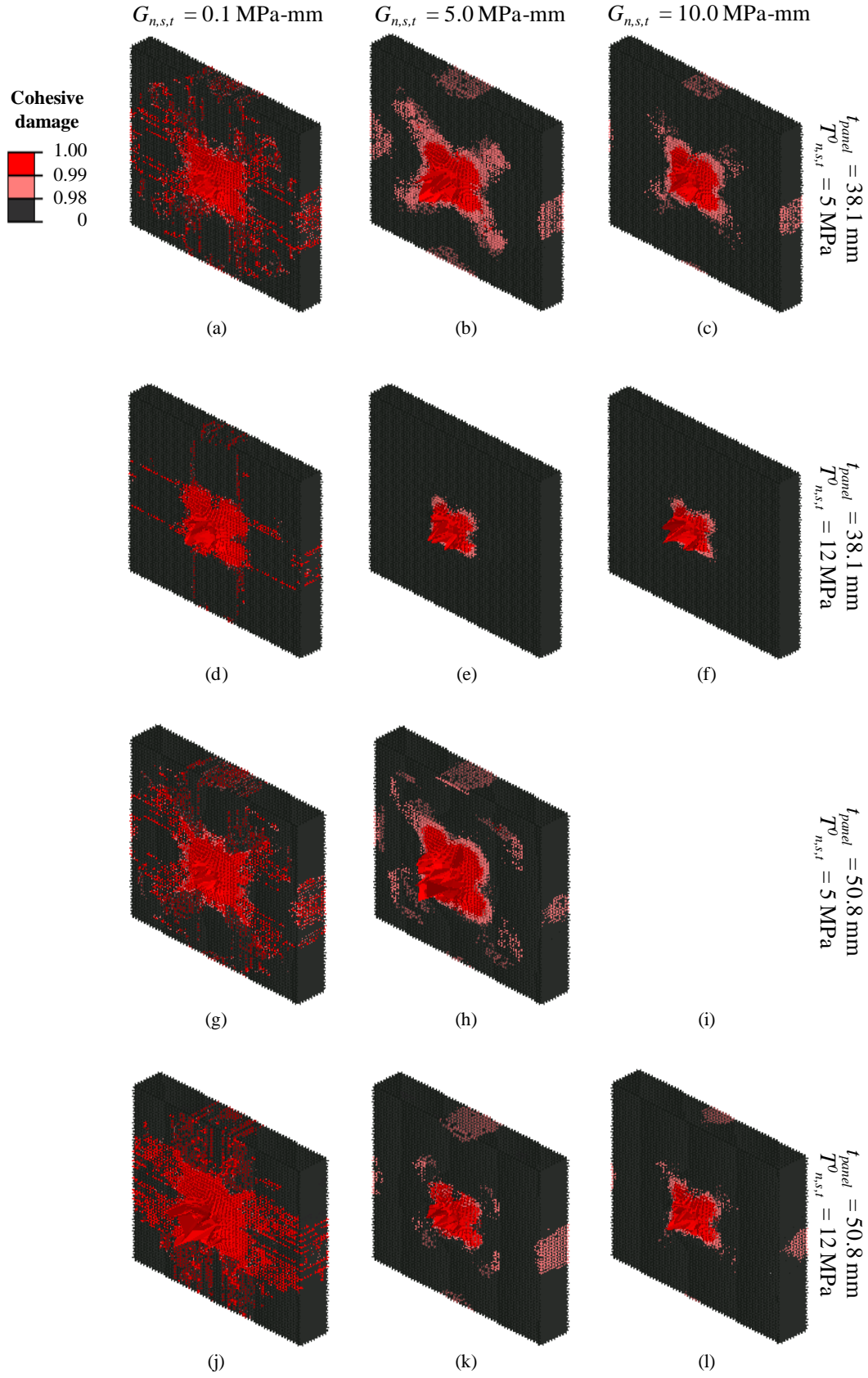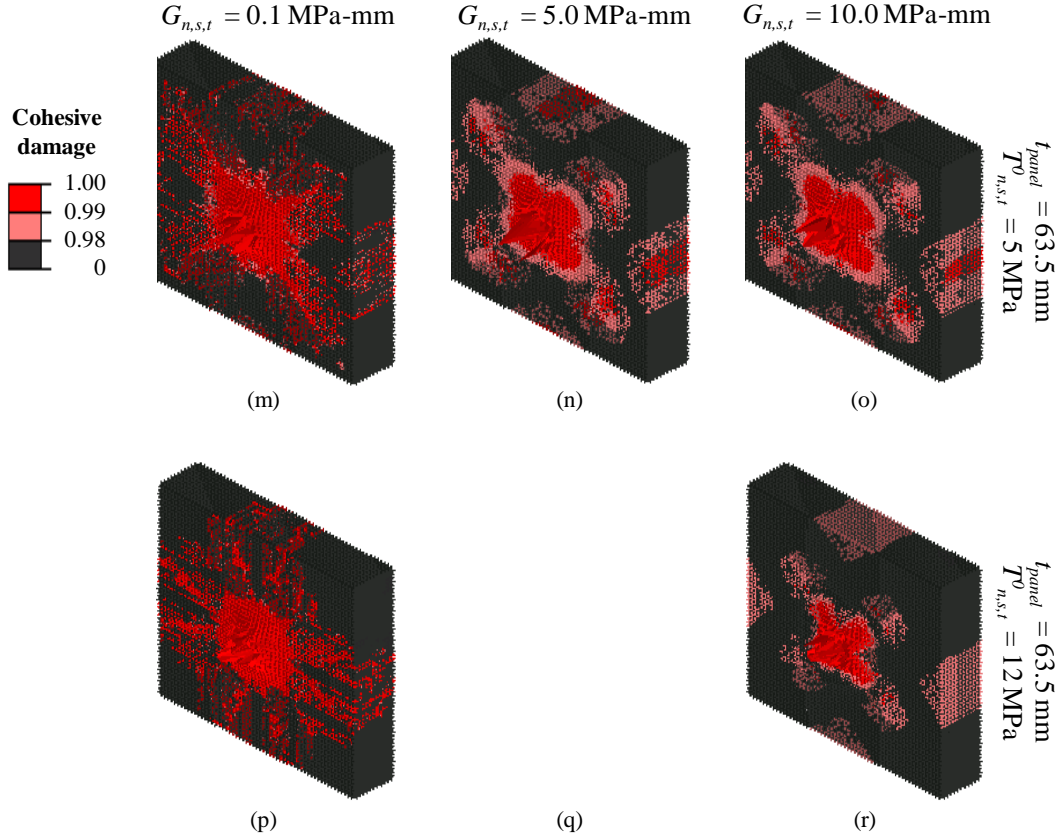
Figure 42. Cohesive damage of simulated UHPC panels 90 μs after the impact of a projectile traveling at 1,000 m/s. The instantiations shown have material properties of $G_{n,s,t} = 0.1$, 5.0, and 10.0 MPa-mm; $T^o = 5$ and 12 MPa; and $t_{panel} = 38.1$, 50.8, and 63.5 mm.

As shown in the left column of Figure 42, all instantiations with $G_{n,s,t} = 0.1$ MPa-mm fractured by or before 90 μs due to the impact of the projectile travelling at 1,000 m/s. In contrast, cohesive damage images for instantiations with $G_{n,s,t} = 5$ and 10 MPa show a lack of interconnected damage, indicating that the panel sustains damage, but does not shatter. Assuming straight, smooth fibers of 0.185-mm diameter and 14-mm length, energy dissipation densities of 5.0 and 10.0 MPa-mm represent fiber volume

fractions of 0.75 and 1.5%, respectively. Results of the simulations are summarized in

Table 10.

Table 10. Results of impact simulations to determine if a simulated UHPC panel fractures
by or before 90 μs after being impacted by a projectile traveling at 1,000 m/s.

Figure 42 subfigure	t_{panel} (mm)	$T_{n,s,t}^0$ (MPa)	f_c (MPa)	$G_{n,s,t}$ (kJ/m^2)	Fractures
a	38.1	5	80	0.1	**yes**
b	38.1	5	80	5.0	no
c	38.1	5	80	10.0	no
d	38.1	12	200	0.1	**yes**
e	38.1	12	200	5.0	no
f	38.1	12	200	10.0	no
g	50.8	5	80	0.1	**yes**
h	50.8	5	80	5.0	no
i	50.8	5	80	10.0	DNF
j	50.8	12	200	0.1	**yes**
k	50.8	12	200	5.0	no
l	50.8	12	200	10.0	no
m	63.5	5	80	0.1	**yes**
n	63.5	5	80	5.0	no
o	63.5	5	80	10.0	no
p	63.5	12	200	0.1	**yes**
q	63.5	12	200	5.0	DNF
r	63.5	12	200	10.0	no

DNF = Simulation did not complete 90 μs.

The legitimacy of the results shown in Table 10 can be judged in comparison to

the experimental results of Zhang et al. (2005) and Dancygier and Yankelevsky (1996).

Zhang et al. (2005) studied the effects of fiber-reinforcement on the impact response of

cementitious panels with f_c ranging between 45 and 225 MPa. The cementitious panels

were reinforced by a 1.5% fiber volume fraction of 13-mm long by 0.2-mm diameter

steel fibers. Results of Zhang et al. (2005) indicate that the 1.5% fiber fraction of the

specified was sufficient to prevent the cementitious panels from shattering. Similar

results were found by Dancygier and Yankelevsky (1996), who measured the impact

response of 400-mm wide by 400-mm tall by 40- to 60-mm thick panels. They found 0.8% fiber volume fraction of 30-mm long by 0.5-mm diameter hooked fibers to be sufficient to prevent cementitious panels from shattering upon impact. The cementitious panels were constructed using materials with f_c ranging from 34 to 104 MPa. The projectiles had a 25-mm diameter, 120-g mass, and impacted the cementitious panels at velocities between 85 and 230 m/s.

4.3   Summary

A three-dimensional Cohesive Finite Element Model (CFEM) of a 304.8-wide by 304.8-mm tall UHPC panel of a uniform, but adjustable, thickness was developed and validated to determine the fracture response of a UHPC panel to ballistic impact. The model was used to determine the fracture resistance of UHPC panels struck by a projectile traveling at 1,000 m/s as a function of panel thickness (38.1, 50.8, and 63.5 mm), uniaxial tensile strength of the fiber-reinforced matrix (5 and 12 MPa), and energy dissipation density (0.1, 5.0, and 10.0 MPa-mm). The 0.1, 5.0, and 10.0 MPa-mm levels of energy dissipation density correspond to 0, 0.75, and 1.5% fiber volume fraction of 0.185-mm diameter by 14-mm long straight, smooth fibers.

For the parameters used in the this study, the model indicates the fracture response of the UHPC panel is highly dependent upon on the energy dissipation density. For example, all instantiations fractured that had energy dissipation densities of 0.1 MPa-mm, whereas all instantiations using energy dissipation densities of 5.0 or 10.0 MPa-mm were perforated but remained intact. From these results, it is concluded that energy dissipation density is the dominant material parameter preventing the fracture of UHPC

panels impacted by projectiles. This conclusion is consistent with experimental data

available in the literature.

CHAPTER 5:

MATERIAL DESIGN

The goal of computational material design is to determine combinations of constituents, properties of materials, and other characteristics (e.g., fiber topologies) that achieve system-level performance requirements. This goal is accomplished by simultaneously solving two distinct paths – a bottom-up deductive modeling and simulation path and a top-down inductive decision path. The bottom-up mappings seek to assemble process-structure-properties-performance (PSPP) relations, which can be found via experimental, analytical, or computational techniques. In this dissertation, the multiscale computational model presented in Chapter 3 is utilized to simulate blast loading to construct the deductive bottom-up set of mappings. The ballistic impact deductive mappings are taken from Chapter 4, at the structural length scale, and the models at the single fiber and multiple fiber length scales in Chapter 3. Deductive mappings between processing conditions, porosity within the paste and ITZ, and the non-fiber-reinforced cementitious matrix are taken from the literature and an analytical model presented in Chapter 4.

In contrast to the bottom-up deductive mappings, the top-down inductive decision path is an entirely different problem with different goals and a different approach to uncertainty. The goal of the inductive decision path is to efficiently determine the constituents, material properties, and other characteristics that satisfy the system-level performance requirements. To achieve this goal, uncertainty within the deductive path is quantified, thus allowing solutions of the inductive decision path to be tolerant of the

effects of uncertainty, or robust. The result of the inductive decision path is the feasible input space, defined as the set of inputs values (e.g., constituents, constituent material properties) that satisfy the system-level requirements. Within the feasible input space, discrete sets of input values are evaluated for system-level goals expressed in terms of objective functions. The objective functions of this work can include the mass of the panel and costs of raw materials. Note that objective functions and system-level performance requirements are fundamentally different: system-level performance requirements must be satisfied for a material design to be feasible, whereas objective functions assign preference to a given design. The notion of preference allows a designer to determine the Pareto frontier, defined as the set of preferred input values within the feasible input space that satisfy performance requirements and goals..

This remainder of this chapter presents the theoretical framework for the material design problem. The sections are as follows. Section 5.1 reviews the classification system of uncertainty. Section 5.2 compares optimal and robust designs. Section 5.3 reviews the theoretical framework for the Inductive Design Exploration Method (IDEM). Section 5.4 presents how IDEM was implemented in MatLab® such that it could be used for materials design. Section 5.5 presents the advantages of using IDEM as the inverse materials design algorithm, and Section 5.6 summarizes this Chapter.

5.1   Uncertainty

Uncertainty is associated with the degree of variability of an input to or response of a system. In the broadest sense, uncertainty is delineated into two categories: aleatory and epistemic. Aleatory uncertainty is inherent to the system and must be quantified in a

statistical sense via moments of probability distribution functions. In contrast, epistemic uncertainty can be reduced by increasing the knowledge of a system via refined measurement techniques or acquiring more samples. The level of epistemic uncertainty is often selected, tacitly or explicitly, based on financial or practical limitations.

For computational materials design using numerical simulations, McDowell, et al. (2009a) suggest a further decomposition of sources of uncertainty, which is an extension of the uncertainty classification presented by Isukapalli, Roy, and Georgopoulos (1998).

- **Natural Uncertainty** (NU) is a subset of aleatory uncertainty quantifying the inherent randomness of the physical system. Natural uncertainty can be further delineated into parameterizable and unparameterizable uncertainty. Parameterizable uncertainty may be expressed as a numeric variance, e.g., the variance in the length of a fiber or the variance in the fiber volume fraction within a statistical volume element. Unparameterizable uncertainty cannot be expressed numerically and is a result of the unknown position and orientation of individual constituents (e.g., fibers, grains) within realized microstructures. As such, unparameterizable uncertainty is related to the size of the chosen statistical volume element.

- **Model Parameter Uncertainty** (MPU) is a subset of epistemic uncertainty resulting from a lack of data related to parameter estimation in the model. Several examples of model parameter uncertainty include the coefficient of friction between steel and concrete, shrinkage coefficients of cementitious materials, elastic modulus of the UHPC used in the blast panels, and strain-rate sensitivity of

119

cementitious materials. Model parameter uncertainty may be reduced by refining the measurement technique or taking more measurements.

- **Model Structure Uncertainty** (MSU) is a combination of aleatory and epistemic uncertainty resulting from the simplifications and approximations in numerical modeling. Although the level of uncertainty can be reduced by refining the assumptions of numerical models, model structure uncertainty cannot be eliminated. Examples of MSU pertaining to the multiscale modeling of blast loaded UHPC panels can be found at each length scale. At the single fiber length scale, three examples of MSU include: (1) the assumed non-strain-softening Drucker-Prager constitutive relation used to represent the response of the ITZ and the matrix; (2) the idealization that the ITZ as a 50 μm uniformly thick, homogeneous material having an elastic stiffness value 80% of the elastic stiffness of the matrix; and (3) the assumption that friction is pressure-independent. At the multiple fiber length scale, two examples of MSU include: (1) the crack plane was represented by a predefined perfectly flat crack surface; and (2) the stress fields in the matrix surrounding individual fibers do not interact. At the coarsest length scale, four examples of MSU include: (1) the assumed linear traction-separation response of fiber-reinforced cementitious materials; and (2) the simplification of the loading conditions to use a linear decaying applied pressure; (3) the Hardwire steel cloth on the distal face was not modeled; and (4) the simplification of the boundary conditions to square steel tubing with sharp corners.

- **Propagated Uncertainty** (PU) is a combination of aleatory and epistemic uncertainty resulting from the propagation of error from one model level to the next. For example, the three-length scale model of the a UHPC blast panel involve the following propagation of uncertainty. Starting at the single fiber length scale, the pullout force versus end slip relation used as an input to the multiple fiber length scale. The uncertainty of the pullout force is propagated to the model at the multiple fiber length scale, which results in homogenized traction-separation relations for a given fiber and fiber volume fractions. These homogenized traction-separation relations, and the uncertainty with the relations are then propagated to the structural length scale.

5.2   Optimal versus Robust solutions

For a given set of input parameters, the presence of uncertainty fundamentally alters a system's response: instead of a single deterministic response, a system will produce a stochastic range of responses. This range of responses alters the type of solutions sought. One possible type of solution is an optimal solution, which seeks to determine the set of input variables that maximize, or minimize, the mean response of the objective function regardless of the variation of the response. The problem with optimal solutions is that uncertainty may cause responses that do not satisfy the system-level performance requirements. Therefore, solutions are sought instead that are robust to the influences of uncertainty.

Robust solutions seek to find sets of input variables with responses that are insensitive to uncertainty while satisfying system-level performance requirements. The three types of robust solutions considered are described below and shown in Figure 43.

- **Type I Robust Solutions** seek a satisfying level of a response function based on insensitivity of response to noise variables, or variables beyond the control of a material designer, while meeting system-level performance requirements (Taguchi, 1992).

- **Type II Robust Solutions** seek a satisfying level of a response function based on insensitivity of the response due to uncertainty of the input variables (Chen et al., 1996).

- **Type III Robust Solutions** seek to the desired performance level while minimizing the effects of uncertainty in the response function (Choi et al., 2005b).
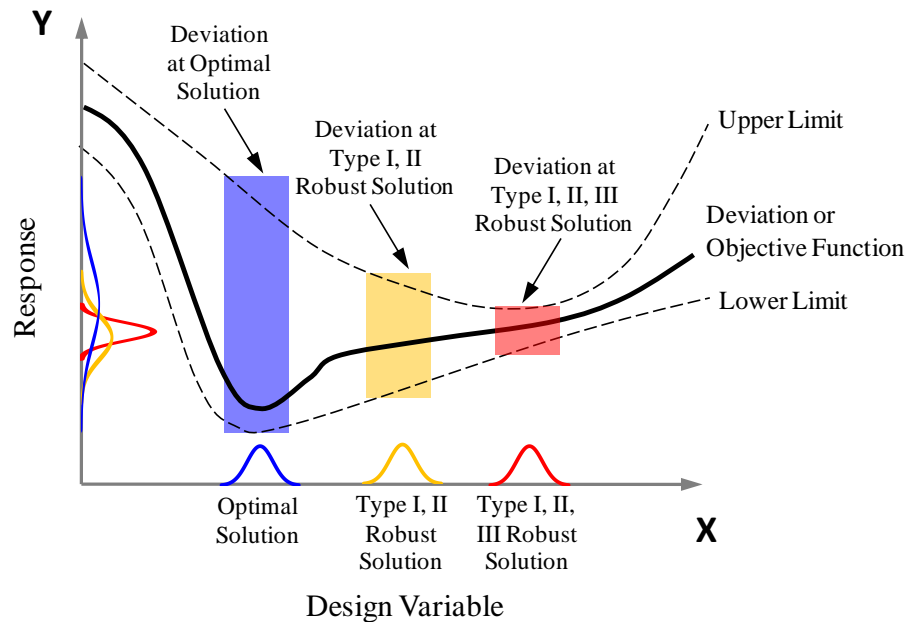
Figure 43. Comparison of optimal and robust solutions (adapted from McDowell et al., 2009a).

The types of robust solutions considered are driven by the computational design of UHPC materials. In particular, Type I and Type II robust solutions are useful for mitigating uncertainty associated with batch processed materials such as UHPC. Type III robustness is critical to account for the assumptions within the computational modeling framework.

5.3   Inductive Design Exploration Method (IDEM)

The inductive decision path is implemented via the Inductive Design Exploration Method (IDEM) (Choi, 2005), which, as shown in Figure 44, is a three-step method that determines feasible values of input variables for a given performance requirement. Between any two spaces, IDEM discretizes input variables, projects each set of discretized input values to a range in the output space, and determines which sets of discrete input values satisfy the output space performance requirements. For example, consider the y- and z-spaces shaded in blue in Figure 44 as the input and output space. The y-space is composed of the y_1 and y_2 input variables with each set of discrete input values, or "input value", show as black dots in Step 1. In Step 2, each input value is projected to the output z-space via the function g. Note that the projection of each input value creates a range of possible results, as indicated by the yellow ellipse in the z-space. In step 3, the range of output in z-space from a single input value is compared to the z-space performance requirement. If the range of output is within the z-space performance requirement, the input value satisfies the performance requirement. Although Figure 44 shows IDEM with three spaces and two variables in each space, IDEM may be

generalized to *m*-spaces with each space having up to *n*-variables, where *m* and *n* are positive integers.
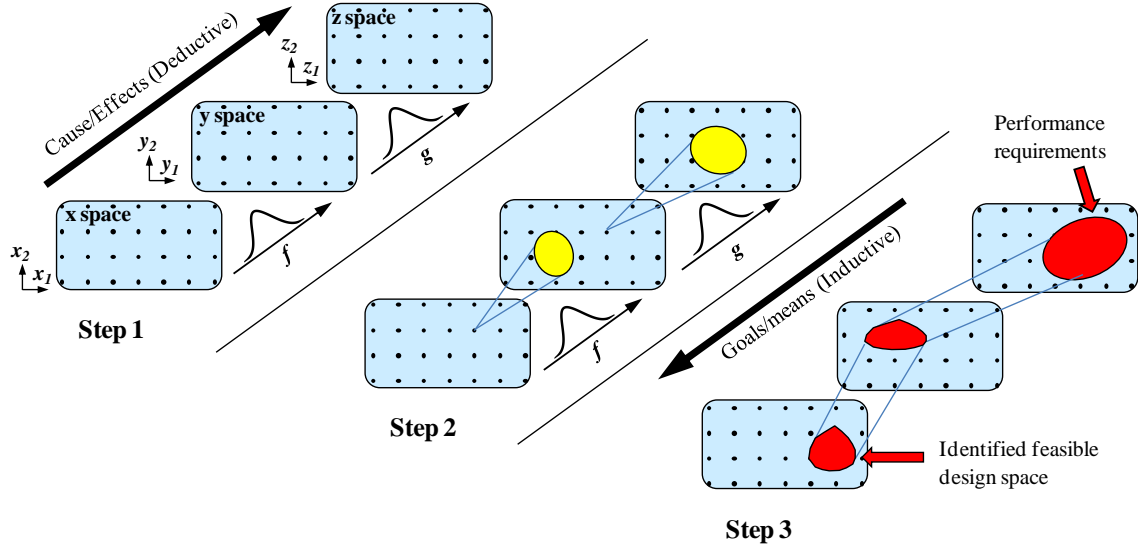
Figure 44. Schematic of Inductive Design Exploration Method (IDEM) applied to a three-space hierarchical problem consisting of x-, y-, and z-spaces. The schematic is shown with two variables in each space.

To determine which sets input values satisfy the output performance requirement, IDEM employs the Hyper-Dimensional Error Margin Index (*HDEMI*). Here, the *HDEMI* of the ith output space variable is defined as

$$HDEMI_i = \begin{cases} min\left[\dfrac{\left\|\left(\mathbf{mean} - \mathbf{B}_j\right)\mathbf{u}_i\right\|}{\left\|\left(\mathbf{mean} - \mathbf{B}_j^i\right)\mathbf{u}_i\right\|}\right], & for\ \mathbf{mean} \in \Omega \\ -1, & for\ \mathbf{mean} \notin \Omega \end{cases} \qquad (20)$$

where i is the number of variables in the output space, j is the number discrete points on a boundary, **mean** is the output value without considering Type I, II, or III uncertainty, $\mathbf{B}_j$ is the output performance requirement composed of j points, $\mathbf{B}_j^i$ is the output boundary of a single input value in the ith output direction, $\mathbf{u}_i$ is a unit vector of the ith

124

variable, and Ω is the feasible output space defined by $\mathbf{B}_j$. Note that $\left\|\left(\mathbf{mean}-\mathbf{B}_j\right)\mathbf{u}_i\right\|$

is the absolute value of the distance between **mean** and the boundary of the projected

input point in direction of the ith output variable. Similarly, $\left\|\left(\mathbf{mean}-\mathbf{B}_j^i\right)\mathbf{u}_i\right\|$ is the

absolute value of the distance between **mean** and the boundary of the output space

projected in the ith direction. Figure 45 shows a graphical representation of the

projection of a discrete set of input values to a range in the output space, thus allowing

the calculation of the $HDEMI_i$. In Figure 45, the feasible output space is shaded red

and the projected output range from a single discrete input value is shaded yellow.

$$HD\_EMI_i = \begin{cases} Min\left[\dfrac{\left\|(\mathbf{mean}-\mathbf{B}_j)\mathbf{u}_i\right\|}{\left\|(\mathbf{mean}-\mathbf{B}_j^i)\mathbf{u}_i\right\|}\right], & for\ \mathbf{mean}\in\Omega \\ -1 & ,\quad for\ \mathbf{mean}\notin\Omega \end{cases}$$
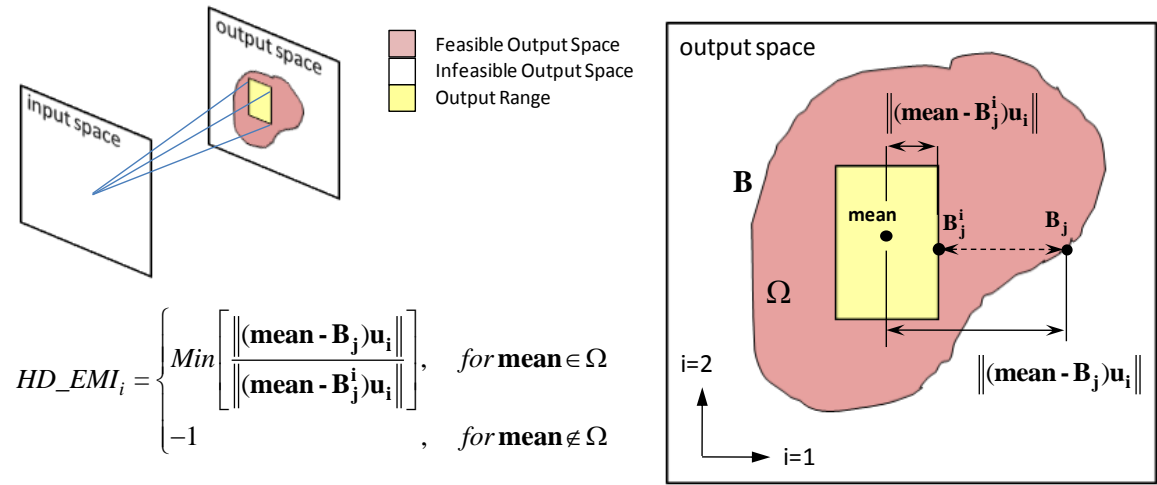
Figure 45. Schematic of the Hyper-Dimensional Error Margin Index (HDEMI) showing the projection of a discrete input value to a range of outputs (adapted from Choi et al., 2008).

The boundary of the output range of a single point, $\mathbf{B}_j^i$, is determined by the type

or types of robustness desired. Given the input space $y=\{y_1,...,y_k,...,y_n\}$, the input

value $y_0 = \{y_{1,0}, ..., y_{k,0}, ..., y_{n,0}\}$ projects to the **mean** output value $z_0 = g(y_0)$, where g

is a function relating y and z. Type II robustness accounts for variations in the output

defined as

$$\Delta z = \sum_{k=1}^{n} \left| \frac{\partial g}{\partial y_k} \right| \Delta y_k, \tag{21}$$

where n is the dimension of the input space, $\left| \dfrac{\partial g}{\partial y_k} \right|$ is the absolute value of the partial

derivative of g with respect to y_k, and Δy_k is the expected variation of the kth input

variable. Type III robustness assumes knowledge of the deviation of the response

function g. Specifically, the lower and upper bound of g are defined as g_{lower} and

g_{upper}. In a similar manner to Eq. (21), the variation of z_0 due to g_{lower} and g_{upper} are

defined as

$$\Delta z_{lower} = \sum_{k=1}^{n} \left| \frac{\partial g_{lower}}{\partial y_k} \right| \Delta y_k, \text{ and}$$

$$\Delta z_{upper} = \sum_{k=1}^{n} \left| \frac{\partial g_{upper}}{\partial y_k} \right| \Delta y_k. \tag{22}$$

The maximum and minimum boundaries of uncertainty accounting for Type II and III

robustness are then defined as

$$z_{max} = Max\{g(y_0) + \Delta y, \ g_{lower}(y_0) + \Delta y_{lower}, \ g_{upper}(y_0) + \Delta y_{upper}\}, \text{ and}$$

$$z_{min} = Min\{g(y_0) - \Delta y, \ g_{lower}(y_0) - \Delta y_{lower}, \ g_{upper}(y_0) - \Delta y_{upper}\}. \tag{23}$$

Finally, the deviation from the nominal value z_0 is found by

$$\Delta Z_{upper} = z_{max} - g(y_0) \text{ and}$$

$$\Delta Z_{lower} = g(y_0) - z_{min}. \tag{24}$$

Input points with *HDEMI* values greater than one indicate the feasible input space; input points with *HDEMI* values less than one indicate the infeasible space. The boundary between the feasible and infeasible spaces have, by definition, *HDEMI* values equal to one. However, the prior discretization of the input space into a set of input points does not guarantee that the prior defined points will lie on the boundary. Thus, points on the boundary must be determined.

Figure 46 illustrates the how the boundary is determined between the feasible input points (shaded in blue) and the infeasible input points (shaded in gray) for a two-dimensional input space. The input space consists of y_1 and y_2 input variables that have been discretized into 4 and 3 points, respectively, with the index of each discretized point shown as a superscript, e.g. y_1^4 represents the fourth discretized point of the y_1 input variable. For each orthogonal direction, the input points are search to find adjacent pairs of points that are feasible and infeasible. If such an adjacent pair of points is found, it is assumed that exactly one boundary point exists between the adjacent points. This boundary point is found via a bisection method.
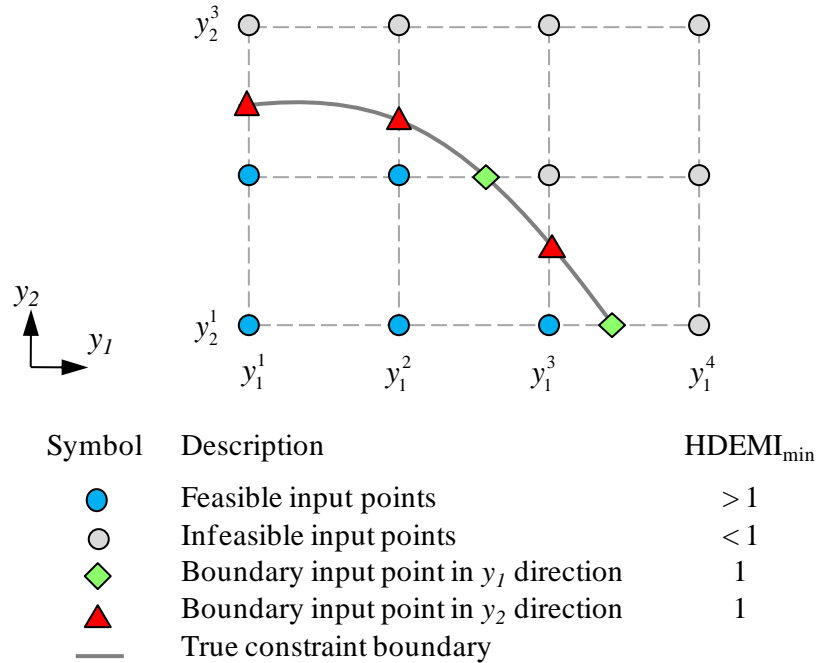
Figure 46. Determination of the input space's boundary for a two-dimensional input space consisting of feasible and infeasible input points.

For design problems containing more than two spaces, the performance at the highest-level space is used to determine the feasible input space at the next-to-highest space. The calculated feasible input space, or more specifically the boundary of the input space, becomes the output performance requirement at the next-finer scale. In this recursive manner, IDEM can be used for problems across multiple spaces or length scales.

5.4   Implementation of IDEM in MATLAB[®]

To implement IDEM, a computer program was written and validated in the MATLAB[®] programming language. The MATLAB programming language was chosen due to its integrated graphics capabilities, symbolic mathematical operator, and

widespread availability. The program's flow chart in Figure 47 highlights the algorithm and structure of the program, which consists of the main script, *IDCE.m*, and three functions: *fHDEMIPrep.m* , *fHDEMI.m*, and *bHDEMI.m*.

The remainder of this section provides details pertaining to the main script and function calls within the program. For clarity, the `Courier New font` will be used in the remainder of this section to identify verbatim symbols or text taken from the MATLAB program.

```
Start
```

User Input:
1.) Response Functions
$$f, f_{upper}, f_{lower}$$
2.) Input Variables
$$x = \{x_1, x_2, ..., x_i, ..., x_n\}$$
3.) Uncertainty of Input Variables
$$\Delta x = \{\Delta x_1, \Delta x_2, ..., \Delta x_i, ..., \Delta x_n\}$$
4.) Discretization of Input Variables
$$dx = \{dx_1, dx_2, ..., dx_i, ..., dx_n\}$$
5.) Performance Requirements

Function: *fHDEMIPrep.m*
Calculate Partial derivatives
$$\frac{\partial f}{\partial x_i}, \frac{\partial f_{upper}}{\partial x_i}, \frac{\partial f_{lower}}{\partial x_i}$$

Loop through discretized sets of Input Variables

Function: *fHDEMI.m*
Find HDEMI values
$$HDEMI_i = \begin{cases} Min\left[\frac{\|(\text{mean} - \mathbf{B_j})\mathbf{u_i}\|}{\|(\text{mean} - \mathbf{B_j^i})\mathbf{u_i}\|}\right], & for\,\text{mean} \in \Omega \\ -1, & for\,\text{mean} \notin \Omega \end{cases}$$

All Points Complete?

No

Yes

Function: *bHDEMI.m*
Determine boundary points where HDEMI = 1

1.) Display Input Space with Satisfying and Unsatisfying domains and boundary points
2.) Record boundary points to array for future other input

```
End
```

Figure 47.   Flow chart of MATLAB® program for calculating the feasible input spaces for linear and nonlinear response functions.

5.4.1 **MATLAB script:** *IDCE.m*

The main script for the IDEM program, named *IDCE.m*, contains the five

different inputs that will need to be adjusted for design problems containing up to three

variables. Note that IDCE.m and the three functions automatically adjust to the number

of input variables entered by the user. To change the program for a different design

problem, the following five inputs must be changed.

- **Symbolic input variables** are the symbolic names given to the input variables. In

  IDCE.m, the symbolic names are declared after the `syms` command using all

  upper-case letters. The upper-case letters are not required, but are convenient for

  distinguishing between the symbolic variable name and the vector of discretized

  input values given the same name in lower-case letters. After updating the names

  of the symbolic input variables, the new symbolic input variables names must be

  entered as arguments of the `VAR` vector. For example, Figure 48 contains

  example code for defining the three symbolic input variables to

  `DISSIPATEDENERGY`, `STRENGTH`, and `THICKNESS`.

```
syms DISSIPATEDENERGY
syms STRENGTH
syms THICKNESS

VAR=[STRENGTH DISSIPATEDENERGY THICKNESS];
```

Figure 48. Example code for declaring the name of the symbolic input variables.

- **Discretized input vectors** are vectors that discretize the symbolic input variables into the desired values. In *IDCE.m*, the discretized input vectors are adjusted by defining a vector using the same name as the symbolic input variables, but given in all lower-case. If the names of any of the discretized input vectors are changed, the names of the discretized vectors should be updated in the v vector. Note that the sequence of the symbolic input variables listed in VAR and the sequence of discretized input vectors listed in v must match. Figure 49 gives example code for defining for the discretized input vectors that match the symbolic input variables given in Figure 48. As defined in Figure 49, the thickness vector will be equal to (39, 45, 51, 57, 63).

```
dissipatedenergy=(20:5:80); % Dissipated energy density (MPa-mm)
strength=(11:0.5:18);       % Quasi-static tensile strength (MPa)
thickness=(39:6:63);        % panel thickness (mm)

v=[{strength} {dissipatedenergy} {thickness}];
```

Figure 49. Example code for defining the discretized input vectors.

- **Uncertainty of input variables** is the amount of uncertainty of the discretized input vector expressed in the same units as the variables in the discretized input vector and as a absolute value of the deviation. As such, the uncertainty of input variables accounts for Type II Robustness. In *IDCE.m*, the discretized input error is specified by the ie1, ie2, and ie3 variables.

132

- **Response functions** are the nominal, upper, and lower response functions, which have determined from either numerical simulations, analytical models, or experimental data. In *IDCE.m*, the nominal, upper, and lower response functions are specified by the `f`, `fmax`, and `fmin` variables in terms of the symbolic input variables. It is through `fmax` and `fmin` that IDEM accounts for Type III Robustness. An example code is given in Figure 50 for defining the three different response surfaces.

```
f = 0.0668 ...
    + 0.0074*THICKNESS + 0.0081*STRENGTH ...
    - 0.0282*DISSIPATEDENERGY + 0.0004*THICKNESS*STRENGTH ...
    + 0.0000*STRENGTH*DISSIPATEDENERGY   ...
    + 0.0010*DISSIPATEDENERGY*THICKNESS;

fmax=0.0678 ...
    + 0.0074*THICKNESS + 0.0081*STRENGTH ...
    - 0.0282*DISSIPATEDENERGY + 0.0004*THICKNESS*STRENGTH ...
    + 0.0000*STRENGTH*DISSIPATEDENERGY ...
    + 0.0010*DISSIPATEDENERGY*THICKNESS;

fmin=0.0668 ...
    + 0.0074*THICKNESS + 0.0081*STRENGTH ...
    - 0.0282*DISSIPATEDENERGY + 0.0004*THICKNESS*STRENGTH ...
    + 0.0000*STRENGTH*DISSIPATEDENERGY ...
    + 0.0010*DISSIPATEDENERGY*THICKNESS;
```

Figure 50. Example code for defining the nominal, maximum, and minimum response functions.

- **Performance Requirements** are the requirements that the range of responses must satisfy for the discrete input to be considered part of the feasible input space. For simple cases involving a single response, the upper and lower performance

133

requirements are set by the `fusl` and `flsl` variables. For single-sided

performance requirements, set the non-necessary performance requirement

variable to be equal to `NoSL`. For example, if the performance requirement is that

the material must have a tensile yield strength greater than or equal to 100 MPa,

the performance requirement should be specified as `flsl=100` and `fusl=NoSL`.

For more complicated performance requirements which might be encountered in

inductive decision paths containing three or more levels of hierarchy, a set of

boundary points to the feasible domain is imported from the previous level of

hierarchy. The boundary points stored in `Bnd2Plot` are used to define a surface

inside which are points that satisfy the performance requirements. Should the

performance requirements consist of more than one contiguous domain, *IDCE.m*

needs to be run separate times for each contiguous domain.

In addition to the five items listed previously, there are four variables – `vlabel1`,

`vlabel2`, `vlabel3`, and `cHDEMI` – that need to be defined for labeling axes and titles of

the graphical output.

5.4.2 **MATLAB function:** *fHDEMIPrep.m*

The function *fHDEMI.m* prepares response functions to be used within the

IDCE.m script by calculating the symbolic partial derivatives of any function with respect

to the symbolic variables listed in the *n*-length `VAR` vector. The function requires two

input arguments: (1) a response function (e.g. `f`, `fmax`, or `fmin`); and (2) a vector of

symbol variables used in the response function, i.e., the `VAR` vector. The

fHDEMIPrep.m function returns a $n+1$ length cell of anonymous functions where the first element in the cell is the anonymous function of the response function and the 2nd through $n+1$ elements are anonymous functions of the partial derivatives of the variables listed in VAR, i.e.,

$$
\begin{aligned}
\texttt{fHDEMI(f,VAR)\{1\}} &= \texttt{f} \\
\texttt{fHDEMI(f,VAR)\{2\}} &= \frac{\delta\texttt{f}}{\delta\texttt{VAR(1)}} \\
&\vdots \\
\texttt{fHDEMI(f,VAR)\{n+1\}} &= \frac{\delta\texttt{f}}{\delta\texttt{VAR(n)}}.
\end{aligned}
\tag{25}
$$

In MATLAB, cells are similar to vectors in that they can store variables or numbers, but cells may also store text strings and anonymous functions. Hence, cells are a generalized form of a vector. The term anonymous function refers to a class of functions that are defined within scripts and do not require a standalone file. As such, anonymous functions are more flexible than traditional functions and can as elements in a cell.

5.4.3 MATLAB function: *fHDEMI.m*

For input points whose responses must satisfy a scalar interval, the function *fHDEMI.m* calculates the value of *HDEMI* for each discrete set of input values. The function requires five arguments: (1) an array of anonymous functions in the sequence

$$
\begin{aligned}
&\texttt{f}, \; \frac{\delta\texttt{f}}{\delta\texttt{VAR(1)}}, \; \dots, \; \frac{\delta\texttt{f}}{\delta\texttt{VAR(n)}}, \\
&\texttt{fmax}, \; \frac{\delta\texttt{fmax}}{\delta\texttt{VAR(1)}}, \; \dots, \; \frac{\delta\texttt{fmax}}{\delta\texttt{VAR(n)}}, \\
&\texttt{fmin}, \; \frac{\delta\texttt{fmin}}{\delta\texttt{VAR(1)}}, \; \dots, \; \frac{\delta\texttt{fmin}}{\delta\texttt{VAR(n)}},
\end{aligned}
\tag{26}
$$

where n is the length of the `VAR` vector; (2) an n-length vector of the discrete input values to calculate the HDEMI value for; (3) an n-length vector of the uncertainties associated with each discrete input value; (4) the lower performance requirement; and (5) the upper performance requirement. If the mean response is outside of the performance requirements, *fHDEMI.m* returns a scalar value of -1. Otherwise, *fHDEMI.m* returns the scalar result of Eq. (20).

The *fHDEMI.m* function is first called by *IDCE.m* to determine the values of HDEMI for each set of discretized input values. After HDEMI values for each discrete input value have been calculated, *fHDEMI.m* is called by *bHDEMI.m* to determine the HDEMI value of midpoint value during a bisection root-finding method.

For responses having performance requirements defined as a series of points in an m-dimensional space, *fHDEMI.m* is not called. Instead, the list of boundary points `BndPoints` and feasible points `FeasPoints` defining the performance requirement are used to define an m-dimensional Delaunay triangulation. The Delaunay triangulation is then used to determine HDEMI values per Eq. (20) in the m-dimensional space.

5.4.4 MATLAB function: *bHDEMI.m*

Given a performance requirement for an output space, the function *bHDEMI.m* is determines the boundary points, i.e., points such that HDEMI equals one, between the feasible and infeasible input spaces. To accomplish this task, *bHDEMI.m* employs a bisection method up to a finite number, `kmax`, of iterations.

The function *bHDEMI.m* requires eight arguments: (1) the array of anonymous functions specified in Eq. (26); (2) an n-length vector specifying a feasible input point,

where n is the length of `VAR`; (3) an *n*-length vector specifying an infeasible input point that is adjacent to the feasible input point; (4) an *n*-length vector specifying the uncertainty of the feasible and infeasible input points, which are assumed to have the same uncertainty; (5) lower performance requirement; (6) upper performance requirement; (7) upper bound of the allowable HDEMI value, `HTP`, which is typically set equal to 1.005; (8) lower bound on the allowable HDEMI value, `HTM`, which is typically set equal to 0.995. If the bisection method finds a boundary point, y_{bp}, with an HDEMI value between `HTM` and `HTP` with fewer iterations than `kmax`, the function returns y_{bp} as an *n*-length vector. If a root of the equation is not determined before the maximum number of iterations, *bHDEMI.m* returns with an error.

5.5   Advantages of using IDEM in computational materials design

Computational materials design using IDEM has several advantages over other approaches. First, IDEM is capable of determining either optimal or robust solutions. As previously mentioned, robust solutions offer significant advantages for batch processes such as the manufacture of NSCs and UHPCs. Second, IDEM separates the hierarchical design problem into tasks between each level of hierarchy. By separating the hierarchical design problem to tasks at each level, changes to the range of the input space, discretization of the input space, or the response function between input space and the output space can be made quickly. This is especially important in multilevel designs because only the input and output spaces of interest need to be recalculated. Third, IDEM is parallelizable due to its modular nature. Fourth, IDEM is well suited to design problems at the early stages of design. It is often in the early stages of design that

137

significant portions of time are lost due to trying to determine the optimum of a local extremum, without understanding if the extremum satisfies the system-level requirements.

5.6   Summary

The materials design process consists of bottom-up mappings and top-down inductive decision path which must be solved simultaneously. The bottom-up deductive mappings seeks to accurately determine relations between causes and effects via experimental data, analytic models, or computational models. The inductive decision path seeks to efficiently determine feasible input spaces that satisfy the system-level performance objectives. Whereas the deductive mappings seek to employ accurate relations, the inductive decision path seeks to mitigate the effects of uncertainty.

Uncertainty can be classified as aleatory uncertainty, defined as the irreducible uncertainty that can only be quantified in a statistical sense, or epistemic uncertainty, which can be reduced via a larger number of measurements or more accurate measurements. For purposes of computational materials design, uncertainty is further classified into Natural Uncertainty, Model Parameter Uncertainty, Model Structure Uncertainty, and Propagated Uncertainty. The presence of uncertainty motivates the choice of robust solutions instead of optimal solutions.

The three types of robust solutions considered are Type I, Type II, and Type III. Type I robust solutions seek to find values of input variables that satisfy system-level performance requirements with account of noise variables. Type II robust solutions seek to values of input variables that satisfy the performance objectives with account for

uncertainty in the value of the input variables. Type III robust solutions seek to find values of input variables that satisfy performance objections with account for uncertainty in the response functions.

Robust solutions are implemented in the inductive decision path via the Inductive Design Exploration Method (IDEM) (Choi et al., 2008), which is a systematic three-step method that determines feasible values of input variables for a given performance requirements. Between any two spaces, IDEM discretizes the input space into points, projects each input point to a range of output in the output space, and determines if each input point satisfies the output space's performance requirement. The set of input points satisfying the performance objective are defined as the feasible input space, around which a boundary is defined. The design of multiscale materials is possible by recursive applications of IDEM, in which the boundary of the feasible input space at the coarser level of hierarchy becomes the performance requirement at the finer level of hierarchy.

IDEM was programmed and verified in the MATLAB$^{\circledR}$ programming language for responses having up to three input variables, which had to satisfy three performance requirements simultaneously. Details of the MATLAB program are listed in this dissertation such that the IDEM code can be used by other researchers.

IDEM is well suited to the computational materials design process because it: (1) can determine either optimal or robust designs; (2) separates hierarchical design problems into a systematic three-step algorithm which can be applied recursively for multilevel problems; (3) can be implemented in a parallelized computational environment due to its modular nature; and (4) finds ranges of feasible solutions, which is important at the early stages of design.

CHAPTER 6:

APPLICATION: DESIGN OF UHPC MATERIALS AND

STRUCTURES FOR BLAST AND IMPACT

This chapter applies the materials design methodology presented in Chapter 5 to the design of UHPC materials and structures. The design problem is divided into two steps. The first step is to determine the feasible input space of constituent attributes, constituent properties, processing conditions, and panel thickness such that a 1,625.6-mm tall by 863.6-mm wide UHPC panel (cf. Figure 24) survives blast loading and a 304.8-mm tall by 304.8-mm wide panel made of the same UHPC material and to the same thickness as the blast panel survives ballistic impact. The second step is to identify preferred solutions that satisfy the performance requirements and are preferred in terms of objective functions that may include mass or cost of the panel.

The sections of this Chapter are as follows. Section 6.1 defines the performance requirements for the two objectives considered. Section 6.2 presents the Process-Structure-Properties-Performance (PSPP) mapping used for the design of UHPC materials. Sections 6.3, 6.4 and 6.5 detail the process-structure, structure-property, and property-performance relations, respectively. Section 6.6 presents results of the feasible design space as well as minimized mass and minimized costs solutions. Section 6.7 summarizes the chapter and presents conclusions.

6.1   Multifunctional performance requirements

6.1.1   *Blast loading*

The performance requirement for "blast loading" is defined such that a 1,625.6-mm tall by 863.6-mm wide UHPC panel should survive, i.e., not fracture into two or more pieces, a blast load with a specific impulse, I, between 1.25- and 1.5-MPa-ms.

The UHPC panel's response, i.e., either survive the blast load or fracture due to the blast load, is determined using the computational model for blast loading at the structural length scale (cf. Chapter 3.4), which is shown in Figure 51. In the model, the blast load is applied to the proximal face with a pressure $p_{\max} = \dfrac{2I}{15 \text{ ms}}$ at 0 ms and linearly decreases to 0 Pa at 15 ms. Prior to and during blast loading, the simulated panel is constrained by four restraints (shaded gray in Figure 51) modeled with a linear elastic constitutive relation utilizing a 200-MPa Young's modulus, 0.3 Poisson ratio, and 7.85-g/cm^3 mass density.   The back restraint in the positive x_2 direction is fixed on its positive x_2 face; the back restraint in the negative x_2 direction is fixed on its negative x_2 face. All four restraints are fixed at their positive and negative x_1 faces. In this manner, the boundary conditions are similar to, but not exactly the same as, "simply supported" boundary conditions.

The UHPC panel is modeled using bulk elements separated by zero-thickness cohesive elements. The bulk elements utilize the Drucker-Prager constitutive relation, described in Section 3.1.1 of this dissertation, with a 200-MPa unconfined compressive strength, 2.57-g/cm^3 mass density, 58.4-GPa Young's modulus, 28° internal friction

angle, 20º dilation angle, and $K = 0.8$. Between each adjacent pair of bulk elements, a zero-thickness cohesive element is placed to simulate fiber pullout. The zero-thickness cohesive elements utilize the strain-rate sensitive traction-separation relation described in Section 3.4.1 of this dissertation. Cohesive elements use a stiffness of 200 GPa, quasi-static tensile strength values between 10 and 20 MPa, and dissipated energy density values between 20 and 100 kJ/m^2. Prior to the application of blast loads, the panel is assumed to be as manufactured, i.e., neither perforated due to ballistic impact nor containing damaged cohesive elements.
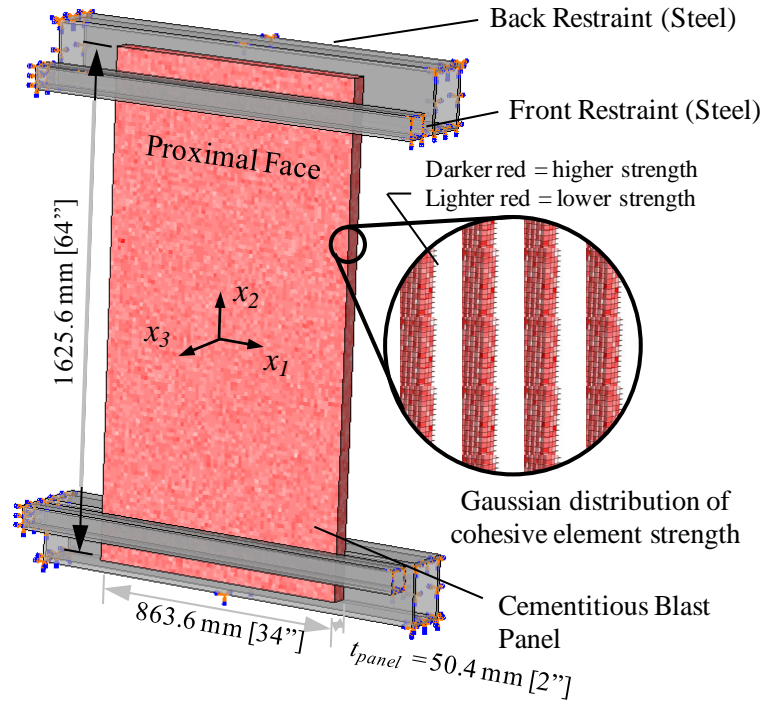
Figure 51. Model of blast loading at the structural length scale.

6.1.2 Impact loading

The performance requirement for "impact loading" is that a 304.8-mm tall by 304.8-mm wide panel made from the same material and the same thickness as the blast panel must not completely fracture due to the impact of a 0.50-cal bullet (12.95-mm diameter, 58.67-mm length, and 42.8-g mass (DiPaolo et al., 2012)) traveling between 900 and 1,000 m/s and striking the panel at an obliquity angle of 0º. The performance requirement limits neither perforation nor penetration of the UHPC panel by the projectile.

The UHPC panel's response is simulated by the model of penetration at the structural length scale (cf. Chapter 4), which is shown in Figure 52. In the model, the simulated projectile (shaded in orange) impacts the center of the positive x_3 face of the simulated UHPC panel (shaded in gray) at imposed velocities between 900 and 1,000 m/s. The projectile is modeled as a rigid part; the UHPC panel is modeled using the same arrangement and material properties as the bulk and cohesive elements in the blast model at the structural length scale. The UHPC panel has traction free surfaces on all six exterior faces.
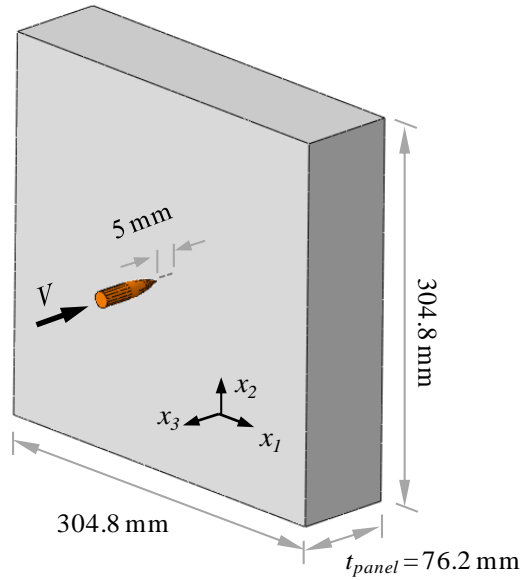
Figure 52. Model of penetration at the structural length scale.

6.2   Process-structure-properties-performance (PSPP) Map

To employ the Inductive Design Exploration Method (IDEM), a set of process-structure-property-performance (PSPP) mappings must be defined. Here, it is assumed that the PSPP mappings shown in Figure 53 define the relevant relations for the design of UHPC for the multifunctional objectives considered. In Figure 53 , cause-and-effect relations are read from left to right and designated by straight lines without arrows. The arrows in the processing path indicate a time sequence, not cause-and-effect relations. Some of the process parameters are surrounded by parentheses, indicating that the process parameter is listed for a reference, rather than as inputs to cause-and-effect relationships. The PSPP mappings for structures, properties, and performance are separated into micro-, meso-, and macro-scale relations, which allows delineation of the PSPP mappings for a multiscale material such as UHPC. For each of the process-

144

structure, structure-property, or property-performance relations shown in Figure 53, a relation is defined analytical models or numerical modeling which have been validated by experimental data.
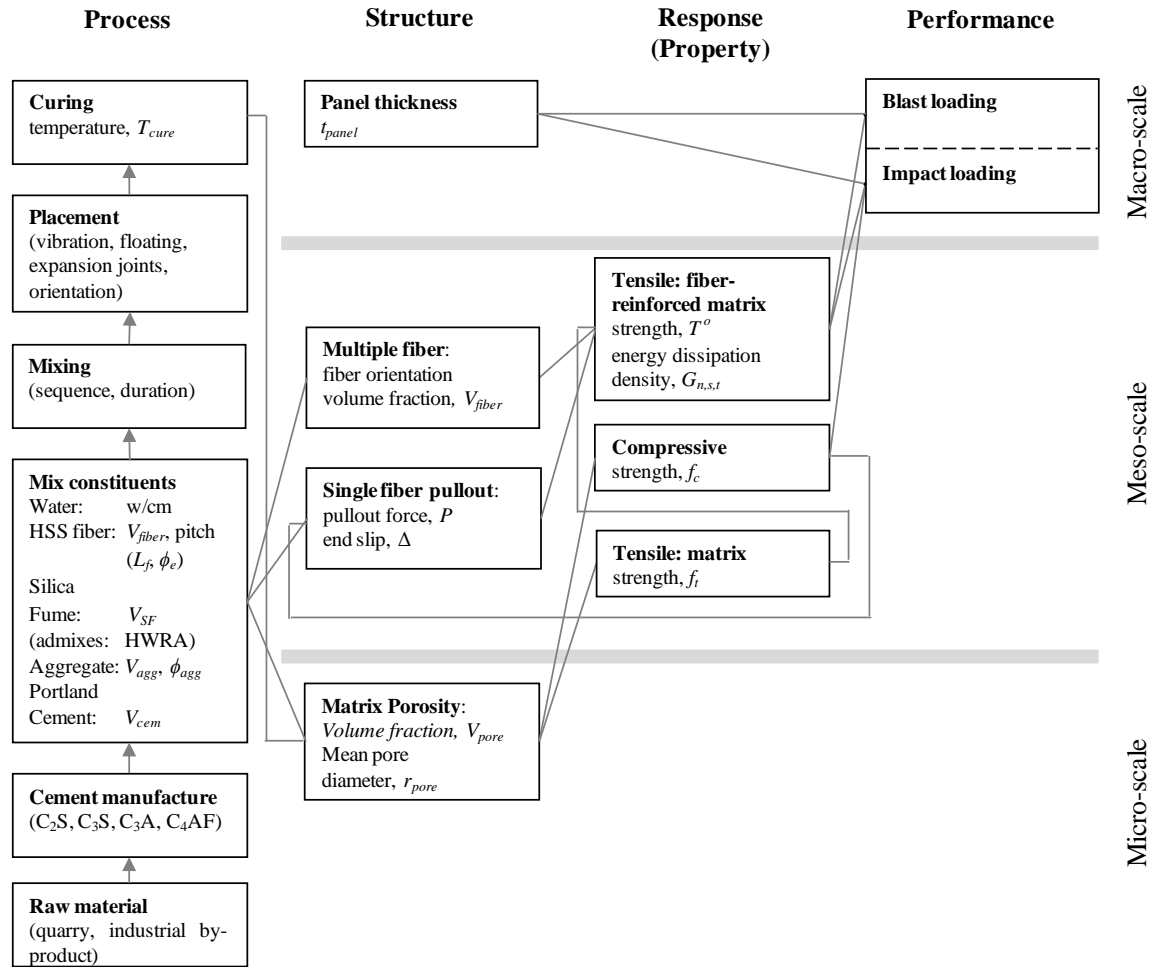
Figure 53. A set of process-structure-property-performance (PSPP) mappings for design of UHPC subject to blast and ballistic loading.

6.3   Process-structure relations

6.3.1 Mix Constituents and curing Temperature to Porosity (MCTP) model of hydrated UHPC

The relation between the mix constituents, curing temperature, and the porosity in the hardened cement paste depends on the constituent volume fractions, constituent sizes, hydration of the cement paste, interfacial transition zone, and the curing procedure. To account for these dependencies, the model assumes hydrated concrete consists of three phases: aggregate, bulk hardened cement paste (or bulk paste), and the Interfacial Transition Zone (ITZ). The first phase, aggregates, consists of coarse and fine aggregates that are assumed to be non-reactive during the hydration process. Aggregates are characterized by their shape, specific gravity, and their distribution of sizes. The volume fraction of aggregate, V_{agg}, is defined as volume of solids in the aggregate to the volume of UHPC. The remaining volume is assumed to consist of bulk paste and ITZ.

The second phase, bulk paste, consists of the products of hydration, water, and porosity. Within bulk paste, the porosity is delineated into gel and capillary porosity. Adopting the definition used by Klobes et al. (2008), gel porosity is defined as porosity with characteristic radii less than 25 nm, which represents the porosity within the Calcium-Silicate-Hydrate (CSH) gel. Capillary porosity is defined as porosity with characteristic radii between 25 nm and 25 μm, representing the porosity between CSH gel structures.

The third phase of material, the Interfacial Transition Zone (ITZ), is a relatively porous region between the aggregate and the bulk paste. Although relatively thin with a

typical thickness between 10 and 40 μm, ITZ can occupy up to 20 to 40% of the volume of the combined volume of bulk paste and ITZ in a normal strength concretes (Mindess et al., 2002). Similar to the bulk paste, the ITZ is delineated into gel and capillary porosity using the same definitions given above.

Figure 54 shows the set of process-structure relations used within the Mix Constituent and curing Temperature to Porosity (MCTP) model. Starting at the bottom of the process column, w/cm is the mass ratio of water to cementitious material, V_{cem} is the volume fraction of Portland cement, and V_{SF} is the volume fraction of silica fume. In the structure column, V_{agg}, V_{ITZ}, and V_{paste} are the volume fractions of aggregate, ITZ, and bulk paste. The total volume fraction of pores, V_{pore}, is delineated into gel porosity within the bulk paste, $V_{gel,paste}$, capillary porosity within the bulk paste, $V_{cap,paste}$, gel porosity within ITZ, $V_{gel,ITZ}$, and capillary porosity within the ITZ, $V_{cap,ITZ}$, each with their own respective characteristic radii, denoted by r with a matching subscript. The mean pore radius, r_{pore}, is a linear combination of the delineated pore radii and their respective volume fractions.

The components of the MCTP model are not new; the MCTP model is a new combination of previously documented models assembled in the following sequence. First, V_{ITZ} is calculated from V_{agg} and an assumed aggregate size distribution via the void exclusion probability model introduced by Lu and Torquato (1992) and later applied to cementitious microstructures by Garboczi and Bentz (1998). Next, the ratios of gel porosity to bulk paste and capillary porosity to bulk paste are calculated using w/cm and the desired hydration levels within the Powers hydration model (cf. Mindess et al., 2002).

The maximum porosity in the ITZ has been empirically determined to be two to three times that of the total porosity of the bulk paste (Ollivier, Maso, & Bourdette, 1995). The total porosity in the ITZ is determined by assuming an ITZ thickness of 20 μm, the maximum porosity in the ITZ is 2.5 times that of the total porosity in the paste, and that the maximum porosity in the ITZ cannot exceed 1. Then, the Powers hydration model is employed to calculate the gel porosity in the ITZ, which is then subtracted from the total ITZ porosity, thus allowing the capillary porosity in the ITZ to be calculated. Finally, the radii of gel pores are assumed to be constant; the radii of the capillary pores are assumed to be a function of packing density of silica fume, as calculated by the Linear Packing Model (Stovall, de Larrard, & Buil, 1986), and curing temperature.
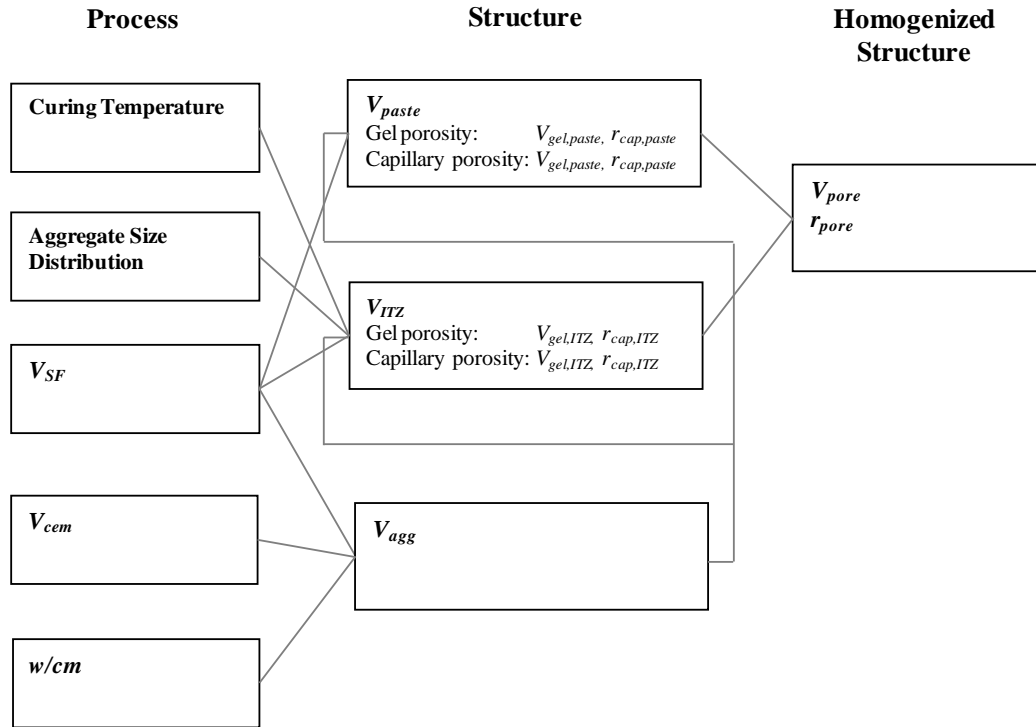
Figure 54. Process-structure (PS) relations used to determine volume fraction of porosity, V_{pore}, and the mean pore radius, r_{pore}.

The volume fraction of ITZ, V_{ITZ}, is predicted by the void exclusion probability model used by Garboczi and Bentz (1998), who assumed that hydrated concrete can be additively decomposed into aggregate, bulk paste, and ITZ. Thus, the volume fraction of ITZ is given by

$$V_{ITZ} = 1 - e_V\left(t_{ITZ}\right) - V_{agg} \,, \tag{27}$$

where t_{ITZ} is the thickness of the of ITZ surrounding the aggregates, V_{agg} is the volume fraction of aggregate, and $e_V\left(t_{ITZ}\right)$ is a function derived by Lu and Torquato (1992) describing the volume of the bulk paste surrounding a hard-particle and the hard particles' inter-penetrable shells. The function form of e_V is

$$e_V\left(t_{ITZ}\right) = \left(1 - V_{agg}\right)\exp\left[-\pi N\left(c\,t_{ITZ} + d\,t_{ITZ}^2 + g\,t_{ITZ}^3\right)\right], \tag{28}$$

where N is the total number of aggregates in a unit volume defined by

$N = \sum_{i=1}^{M}\dfrac{9V_{agg}V_{agg=i}}{4\pi\left(r_{i+1}^3 - r_i^3\right)}\ln\left(\dfrac{r_{i+1}}{r_i}\right)$, where M is the total number of bins (or sieves used in

aggregate sieve analysis) used in the aggregate size distribution, $V_{agg=i}$ is the volume fraction of aggregates in the ith bin, r_{i+1} is the largest radius particle in the bin, r_i is the smallest radius particle in the bin, and c, d, and g are functions defined by

$$c = \frac{4\langle R^2 \rangle}{1 - V_{agg}},$$

$$d = \frac{4\langle R \rangle}{1 - V_{agg}} + \frac{12\varepsilon_2 \langle R^2 \rangle}{\left(1 - V_{agg}\right)^2}, \text{ and} \qquad (29)$$

$$g = \frac{4}{3\left(1 - V_{agg}\right)} + \frac{8\varepsilon_2 \langle R \rangle}{\left(1 - V_{agg}\right)^2} + \frac{16A\varepsilon_2 \langle R^2 \rangle}{3\left(1 - V_{agg}\right)^3}.$$

In the preceding equation, ε_2 is defined as $\varepsilon_2 = 2\pi N \langle R^2 \rangle / 3$, A is a constant assumed to be equal to zero following the work of Garboczi and Bentz (1998), and $\langle R \rangle$ and $\langle R^2 \rangle$ are averages in terms of the number of aggregates of the assumed particle size defined as

$$\langle R^n \rangle = \sum_{i=1}^{M} \frac{9 V_{agg} V_{agg=i}}{4\pi N \left(r_{i+1}^3 - r_i^3\right)} \int_{r_i}^{r_{i+1}} r^{n-1} dr. \qquad (30)$$

The assumed thickness t_{ITZ} is guided by the computational results of Garboczi and Bentz (1991), who determined t_{ITZ} to be approximately equal to the diameter of monodisperse simulated cement grains within a two-dimensional simulation. Here, it is assumed $t_{ITZ} = 20$ μm, which is similar to the 15 μm median diameter of cement grains.

The porosity within the ITZ has been experimentally determined to increase from the far-field value of the bulk porosity at a distance t_{ITZ} from the surface of each aggregate to a maximum value at the surface of each aggregate (e.g. Gao et al., 2013). The maximum value of porosity has been experimentally measured to lie between 1.6 and 3.5 (Gao et al., 2013) for cement pastes without silica fume and was recommended to be within a range of 2 to 3 (Ollivier et al., 1995). In this work, it is assumed that the porosity within the ITZ linearly increases from a far-field value at a distance t_{ITZ} from the surface of each aggregate to a maximum value of 2.5 times the far-field porosity of

the bulk cement paste. Should the value 2.5 times the far-field porosity value exceed

unity, the maximum porosity value is set equal to unity.

6.3.2.2   Powers hydration model

After calculating V_{ITZ}, the volume fractions of past and ITZ are know. However,

the amount of porosity within each phase remains unknown. Here, the Powers hydration

model (cf. Mindess et al., 2002) is adopted to determine the amount of porosity present as

a function of the water to cementitious material ratio and the degree of hydration.

The Powers hydration model assumes that hydrating water is either evaporable or

non-evaporable. Evaporable water evaporates at a temperature of 105 ºC and resides

within either gel or capillary pores, which have characteristic radii on the order of 1-25

nm and 25-25,000 nm, respectively (Klobes et al., 2008). The mass of water in the gel

pores, in units of gram of water per gram of original cement, is given by

$$w_g = 0.18\alpha , \tag{31}$$

where α is the degree of hydration which monotonically increases from zero to a

maximum value of one, and 0.18 is a constant of proportionality empirically determined.

Non-evaporable water is chemically bound within Calcium-Silicate-Hydrate (CSH) and

may only be released by heating CSH to 1000 ºC (Mindess et al., 2002). The mass of

non-evaporable water, in units of gram of water per gram of original cement, is given by

$$w_n = 0.24\alpha , \tag{32}$$

where 0.24 is a constant of proportionality empirically determined to account for the stoichiometry of the chemical reaction. For complete hydration, i.e., $\alpha = 1$, the minimum ratio of the mass of water to the mass of original cement is given by

$$w_{\min} = w_g + w_n,\tag{33}$$

which can also be stated as the minimum water to cement ratio, $(w/c)_{\min} = 0.42$. For UHPCs, w/c ratios of between 0.20 and 0.30 are typical, leading to reduced maximum possible levels of hydration, α_{poss}, calculated by

$$\alpha_{poss} = \frac{w/c}{(w/c)_{\min}} = \frac{w/c}{0.42}.\tag{34}$$

During hydration, the Powers model separates the hydrated cement paste into four constituents: unhydrated cement, hydration products (i.e., cement gel), gel pores, and capillary pores. The volume of unhydrated cement, in terms of cm^3/g of original cement, is given by

$$V_u = (1-\alpha)\frac{1}{sg_{cem}},\tag{35}$$

where $sg_{cem} = 3.15$ is the specific gravity of cement. The volume of hydration products excluding gel pores, in cm^3 per g of original cement is given by

$$V_{hp} = 0.50\alpha.\tag{36}$$

The volume of gel pores, which are assumed to be saturated with water, is given by

$$V_g = 0.18\alpha,\tag{37}$$

and the volume of capillary pores is given by

$$V_c = w/c - 0.36\alpha.\tag{38}$$

The initial volume of cement paste is given by

$$V_p = w/c + \frac{1}{sg_{cem}} \,. \tag{39}$$

The volume fraction of capillary pores to cement paste is given by

$$P_{cap/paste} = \frac{w/c - 0.36\alpha}{w/c + \dfrac{1}{sg_{cem}}} \,, \tag{40}$$

and the volume fraction of gel pores to cement paste is given by

$$P_{gel/paste} = \frac{0.18\alpha}{w/c + \dfrac{1}{sg_{cem}}} \,. \tag{41}$$

6.3.2.3   *Packing density of silica fume prior to hydration*

It is known that the addition of silica fume reduces the porosity, specifically the porosity within the ITZ of hardened cement paste. One explanation is that silica fume, which has mean diameters between 0.1 and 0.3 μm, serves as a pozzolanic interstitial particle between cement particles with median particle diameters between 10 and 20 μm prior to hydration. To account for this effect, the MCTP model incorporates a particle packing to determine the ratio of the actual volume fraction of silica fume to the volume fraction of silica fume which provides the densest possible dry packing density.

There are a large number of packing models which have been classified by Kumar and Santhanam (2003) as discrete or continuous. Within discrete models, the models are further classified as binary (e.g. Furnas, 1931), ternary (e.g. Goltermann, Johansen, & Palbol, 1997), and multi-component (e.g. Fedors & Landel, 1979; Larrard, 1999; Stovall et al., 1986). Continuous models are strictly multi-component. Further classification is possible based the types of effects, i.e., wall effects, loosening effects, or compaction

effects, incorporated into the model. Wall effects are the changes to packing density caused by the interaction of relatively small particles with a much larger particle. Loosening effects are the changes to packing density due to a smaller particle not completely fitting within the vacancy caused by a larger particle. Compaction effects are the changes in packing density due to the compaction of particles. A comparison of packing models by Jones, Zheng, and Newlands (2002) found that the different models predicted packing densities for binary systems within 2.4 to 5.5 % of actual packing densities, deviated by up to 42% in the volume fraction of the small component to maximize the packing density, and that the major differences in the predicted packing density of the models arises when the ratio of small to large particle diameters is greater than 50%.

The design of UHPC materials utilizes the Linear Packing Model (LPM) introduced by Stovall, de Larrard, and Buil (1986). The LPM models an *n*-component system and accounts for the packing density of each component, ϕ_i, volume fraction of each component, V_i, wall and loosening effects, and the distribution of each component's size with a mean radius, r_i. The model assumes that the *n*-components are rank sorted by size such that $r_1 \geq ... \geq r_i \geq ... \geq r_n$. The packing density of the mix of components, ρ_{mix}, is the minimum of the *n* equations describing the packing density of the ith fully-packed system, i.e.,

$$\rho_i = \frac{\alpha_i}{1 - (1 - \alpha_i) \sum_{j=1}^{i-1} g(i,j) V_j - \sum_{j=i+1}^{n} f(i,j) V_j}.$$

(42)

In Eq. (42), α_i is the fully-packed packing density of the ith component (i.e., $\alpha_i = \phi_i$),

$g(i,j) = 1 - \dfrac{r_i}{r_j}$ adjusts for the wall effect of small particles encountering a particle of

much larger radius, and

$$f(i,j) = \begin{cases} 1 & r_j < \mu r_i \\ 1 - \dfrac{\alpha_i}{\alpha_T(r_i, r_j)}\left(1 - \dfrac{\mu r_i^3}{r_j^3}\right) & r_j \geq \mu r_i \end{cases} \tag{43}$$

adjusts for the loosening effect. In Eq. (43), μ is the ratio of the voids between larger

sized particles to the radius of the larger sized particles which is assumed to be 0.2, and

$\alpha_T = \dfrac{\alpha_i}{r_r}\left[(1-\mu^3)(1-\alpha) - 3\mu^3\right](r_i - r_j) + \alpha_i(1-\mu^3)$ is a functional relationship

determined by assuming that two components of the radius will have equivalent ϕ_{mix} for

$\eta_i = \eta_j = 0.5$. For r_j sufficiently small that that it does not displace the ith component,

$f(i,j)$ does not predict any loosening. However, the packing density of the mix is

reduced should the jth particle displace the ith particles due to the loosening effect.

Although it is possible to assign particle size distributions, Eq. (42) provides a

better estimation when the diameter of the smaller particle is at most 50% of the diameter

of the next larger particle. Therefore, this work will assume that distributions of coarse

and fine aggregates can be lumped into a mean value.

Validation of the packing model is shown in Figure 55, which shows a

comparison of the results of the packing model to results presented by Stovall, de

Larrard, and Buil (1986) for binary systems with r_1/r_2 ratios of 0.0143, 0.06, 0.089,

0.153, 0.290, and 0.29, and $\phi_1 = \phi_2 = 0.62$. In Figure 55, V_{small} is the volume fraction of

the smaller particle. The results presented by Stovall, de Larrard, and Buil deviate by a mean difference of 2% from the experimental data of McGeary (1961), who measured the packing density of steel spheres.
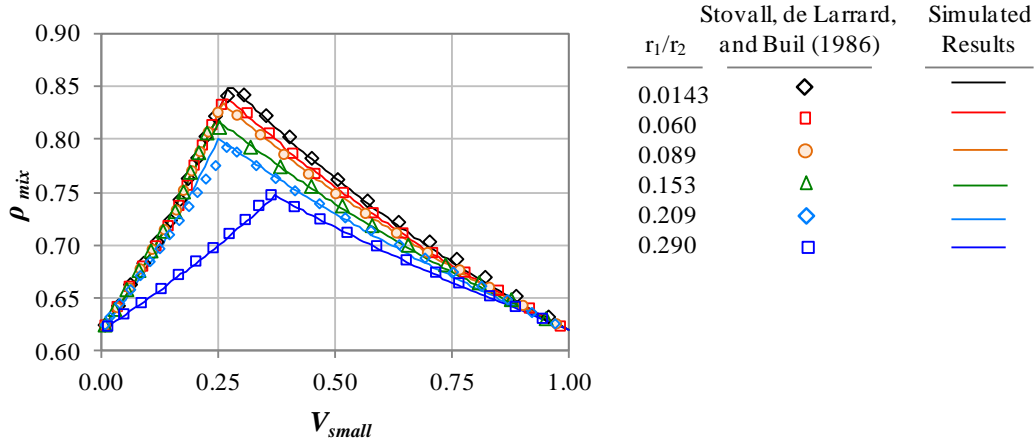
Figure 55. Comparison of simulated ρ_{mix} for a binary system of particles. Data points were reported by Stovall, de Larrard, and Buil (1986); data used to construct the solid lines were generated by the model described in Section 6.3.2.3.

The packing density of individual components, ϕ_i, depends on the arrangement and the shape of the particles. A hexagonal close packed arrangement of spheres has a packing factor of 0.74, whereas randomly placed spheres have a packing factor of approximately 0.64 (Cumberland & Crawford, 1987). For non-spherical particles, such as sand, the packing factor is approximately 0.56 (Stovall et al., 1986).

6.3.2.4   Validation of the combined packing and hydration model

The combined packing and hydration models are compared to Mercury Infusion Porosity (MIP) measurements of a NSC and HSC cured at room temperature and a UHPC cured at 250 ºC, as reported by Klobes et al. (2008). The data from Klobes et al. is

summarized in Table 11, in which CEM I 32.5 R, CEM I 42.5 R, and CEM I 52.5 R are

types of Portland cement specified by the European standard EN 197-1 to develop

minimum unconfined compressive strengths of 32.5, 42.5, and 52.5 MPa, respectively, at

28 days (Lyons, 2012). The 'R' designation indicates high early strength development

with minimum unconfined compressive strengths of 10, 20, and 30 MPa, respectively,

after 2 days.

Table 11. Cementitious constituents, composition (kg of constituent / m^3 of concrete), and Mercury Infusion Porosity (MIP) measurements reported by Klobes et al. (2008).

Concrete	Normal Strength Concrete (NSC)	High Strength Concrete (HSC)	Ultra-High Performance Concrete (UHPC)
Composition			
Cement type	CEM I 32.5 R	CEM I 42.5 R	CEM 52.5 R
Cement (kg/m^3)	310	500	500
Silica fume (kg/m^3)	-	50	116
Fly ash (kg/m^3)	-	-	123
Quartz filler (kg/m^3)	-	-	82
w/c	0.60	0.24	0.28
w/cm	0.60	0.22	0.23
Superplasticizer (%)	-	4.5	2.8
Aggregate (kg/m^3)	1827	1672	1340
Max size aggregate (mm)	32	16	2
Curing	6 days 20 ℃ underwater	6 days 20 ℃ underwater	3 days underwater, 2 days 250 ℃
Porosity			
Total porosity (%)	16.9	11.4	8.8
Gel porosity (%) ($2 \leq r \leq 25$ nm)	5.5	3.6	6.1
Capillary porosity (%) ($25 \leq r \leq 25,000$ nm)	11.2	7.6	2.6
Mean pore radius (nm)	54.1	29.8	3.0

Because silica fume is pozzolanic and undergoes a hydration reaction in the

presence of water, the listed w/c ratios of 0.60, 0.24, and 0.28 overestimate the true mass

ratio of water to reactive materials. Thus, it is appropriate to replace w/c with the mass

ratio of water to cementitious materials, w/cm, within the Powers model. Here, the mass

ratio of water to cementitious materials is defined as

$$w/cm = \frac{W}{C + k_1 SF + k_2 FA + ...},\qquad(44)$$

where W is the mass of water, C is the mass of cement, SF is the mass of silica fume,

k_1 is a pozzolanic efficiency factor for silica fume, FA is the mass of fly ash, k_2 is

pozzolanic efficiency factor of fly ash, and the ellipse represents other secondary

cementitious materials (Siddique, 2008). The determination of k_i values has been

framed in terms of an equivalent 28-day unconfined compressive strength for concretes

having the same workability and same mass of cement (e.g. Hassaballah & Wenzel,

1995), and in terms of mass of cement that could be replaced with the mass of secondary

cementitious material (Wong & Abdul Razak, 2005). A review of models and

experimental work of Wong and Abdul Razak (2005) indicates unique values of k_i are

elusive, even for a binary mixture of cement and one type of secondary cementitious

material. For this dissertation, it is assumed that the efficiency factors for silica fume and

fly ash are one and zero, respectively, which follows the convention of Klobes et al.

(2008). This definition yields a w/cm values of 0.60, 0.22, and 0.23 for the composition

shown in Table 13.

The remaining physical properties of the constituents were not listed by Klobes et

al. (2008), but are assumed to be in accordance with the physical properties reported by

Mindess, Young, and Darwin (2002) and Yazici et al. (2009) listed in Table 12. In Table

12, ϕ_i is the packing factor used within the Linear Packing Model with values given by

Stovall, de Larrard, and Buil (1986).

Table 12. Physical properties of Portland cement, pozzolans, and quartz powder.

Material	Mean size (*μm*)	shape	specific gravity	ϕ_i [3]
Portland cement [1]	10-15	angular, irregular	3.15	0.56
fly ash [1]	10-15	most spherical	2.3	0.56
Silica fume [1]	0.1-0.3	spherical	2.2	0.64
quartz powder [2]	100-400	angular	2.7	0.56

[1] Mindess, Young, and Darwin (2002)
[2] Yazici et al. (2009)
[3] Stovall, de Larrard, and Buil (1986)

The coarse and fine aggregates are assumed to following the gradation data given in Table 13, which were constructed using the ASTM's Standard Specification for Concrete Aggregates (2008b) and the maximum size aggregate given in Table 11. Furthermore, it was assumed that the volume of coarse aggregates is 1.5 times the volume of the fine aggregates in accordance with Garboczi and Bentz (1998). The assumed specific gravity and packing factors for both coarse and fine aggregates is 2.7 and 0.56. For reference, the fineness modulus of the assumed fine aggregate in the NSC and HSC is 3.15; the fineness modulus (cf. Mindess et al., 2002)of the assumed fine aggregate in the UHPC is 3.25.

Table 13. Assumed gradation of coarse and fine aggregates.

Concrete		Normal Strength Concrete (NSC)	High Strength Concrete (HSC)	Ultra-High Performance Concrete (UHPC)
Sieve Parameters		Volume fraction contained within each sieve		
D_{min} (mm)	D_{max} (mm)			
0.075	0.15	0.04	0.04	0.11
0.15	0.30	0.08	0.08	0.18
0.30	0.60	0.12	0.12	0.24
0.60	1.18	0.10	0.10	0.29
1.18	2.36	0.06	0.11	0.18
2.36	4.75	0.00	0.10	0.00
4.75	9.5	0.05	0.30	0.00
9.5	12.5	0.10	0.10	0.00
12.5	19.5	0.30	0.05	0.00
19.5	25.0	0.10	0.00	0.00
25.0	37.5	0.05	0.00	0.00

To demonstrate the MCTP model, an example calculation of the V_{pore} and r_{pore} is given for the NSC material reported by Klobes et al. (2008). First, the volume fraction of aggregate is calculated as

$$V_{agg} = \frac{m_{agg}}{\rho_{agg}} = \frac{1827 \frac{\text{kg aggregate}}{\text{m}^3 \text{ concrete}}}{2700 \frac{\text{kg aggregate}}{\text{m}^3 \text{ aggregate}}} = 0.677 \frac{\text{m}^3 \text{ aggregate}}{\text{m}^3 \text{ concrete}}, \tag{45}$$

Using $V_{agg} = 0.677$, $t_{ITZ} = 20$ μm, and the Normal Strength Concrete aggregate gradation given in Table 13, the void exclusion probability model calculates $\langle R \rangle = 7.21 \times 10^{-5}$, $\langle R^2 \rangle = 7.66 \times 10 - 9$, $c = 9.48 \times 10^{-8}$, $\varepsilon_2 = 740$, $d = 0.0015$, $g = 8.21$, and

$V_{ITZ} = 0.101 \frac{\text{m}^3 \text{ ITZ}}{\text{m}^3 \text{ concrete}}$. The volume fraction of the bulk paste, V_{paste}, here defined to be not within a distance t_{ITZ} of any aggregate surface is

$$V_{paste} = 1 - V_{agg} - V_{ITZ} = 0.222 \frac{\text{m}^3 \text{ paste}}{\text{m}^3 \text{ concrete}}. \tag{46}$$

The porosity within the paste, also referred to as the far-field porosity in Section 6.3.2.1, is calculated using the Powers hydration model. Using $w/cm = 0.6$, the Powers hydration model predicts the hydration is complete, i.e., $\alpha = 1$, $P_{cap/paste} = 0.262$, and $P_{gel/paste} = 0.196$. The volume fractions of capillary pores in the paste and of gel pores in the paste are calculated as

$$
\begin{aligned}
V_{cap,paste} &= P_{cap/paste}V_{paste} = (0.262)(0.222) = 0.058, \text{ and} \\
V_{gel,paste} &= P_{gel/paste}V_{paste} = (0.196)(0.222) = 0.044.
\end{aligned}
\tag{47}
$$

The maximum porosity in the ITZ, $P_{\max}$, is equal to the minimum of either one or 2.5 times the porosity in the paste, i.e., $2.5 \times (0.262 + 0.196) = 1.15$. In this case, the maximum porosity in the ITZ is set equal to one. The volume of porosity in the ITZ divided by the volume of the ITZ, P_{ITZ}, is calculated assuming a linear distribution of porosity throughout the ITZ, i.e., $P_{ITZ} = \frac{1}{2}\left(P_{\max} + \left(P_{gel/paste} + P_{cap/paste}\right)\right) = 0.729$. The volume fraction of the gel pores in the ITZ are calculated as

$$
V_{gel,ITZ} = P_{gel/paste}V_{ITZ} = (0.196)(0.101) = 0.020.
\tag{48}
$$

The volume fraction of capillary porosity in the ITZ are calculated as

$$
V_{cap,ITZ} = \left(P_{ITZ} - P_{gel/paste}\right)V_{ITZ} = (0.729 - 0.196)(0.101) = 0.053.
\tag{49}
$$

Results of the MCTP model and experimental results reported by Klobes et al. (2008) are compared in Table 14.

Table 14. Comparison of porosity volume fractions from MCTP model and MIP experimental data of Klobes et al. (2008).

Concrete	Normal Strength Concrete (NSC)		High Strength Concrete (HSC)		Ultra-High Performance Concrete (UHPC)	
	MCTP model	Klobes et al. (2008)	MCTP model	Klobes et al. (2008)	MCTP model	Klobes et al. (2008)
Parameter						
V_{agg}	0.677	0.677	0.619	0.619	0.527	0.527
V_{ITZ}	0.101		0.101		0.187	
$V_{gel,ITZ}$	0.020		0.018		0.034	
$V_{cap,ITZ}$	0.053		0.024		0.045	
α_{actual}	1.00		0.524		0.548	
V_{paste}	0.222		0.280		0.287	
$V_{gel,paste}$	0.044		0.049		0.085	
$V_{cap,paste}$	0.058		0.016		0.062	
Results						
V_{pores}	**0.175**	**0.169**	**0.107**	**0.114**	**0.147**	**0.088**
$V_{gel,pores}$	0.064	0.055	0.067	0.036	0.085	0.061
$V_{cap,pores}$	0.111	0.112	0.040	0.076	0.028	0.026

For the NSC and HSC samples, V_{pore} predicted by the MCTP model and measured by Klobes et al. (2008) agree within 7%. For the NSC sample, the partitioning of the gel and capillary porosity is qualitatively correct, with the majority of the porosity classified as capillary porosity. However, the partitioning of porosity within the HSC sample is qualitatively incorrect: the MCTP model predicts a majority of porosity within the gel pores, whereas measurements indicate the opposite. One possible explanation for the discrepancy is the assumed 25 nm demarcation radius between gel and capillary porosity. The experimental data of Klobes et al. (2008) indicate a pronounced peak in

porosity at a pore radius of 25 nm; thus, small measurement errors or ink bottle effects could alter the partitioning of porosity.

For the UHPC, the MCTP model predicts $V_{pore} = 0.147$, and the experiments indicated $V_{pore} = 0.088$. Here, the difference is attributed to the assumed thickness of ITZ and thermal curing, which has been observed by other researchers to reduce the porosity in the ITZ and the porosity throughout the bulk cement paste. For example, Scheydt and Müller (2012) show SEM images indicating the presence of a 2- to 4-μm-thick ITZ surrounding steel fibers within a UHPC cured at 20 ℃ for 28 days; however, a UHPC made from the same composition and cured for 3 days at 90 ℃ shows the complete absence of an ITZ. Accordingly, V_{pore} decreased by 39% from 0.089 to 0.054, which cannot be fully explained by changing the microstructure of the ITZ to match the bulk paste. Similarly, Cheyrezy, Maret, and Frouin (1995) observed an 82% decrease in V_{pore} from 0.085 to 0.015 for a non-fiber-reinforced UHPC cured at 20 and 90 ℃, respectively. For curing temperatures greater than 90 ℃, Cheyrezy, Maret, and Frouin (1995) found V_{pore} decreased by a maximum of 87% at a curing temperature of 150 ℃. Above 150 ℃, V_{pore} increased such that V_{pore} at a 250 ℃ curing temperature was slightly greater than V_{pore} at a 90 ℃ curing temperature. The decrease in V_{pore} reported by Scheydt and Müller (2012) and Cheyrezy, Maret, and Frouin (1995) is congruent with autogenous shrinkage and the increase of capillary stresses caused self-desiccation (Mindess et al., 2002). Here, a conservative estimate is applied such that V_{pore} decreases by 25% for curing temperatures at and above 90 ℃.

Table 15. Comparison of porosity volume fractions for UHPC using MCTP model and MIP experimental data of Klobes et al. (2008).

Concrete	Ultra-High Performance Concrete (UHPC)		Ultra-High Performance Concrete (UHPC): no ITZ, 25% capillary porosity reduction from heating	
	model	exp.	model	exp.
Parameter				
V_{agg}	0.527	0.527	0.527	0.527
V_{ITZ}	0.187		-	
$V_{gel,ITZ}$	0.034		-	
$V_{cap,ITZ}$	0.045		-	
α_{actual}	0.548		0.548	
V_{paste}	0.287		0.473	
$V_{gel,paste}$	0.085		0.064	
$V_{cap,paste}$	0.062		0.028	
Results				
V_{pores}	**0.147**	**0.088**	**0.085**	**0.088**
$V_{gel,pores}$	0.085	0.061	0.064	0.061
$V_{cap,pores}$	0.028	0.026	0.021	0.026

The MCTP model has been shown to estimate the total porosity to within 7% of three experimental measurements reported by Klobes et al. (2008); however, the mean pore size as a function of mix constituents and process remains to be determined. As a first estimate, it is assumed that the average pore radius can be calculated as a volume weighted mean of the diameters of the four types of porosity, i.e.,

$$r_{pore} = \frac{r_{gel,paste}V_{gel,paste} + r_{cap,paste}V_{cap,paste} + r_{gel,ITZ}V_{gel,ITZ} + r_{cap,ITZ}V_{cap,ITZ}}{V_{gel,paste} + V_{cap,paste} + V_{gel,ITZ} + V_{gel,ITZ}}, \qquad (50)$$

where $r_{gel,paste}$, $r_{cap,paste}$, $r_{gel,ITZ}$, and $r_{cap,ITZ}$ are assumed radii of the four of the four types of pores. Both of the gel radii, i.e., $r_{gel,paste}$ and $r_{gel,ITZ}$, are assumed to be equal to 2 nm. The silica fume, which increases self-desiccation, and the effect of curing temperature are

assumed to reduce the pore radii of the capillary porosity, not the gel porosity. Therefore, the relevant task is to determine $r_{cap,paste}$ and $r_{cap,ITZ}$ as functions of quantity of silica fume and curing temperature. Here, an empirical relation is used to fit the data of Klobes et al. (2008) to the assumed forms

$$r_{cap,ITZ} = c_0 + c_1 \frac{V_{SF}}{V_{SF,\max}} + c_2 \left(T_{cure} - 20\right), \text{ and}$$

$$r_{cap,paste} = c_3 + c_4 \frac{V_{SF}}{V_{SF,\max}}, \tag{51}$$

where V_{SF} is the volume fraction of silica fume, $V_{SF,\max}$ is the volume fraction of silica fume in a packing configuration in which the silica fume is fully packed thus filling all the vacancies between cement grains, and T_{cure} is the curing temperature specified in °C. There is no assumed dependence of temperature on $r_{cap,ITZ}$ because it is assumed that ITZ is absent after a UHPC is thermally cured. After fitting the constants to data in Klobes et al. (2008), Eq. (51) is rewritten as

$$r_{cap,ITZ} = 130 - 45 \frac{V_{SF}}{V_{SF,\max}} - 0.45 \left(T_{cure} - 20\right), \text{ and}$$

$$r_{cap,paste} = 35 - 60 \frac{V_{SF}}{V_{SF,\max}}. \tag{52}$$

Combining Eqs. (50) and (52) with data in Table 14, the MCTP model can be used to predict the average pore radii, r_{pore}. Figure 56 shows the MCTP model's estimate of r_{pore} as a function of the measured r_{pore}. The solid black line represents a one-to-one correlation, and the two dashed gray lines represent ±10% deviation from a one-to-one correlation.
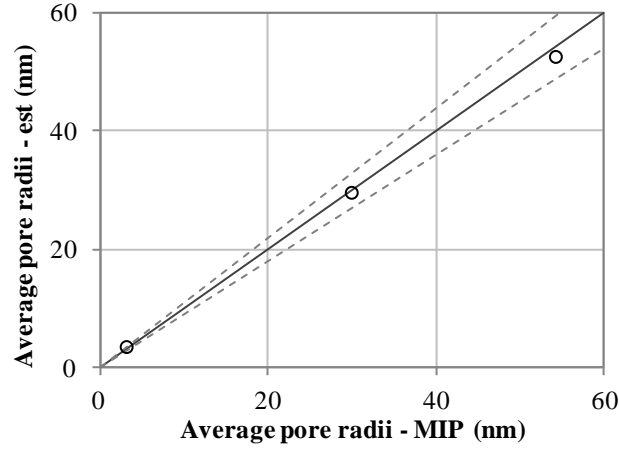
Figure 56. Comparison of average pore radii, r_{pore}, measured experimentally by Klobes et al. (2008) and estimated via MCTP model. The solid black line represents a one-to-one relation and the dashed gray lines above and below the black line represent errors of $\pm\ 10\%$.

6.3.2.4 Response surfaces

The previously described model is used to create response surfaces to be used within IDEM. For the response surface, it is assumed that all gradations of coarse and fine aggregates follows the gradation listed for in Table 16, which is identical to the gradation of coarse and fine aggregates for UHPC listed in Table 13. This gradation represents a mixture of a sand and quartz powder with a maximum aggregate size of 2 mm. The volume fractions listed in Table 16 sum to unity, and thus represent the volume fraction of a size of aggregate within all of the aggregate, not the volume fraction of a size of aggregate within the UHPC. The volume fraction of aggregate to the total volume is given by

$$V_{agg} = 1 - V_{cem} - V_{SF} - w/cm \left(V_{cem}\rho_{cem} + V_{SF}\rho_{SF} \right) / \rho_{water}. \tag{53}$$

Table 16. Assumed gradation of aggregates.

| Sieve Parameters | | Volume fraction |
D_{min} (mm)	D_{max} (mm)	contained within each sieve
0.075	0.15	0.11
0.15	0.30	0.18
0.30	0.60	0.24
0.60	1.18	0.29
1.18	2.36	0.18
2.36	4.75	0.00
4.75	9.5	0.00
9.5	12.5	0.00
12.5	19.5	0.00
19.5	25.0	0.00
25.0	37.5	0.00

The MCTP model simulated 200 different combinations of parameters encompassing a space of T_{cure} (20 and 90 °C), V_{cem} (0.1 to 0.24), V_{SF} (0.02 to 0.05), and w/cm (0.22 to 0.30). Results of the 200 different simulations were then fit to a regression model to generate a functional forms

$$
\begin{aligned}
V_{pore}\left(w/cm, V_{cem}, V_{SF}\right) = & -0.0398 - 0.000167 T_{cure} + 0.201 V_{cem} + 0.193 V_{SF} + 0.298\, w/cm \\
& -0.00761 T_{cure} V_{cem} - 0.000735 T_{cure} V_{SF} - 0.00198 T_{cure}\, w/cm \\
& -0.315 V_{cem}^{2} - 0.558 V_{cem} V_{SF} + 1.37 V_{cem}\, w/cm - 0.165\, w/cm^{2},
\end{aligned}
\tag{54}
$$

and

$$
\begin{aligned}
r_{pore}\left(w/cm, V_{cem}, V_{SF}\right) = & \; 70.9 - 0.76 T_{cure} - 71.5 V_{cem} - 91.1 V_{sf} - 16.8\, w/cm \\
& + 1.10 T_{cure} V_{cem} + 1.33 T_{cure} V_{SF} + 0.307 T_{cure}\, w/cm - 31.9 V_{cem}^{2} \\
& - 309 V_{cem} V_{SF} - 65.2 V_{cem}\, w/cm - 64.5 V_{SF}^{2} - 78.3 V_{SF}\, w/cm.
\end{aligned}
\tag{55}
$$

Figure 57 compares V_{pore} as predicted by the regression model in Eq. (54) and the prediction of V_{pore} by the MCTP model. The regression model predicts the result of the MCTP model within 10% except for $V_{pore} < 0.04$.
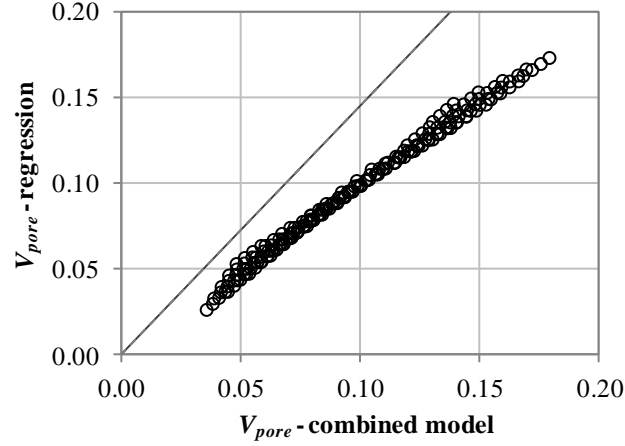
Figure 57. Comparison of V_{pore} predicted by regression model (i.e., Eq. (54)) and V_{pore} predicted by the MCTP model. The solid black line represents a one-to-one relation and the dashed gray lines above and below the black line represent errors of $\pm\,10\%$.

Figure 58 compares r_{pore} as predicted by the regression model in Eq. (55) and the prediction of r_{pore} by the MCTP model. The regression model predicts the result of the MCTP model within 15% except for $r_{pore} \leq 3$. In Figure 58, there is a large gap in data for r_{pore} values between 10 and 33 nm. This gap is due to the substantial decrease in r_{pore} caused by curing at 90 ℃.
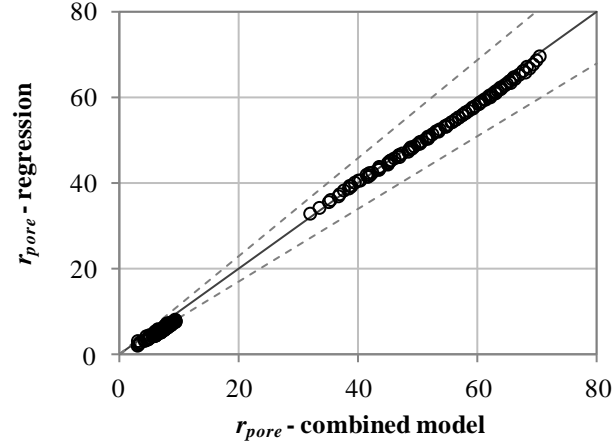
Figure 58. Comparison of r_{pore} predicted by regression model (i.e., Eq. (55)) and r_{pore} predicted by the MCTP model. The solid black line represents a one-to-one relation and the dashed gray lines above and below the black line represent errors of $\pm$ 15%.

6.3.2 Mix constituents to single fiber

The mix constituents to single fiber relation is defined by the three-dimensional numerical model at the single fiber length scale, as described in Section 3.2 of this dissertation.

6.3.3 Mix constituents to multiple fibers

The mix constituents to multiple fiber relation assumes that the volume fraction of fibers within the mix constituents are randomly placed and oriented within the UHPC microstructure. Furthermore, it is assumed that the fibers do not undergo mechanical deformation during the mixing process; therefore, the fiber length, diameter, morphology, and initial curvature remain the same during mixing. Possible clumping, introduction of porosity due to clumping, and fiber orientation from wall effects are not considered. The

169

fiber aspect ratio, λ, is fixed at 50 and the ultimate tensile strength of the fiber is assumed to be 2,400 MPa.

6.4   Structure-responses relations

6.4.1   Relation between single fiber pullout, Multiple fibers, tensile strength of the matrix, and the tensile response of a fiber-reinforced matrix

The relation between the single fiber pullout, multiple fibers, tensile strength of the matrix, and tensile responses of the fiber-reinforced matrix are defined by the model at the multiple-fiber length scale (cf. Chapter 3). In particular, the model utilizes the uniaxial tensile strength of the matrix, f_t, and the pullout force versus end slip relations to compute the quasi-static tensile strength and the dissipated energy density of the composite. Pullout force versus end slip relations for straight, smooth fibers were simulated via the analytical model developed by Gopalratnam and Shuh (1987). Pullout force versus end slip relations for fiber containing morphology, i.e., polygonal cross sections twisted along the fiber length, were generated by the model at the single fiber length scale with the pullout force set to zero for the final 20% of $L_{fiber}/2$, in accordance with experimental data presented by Sujivorakul (2002).

The pullout force versus end slip behavior for each fiber is used as the scale transition mechanism to the multiple fiber length scale. The multiple fiber length scale introduces fiber volume fraction and fiber inclination angle (cf. Li et al., 1990) to predict the quasi-static tensile strength and the dissipated energy density, which together define the tensile response. Figure 59 shows the maximum tensile strength of the fiber

reinforced matrix as a function of fiber volume fraction, fiber pitch, and non-reinforced matrix tensile strength. At $V_{fiber} = 0.5\%$, the maximum tensile strength of the fiber reinforced composite is dominated by increases in the matrix tensile strength, as indicated by the vertically-delineated iso-levels in Figure 59a. However, for $V_{fiber} = 2\%$ the maximum pullout force of fibers of different pitch dominates the maximum tensile strength response as indicated by horizontal iso-levels in Figure 59d.
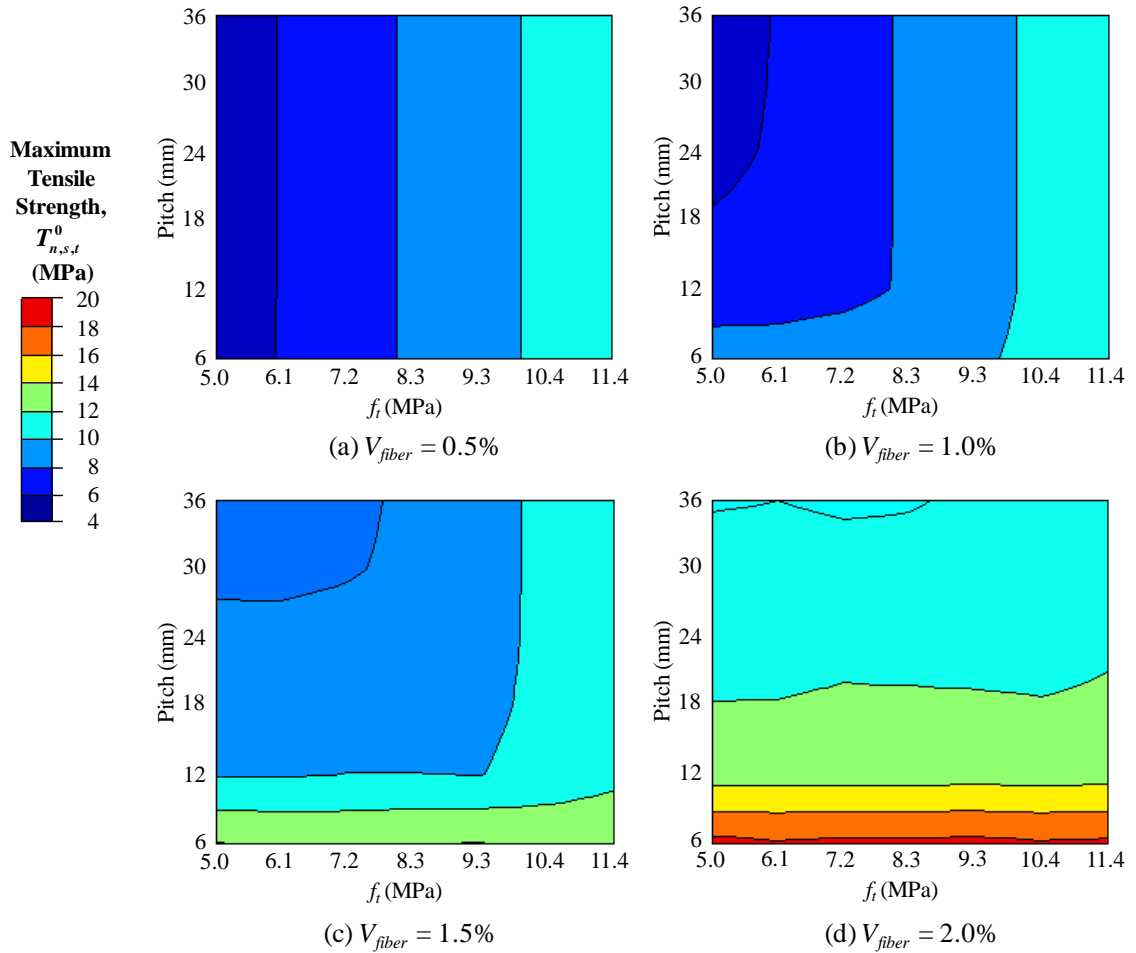
Figure 59. Maximum tensile strength as a function of fiber volume fractions between 0.5 and 2%, fiber pitch, and non-reinforced matrix tensile strength. All fibers had a 0.5-mm equivalent diameter and 25-mm length.

The 168 data points used to generate the contour plots in Figure 59 were fit to a rule of mixtures form, i.e.,

$$T^o = 0.85\left(1-V_{fiber}\right)f_t + 1300\left\langle V_{fiber} - 0.0075\right\rangle pitch^{-0.3}, \qquad (56)$$

where $\langle\ \rangle$ are McCauley brackets signifying $\langle x\rangle = \frac{1}{2}\left(x+|x|\right)$, and 0.85, 1300, -0.0075, and -0.3 are fitting parameters. The correlation between the data calculated by the multi fiber length scale and the regression are shown in Figure 60. The solid black represents the regression shown in Eq. (56), and the dashed gray lines above and below the black line represent errors of ± 20%.
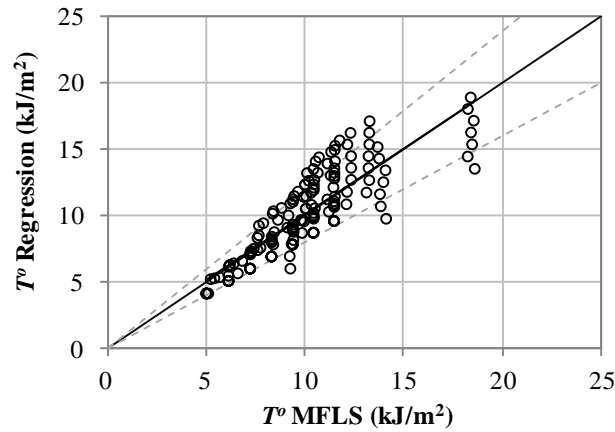
Figure 60. Comparison of T^0 as calculated by the model at the multiple fiber length scale (MFLS) and regression. The solid black line represents a one-to-one relation and the dashed gray lines above and below the black line represent errors of ± 20%.

Figure 61 shows the dissipated energy density as a function of fiber volume fractions between 0.5% and 2%, fiber pitch between 6 and 36 mm, and the non-reinforced matrix tensile strength between 5 and 11.4 MPa. The brittle nature of the matrix causes the dissipated energy density to be highly dependent upon the fiber volume

fraction and pitch of the fiber. In Figure 61, this behavior can be observed by the

horizontal iso-levels of dissipated energy density, which increase with increasing fiber

volume fraction. For comparison, the dissipated energy density for a fiber reinforced

matrix having 200-MPa unconfined compressive strength and $V_{fiber} = 2\%$ of 0.185-mm

diameter by 14-m long straight smooth fibers is 13.5 kJ/m^2, which is approximately one-

third that of a similar matrix with triangular cross section fibers with a 36-mm pitch.
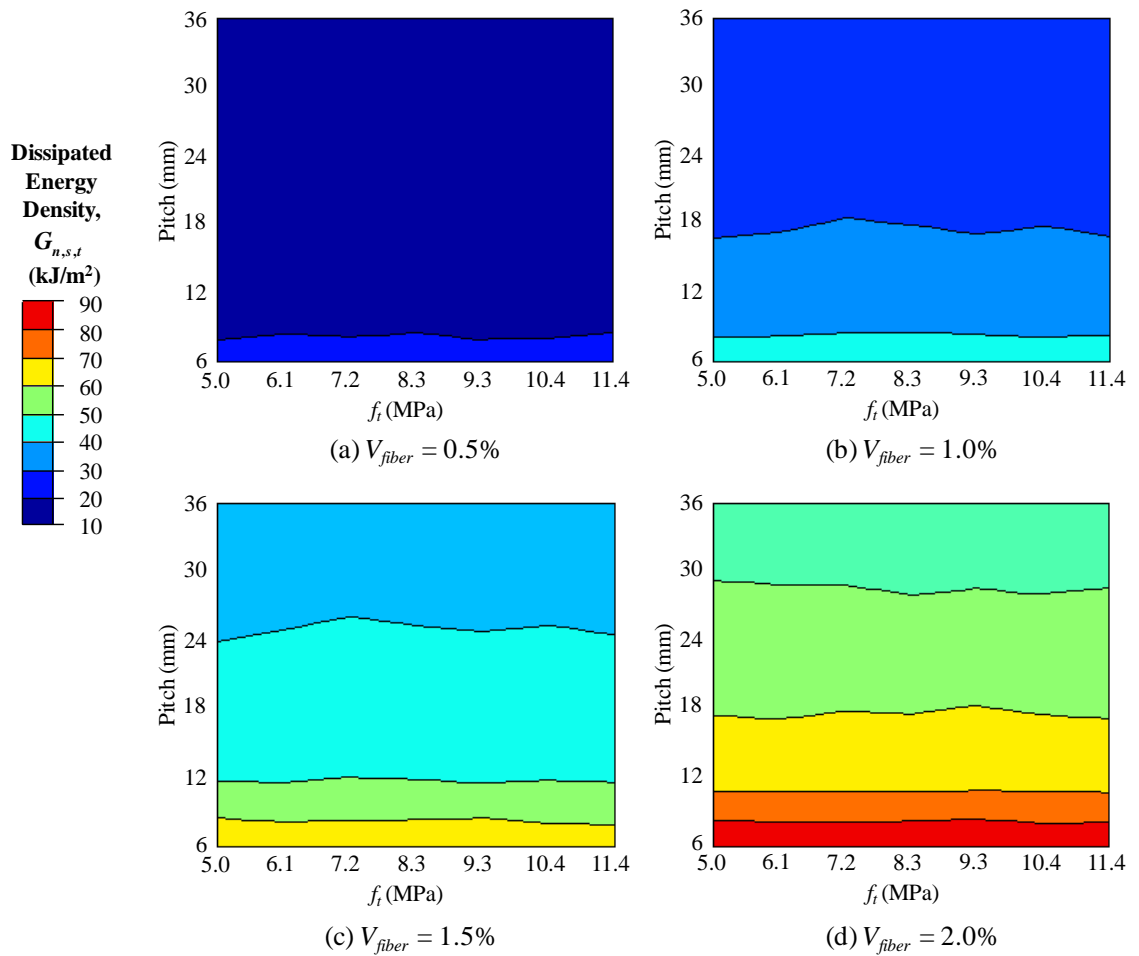
Figure 61. Dissipated energy densities as functions of fiber volume fractions between 0.5 and 2%, fiber pitch, and non-reinforced matrix tensile strengths. All fibers had a 0.5-mm equivalent diameter and 25-mm length.

The 168 data points used to generate the contour plots shown in Figure 61 were fit to the non-linear regression

$$E_{dis} = 0.166 + 4320V_{fiber} - 62.4V_{fiber}\ pitch,\qquad(57)$$

where V_{fiber} is specified in decimal form, i.e., $0.005 \leq V_{fiber} \leq 0.02$, and $pitch$ is specified in mm. Figure 62 compares E_{dis} as calculated by the model at the multiple fiber length scale (MFLS) to E_{dis} as calculated by the linear regression in Eq. (57). The solid black line represents a one-to-one correlation, and the dashed gray lines above and below the black line represent errors of $\pm$ 10%.
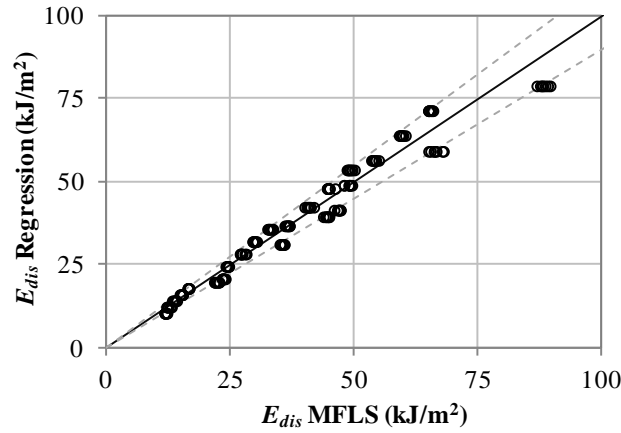
Figure 62. Comparison of E_{dis} as calculated by the model at the multiple fiber length scale and the fitting linear regression. The solid black line represents a one-to-one relation and the dashed gray lines above and below the black line represent errors of $\pm$ 10%.

6.4.2 *Relation between porosity and compressive strength*

The relation between porosity and compressive strength has been studied extensively. Powers (1958) measured the volume fraction of porosity, V_{pore}, and the

unconfined compressive strength, f_c, of cement pastes over the range $27 \le f_c \le 117$

MPa. The data were used to determine the empirical relation $f_c = 234(1 - V_{pore})^3$, where

234 is a constant representing the intrinsic strength of porosity-free cement paste. Later,

Odler and Rößler (1985) measured the distribution of pore radii within cement pastes

over the range $4 \le f_c \le 112$ MPa that had been cured at temperatures between 25 and

100ºC. They fit their experimental data to the linear relation

$$f_c = c_0 + c_1 V_{pore<10} + c_2 V_{10<pore<100} + c_3 V_{pore>100}, \tag{58}$$

where c_0, c_1, c_2, and c_3 are empirically determined parameters, and $V_{pore<10}$, $V_{10<pore<100}$,

and $V_{pore>100}$ are the volume fractions of porosity for pores with mean pore radii, r_{pore},

less than 10 nm, between 10 and 100 nm, and greater than 100 nm, respectively.

The analytical model chosen for the relation between porosity and compressive

strength is derived from Kumar and Bhattacharjee (2003), who developed a functional

form of f_c based on Griffith model of fracture (Griffith, 1921). The function form starts

with the tensile stress require for fracture of a brittle material, i.e.,

$$f_t = \sqrt{\frac{2ET}{\pi a}}, \tag{59}$$

where E is the effective modulus of elasticity for the porous material, T is the effective

fracture surface energy for the porous material, and a is the half-crack length. Two

assumptions are required to incorporate porosity. First, it is assumed that the effective

modulus is $E = E_0(1 - V_{pore})$, where E_0 is the modulus of elasticity for the material

without porosity. Second, it is assumed that $T = T_0(1 - V_{pore})$, where T_0 is the fracture

surface energy for the material without porosity. The effects of hydration in Kumar and

Bhattacharjee's model are accounted for by introducing the mass fraction of cementitious materials, M_c, such that Equation (59) is expressed as

$$f_t = k_1 M_c \frac{\left(1 - V_{pore}\right)}{\sqrt{r_{pore}}},$$ (60)

where k_1 is a constant depending upon E_0 and T_0. Finally, the unconfined compressive strength is assumed to proportional to f_t, resulting in

$$f_c = k_2 M_c \frac{\left(1 - V_{pore}\right)}{\sqrt{r_{pore}}},$$ (61)

where k_2 is a different material constant. The model was used by Kumar and Bhattacharjee (2003) to fit experimental data with $13.6 \leq f_c \leq 43.2$ MPa and $0.38 \leq w/cm \leq 0.65$. Here, the model is adapted for matrices with lower w/cm and greater compressive strengths by replacing M_c with $\dfrac{1}{w/cm}$, resulting in

$$f_c = K \frac{\left(1 - V_{pore}\right)}{w/cm \sqrt{r_{pore}}}.$$ (62)

The material constant K is determined by fitting experimental data of Kumar and Bhattacharjee (2003) and Klobes, Rübner, Hempel, and Prinz (2008). Figure 63a shows the fit of the linear regression determining $K = 99.3$ MPa$\sqrt{nm}$, thus resulting in the nominal relation

$$f_c = 99.3 \frac{1 - V_{pore}}{w/cm \sqrt{r_{pore}}}.$$ (63)

Figure 63b compares f_c as measured to the prediction of the model. The solid black line has a slope of one, the two gray lines have slopes $\pm 10\%$ from unity.
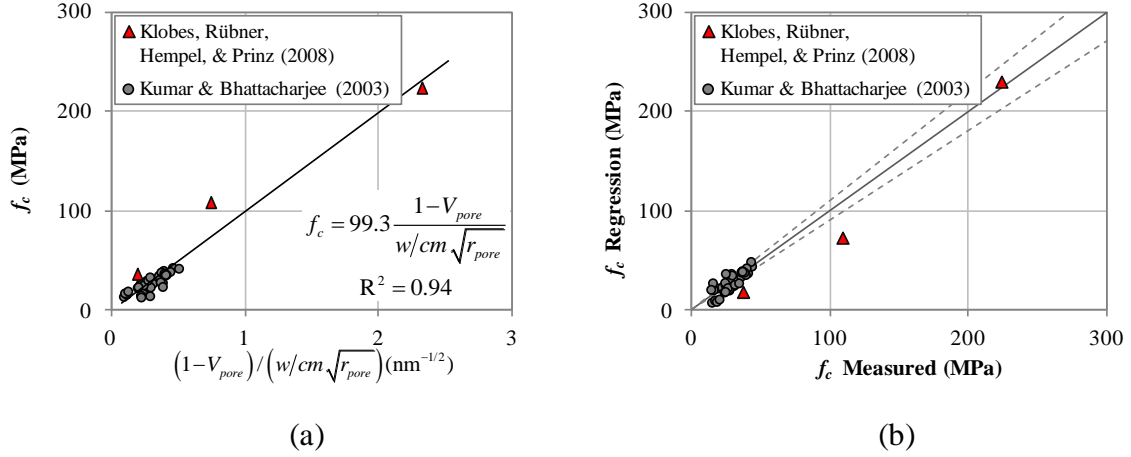
Figure 63. (a) Fitting of material constant K for the compressive strength as a function of the volume fraction of pores, V_{pore}, mean pore radius, r_{pore}, and mass ratio of water to cementitious materials, w/cm. (b) Comparison of f_c as calculated by Equation (63) to f_c as experimentally measured. The solid black line represents a one-to-one relation and the dashed gray lines represent errors of $\pm 10\%$.

6.4.3 Relation between porosity and tensile response

The tensile response of UHPCs may be measured via flexural tests (ASTM 1609; 2012b), split cylinder (ASTM C496; 2004), or direct tension tests. Due to the difficulty and recent emergence of the direct tensile tests, there is a paucity of data in literature regarding direct tensile tests, porosity, and pore size distribution. Therefore, an intermediate relation between tensile strength and compressive strength will be used to determine a relation between tensile strength and porosity.

The relation between tensile strength and compressive strength has typically been expressed as a power law relation, i.e., $f_t = c_0 \left(f_c \right)^n$, where c_0 and n are material parameters to be determined from experiments, from which n is typically in the range between 0.5 and 0.75 for concretes with f_c between 7 and 69 MPa (Oluokun, 1991).

177

Data from Garas-Yanni (2009), Pul (2008), and Zheng, Kwan, and Lee (2001) shown in Figure 64 was used for calibration. In Figure 64, the black line represents the nominal relation between f_t and f_c, i.e.,

$$f_t = 0.177\left(f_c\right)^{0.74}.$$ (64)

The gray lines below and above the nominal relation represent the lower and upper functions, i.e.,

$$f_{t,lower} = 0.144\left(f_c\right)^{0.74}, \text{ and}$$
$$f_{t,upper} = 0.216\left(f_c\right)^{0.74}.$$ (65)
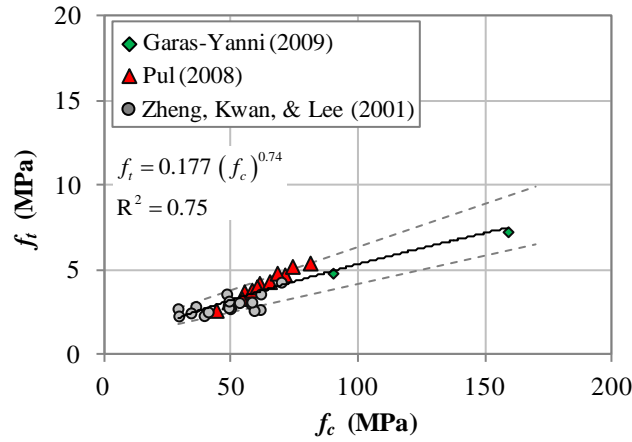
Figure 64. Relation between uniaxial tensile strength, f_t, and unconfined compressive strength, f_c.

Using Eq. (63), the nominal relation between f_t and V_{pore}, r_{pore}, and w/cm is expressed as

$$f_t = 0.177 \left(99.3 \, \frac{1 - V_{pore}}{w/cm \, \sqrt{r_{pore}}} \right)^{0.74}, \tag{66}$$

and the lower and upper bounds of f_t are expressed as

$$f_{t,lower} = 0.144 \left(1390 \, \frac{1 - V_{pore}}{w/cm \, \sqrt{r_{pore}}} \right)^{0.74}, \text{ and}$$

$$f_{t,upper} = 0.216 \left(1390 \, \frac{1 - V_{pore}}{w/cm \, \sqrt{r_{pore}}} \right)^{0.74}. \tag{67}$$

6.5   Response-performance relations

6.5.1   *Relation between panel thickness, fiber-reinforced tensile properties, and blast loading*

The relation between the tensile responses and blast loading is determined by the model at the structural length scale, as presented in Chapter 3. Inputs to the model include quasi-static tensile strength, T^o, and the dissipated energy density, E_{dis}, at an interface. The model at the structural length scale introduces strain-rate dependent behavior at the interfaces via a custom VUMAT. Results of the model at the structural length scale include the critical specific impulse at which the panel completely fractures, displacements of the center of the panel, and fracture patterns.

Excluding the data point for $T^o = 14.7$ MPa, $E_{dis} = 80$ kJ/m^2, $t_{panel} = 63.5$ mm, a linear regression analysis of the data shown in Figure 36 generates the following response function for critical specific impulse:

$$I_{cr} = -0.857 + 0.0262t + 6.51 \times 10^{-4} tT^o + 4.22 \times 10^{-4} tE_{dis}. \tag{68}$$
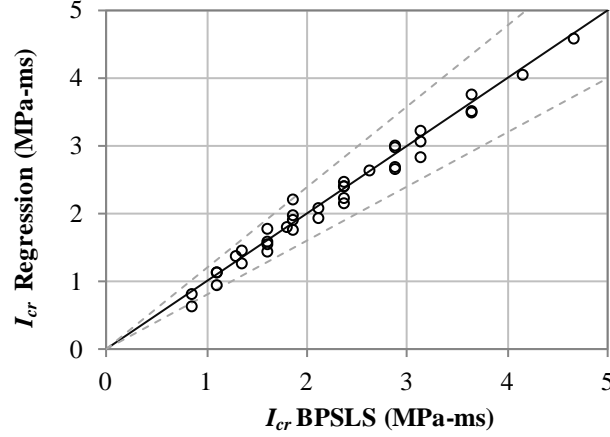
Figure 65. Comparison of the critical specific impulse I_{cr} as calculated by the Blast Panel Structural Length Scale (BPSLS) model and Equation (68). The solid black line represents a one-to-one relation and the dashed gray lines above and below the black line represent errors of $\pm\,10\%$.

6.5.2   *Relation between panel thickness, fiber-reinforced tensile strength, compressive strength, and impact loading*

The relation between the panel thickness, fiber-reinforced tensile strength, compressive strength, and impact loading is defined by the perforation model at the structural length scale. Results of the model indicate that the shatter resistance of a panel are highly dependent upon the dissipated energy density. Specifically, the panel was observed to not shatter for instantiations with dissipated energy densities greater than or equal to 5 MPa-mm. Therefore, a 5 MPa-mm level of dissipated energy density is the lower bound for the design.

6.6 Results

6.6.1 Feasible design space

The feasible properties must satisfy the both the blast loading and impact loading performance requirements. Recalling that the model of perforation at the structural length scale predicts the panel won't shatter for $E_{dis} \geq 5$ MPa-mm, the clarification of the design task to determine feasible properties is listed in Figure 66.

In Figure 66, the design space is shown at the top of the figure and discretized according to the following convention. The lower bound for the design space is given as the first number following the opening bracket. Separated by a colon, the number in the center of the bracket is the increment size, which is followed by another colon and the upper bound of the design space. For example, the quasi-static tensile strength, T^o, has a lower bound of 10 MPa, an increment of 2 MPa, and a maximum value of 20 MPa. Therefore, the discretized quasi-static tensile strength space is 10, 12, 14, 16, 18, and 20 MPa. The response is regression equation defined previously. For Figure 66, the response was defined in Section 6.5.1. The uncertainty is the assumed uncertainty in the variables of the design space and quantified uncertainty of the response functions.

Design Space	Matrix tensile strength, f_t	$x_1 = [\ 5\ \ :1\ \ :12\ ]$ (MPa)
	Axial length per revolution, $pitch$	$x_2 = [\ 6\ \ :3\ \ :36\ ]$ (mm)
	Panel thickness, t_{panel}	$x_3 = [\ 39\ \ :6\ \ :63\ ]$ (mm)
	Fiber volume fraction, V_f	$x_4 = [\ 0.5:0.5:\ \ 2\ ]$ (mm)
Responses	$T^o\ (f_t, pitch, t_{panel}) = 0.166 + 4320\ V_f\text{ - }62.4\ V_f pitch$	
	$E_{dis}\ (f_t, pitch, t_{panel}) = 0.85(1\text{-}V_f) + 1300 <V_f\text{-}0.0075>pitch^{-0.3}$	
Uncertainty	$\Delta x_1 = [\pm\ 10\%]$	
	$\Delta x_2 = [\pm\ 10\%]$	
	$\Delta x_3 = [\pm\ 10\%]$	
	$\Delta x_4 = [\pm\ 10\%]$	
	$T^o_{upper}\ (f_t, pitch, t) = 1.1\ T^o$	
	$T^o_{lower}\ (f_t, pitch, t) = 0.9\ T^o$	
	$E_{dis,upper}\ (f_t, pitch, t) = 1.2\ E_{dis}$	
	$E_{dis,lower}\ (f_t, pitch, t) = 0.8\ E_{dis}$	
Fixed Parameters	Fiber length	$L_{fiber} = 25$ mm
	Fiber cross-section width	$\phi_e\ = 0.5$ mm
Goal	The combination f_t–$pitch$–t_{panel}–V_f should satisfy the requirements quasi-static tensile strength, T^o, and dissipated energy density, E_{dis}, of the fiber-reinforced composite.	
Task Objectives	Identify the f_t–$pitch$–t_{panel}–V_f input space such that $HDEMI_{T^o} \geq 1$ and $HDEMI_{E_{dis}} \geq 1$.	

Figure 66. Clarification of design task for impulsive loading of UHPC panel.

With the design task clarified, IDEM can be used to determine the feasible design space and boundary of the feasible design space as shown in Figure 67. In Figure 67, sets of discrete input values satisfying the performance requirements are shown as blue outlined circles; sets of discrete input values at the boundary, i.e., $HDEMI_{I=1.5\ MPa-ms} = 1$, are shown as solid black diamonds. Infeasible points, i.e., $HDEMI_{I=1.5\ MPa-ms} < 1$, are not shown in Figure 67.
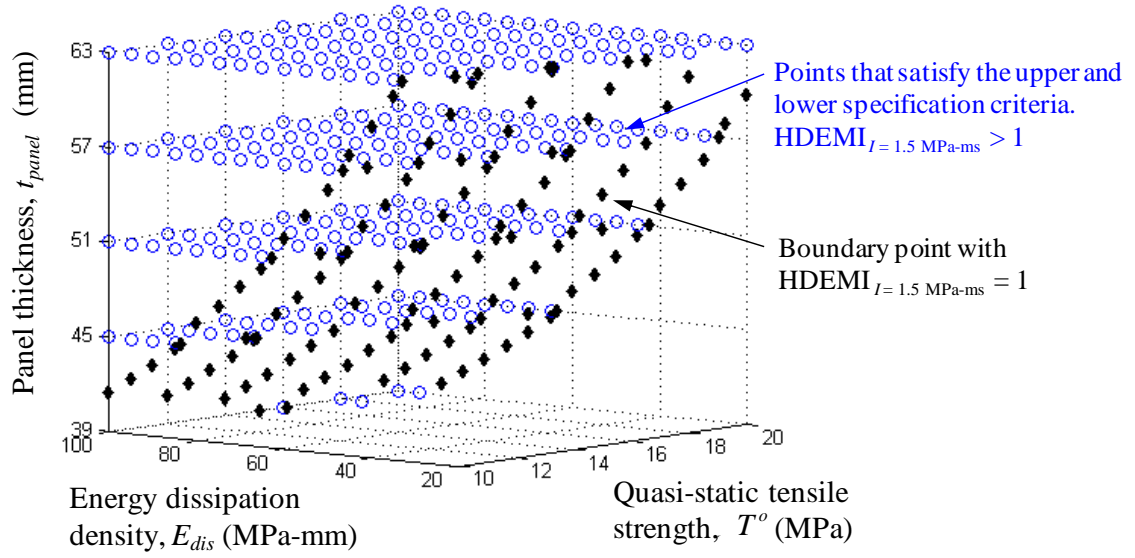
Figure 67. Feasible UHPC properties and panel thicknesses which survive a 1.5-MPa-ms specific impulse blast load and will not shatter as a consequence of being impacted by a 42.8-g projectile traveling at 1,000 m/s.

Figure 68 clarifies the design task to determine feasible matrix tensile strength, fiber pitch, panel thickness and fiber volume fractions. The feasible space of the two responses, quasi-static tensile strength of the fiber-reinforced microstructure, T^o, and dissipated energy density, E_{dis}, were found previously in Figure 67.

Design Space	Matrix tensile strength, f_t	$x_1 = [\ 5 \quad : 0.5\ :\ 9\ ]\,(\text{MPa})$
	Axial length per revolution, $pitch$	$x_2 = [\ 6 \quad :3 \quad :36\ ]\,(\text{mm})$
	Panel thickness, t_{panel}	$x_3 = [\ 39 \quad :6 \quad :63\ ]\,(\text{mm})$
	Fiber volume fraction, V_f	$x_4 = [\ 1.25:0.25:\ 2\ ]\,(\%)$

Responses

$T^o\,(f_t,\,pitch,\,t_{panel}) = 0.166 + 4320\,V_f - 62.4\,V_f pitch$

$E_{dis}\,(f_t,\,pitch,\,t_{panel}) = 0.85(1\text{-}V_f) + 1300 <V_f\text{-}\,0.0075>\,pitch^{\,-0.3}$

Uncertainty

$\Delta x_1 = [\pm\,10\%]$

$\Delta x_2 = [\pm\,10\%]$

$\Delta x_3 = [\pm\,10\%]$

$\Delta x_4 = [\pm\,10\%]$

$T^o_{upper}\,(f_t,\,pitch,\,t) = 1.1\,T^o$

$T^o_{lower}\,(f_t,\,pitch,\,t) = 0.9\,T^o$

$E_{dis,upper}\,(f_t,\,pitch,\,t) = 1.2\,E_{dis}$

$E_{dis,lower}\,(f_t,\,pitch,\,t) = 0.8\,E_{dis}$

Fixed Parameters	Fiber length	$L_{fiber} = 25\text{ mm}$
	Fiber cross-section width	$\phi_e \quad = 0.5\text{ mm}$

Goal — The combination f_t–$pitch$–t_{panel}–V_f should satisfy the requirements quasi-static tensile strength, T^o, and dissipated energy density, E_{dis}, of the fiber-reinforced composite.

Task Objectives — Identify the f_t–$pitch$–t_{panel}–V_f input space such that $HDEMI_{T^o} \geq 1$ and $HDEMI_{E_{dis}} \geq 1$.

Figure 68. Clarification of design task to determine material properties and structural attributes satisfying impact loading.

The clarified design task from Figure 68 facilitates IDEM to determine the feasible design space, as shown in Figure 69.
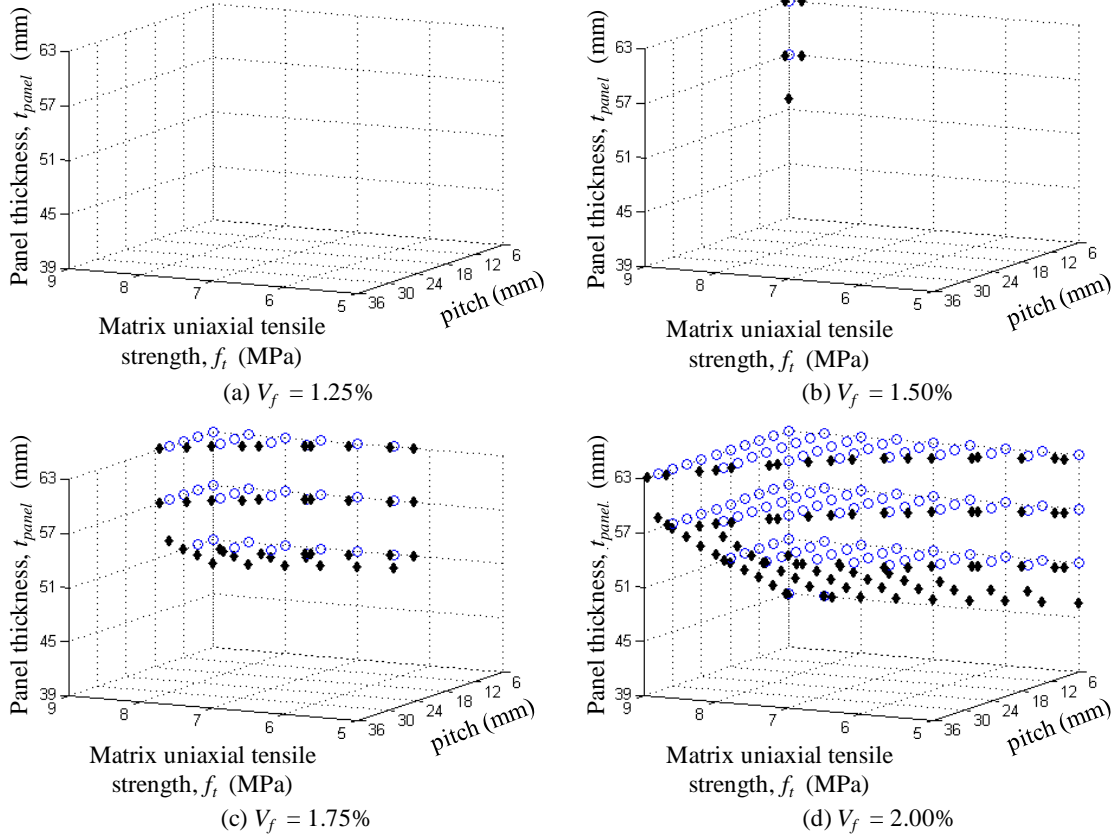
Figure 69. Feasible $f_t - pitch - t_{panel} - V_f$ input space that satisfies the identified $T^0 - E_{dis} - t_{panel}$ feasible space identified in Figure 67.

The remainder of this section provides the clarified design task for the material structures and processes in Figures 70 and 72, respectively. The feasible spaces and boundaries of the feasible spaces for structures and processes are shown in Figures 71 and 73, respectively. Note that for the clarification of the design task to define the feasible processing space shown in Figure 72 and the feasible processing design space in Figure 73, it is assumed that the UHPC has been thermally cured at 90 ℃; no points are feasible with a curing temperature of 20 ℃.

Design Space	Water to cementitious material ratio, w/cm	$x_1 = [\,0.15:\;0.05:\;0.45\,]\,(\;)$
	Volume fraction of pores, V_{pore}	$x_2 = [\,0.01:\;0.05:\;0.51\,]\,(\;)$
	Mean pore radii, r_{pore}	$x_3 = [\,1\quad:\;5\quad:31\quad]\,(nm)$

Responses

$$f_t\left(w/cm, V_{pore}, r_{pore}\right) = 0.177\left(99.3\,\frac{1-V_{pore}}{w/cm\,\sqrt{r_{pore}}}\right)^{0.74}$$

Uncertainty

$\Delta x_1 = [\pm\;\;5\%]$

$\Delta x_2 = [\pm\;\;5\%]$

$\Delta x_3 = [\pm\;10\%]$

$$f_{t,upper}\left(w/cm, V_{pore}, r_{pore}\right) = 0.216\left(99.3\,\frac{1-V_{pore}}{w/cm\,\sqrt{r_{pore}}}\right)^{0.74}$$

$$f_{t,lower}\left(w/cm, V_{pore}, r_{pore}\right) = 0.144\left(99.3\,\frac{1-V_{pore}}{w/cm\,\sqrt{r_{pore}}}\right)^{0.74}$$

Goal   The combination $w/cm-V_{pore}-r_{pore}$ should satisfy the requirements for non-fiber-reinforced matrix tensile strength, f_t.

Task Objectives   Identify the $w/cm-V_{pore}-r_{pore}$ input space such that $HDEMI_{f_t} \geq 1$.

Figure 70. Clarification of design task to determine material structural attributes satisfying the non-fiber-reinforced tensile strength of the matrix.
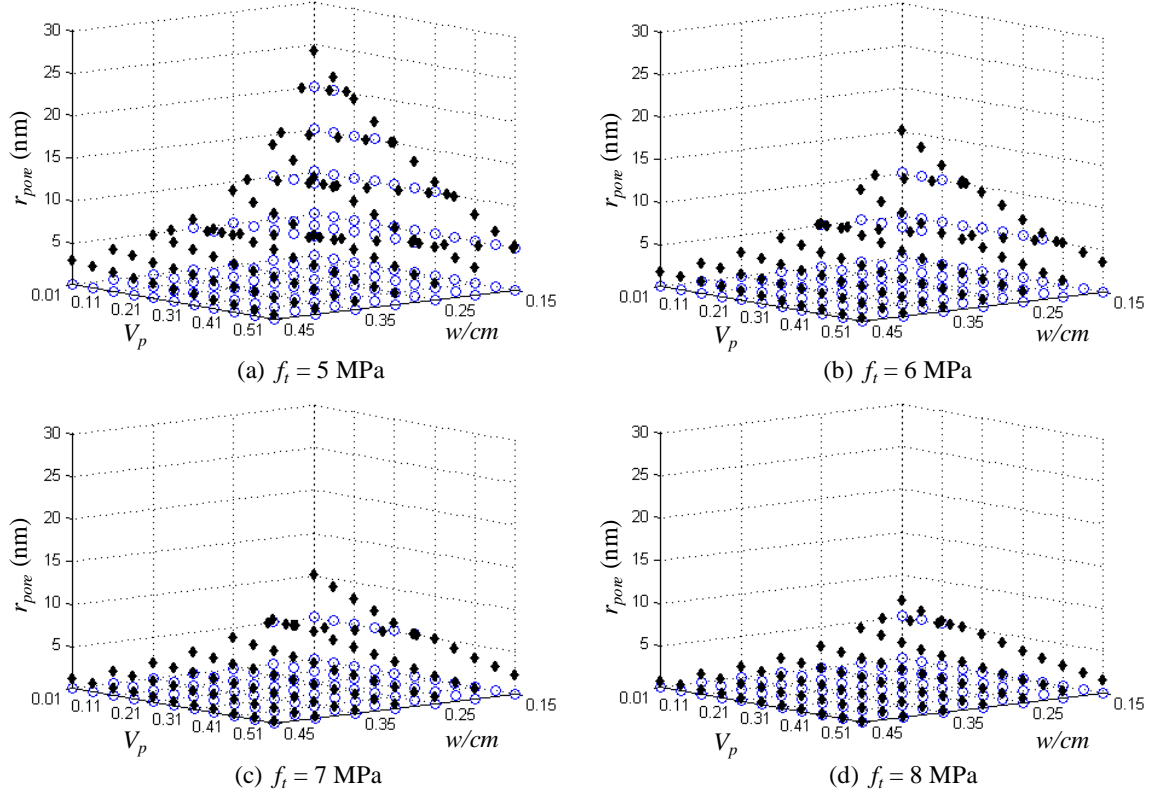
Figure 71. Feasible $w/cm - V_{pore} - r_{pore}$ input space that satisfies the specified uniaxial tensile strength of the matrix, f_t, for $5 \le f_t \le 8$ MPa.

Design Space	Curing temperature, T_{cure}	$x_1 = [\ 20, 90]\ (°C)$
	Volume fraction cement, V_{cem}	$x_2 = [\ 0.10 : 0.02 : 0.20]\ (\ )$
	Volume fraction silica fume, V_{SF}	$x_3 = [\ 0.01 : 0.01 : 0.05]\ (\ )$
	Water to cementitious material ratio, w/cm	$x_4 = [\ 0.20 : 0.02 : 0.30]\ (\ )$

Responses

$$V_{pore}\left(w/cm, V_{cem}, V_{SF}\right) = -0.0398 - 0.000167 T_{cure} + 0.201 V_{cem} + 0.193 V_{SF} + 0.298\,w/cm$$
$$- 0.00761 T_{cure} V_{cem} - 0.000735 T_{cure} V_{SF} - 0.00198 T_{cure}\,w/cm$$
$$- 0.315 V_{cem}^2 - 0.558 V_{cem} V_{SF} + 1.37 V_{cem}\,w/cm - 0.165\,w/cm^2$$

$$r_{pore}\left(w/cm, V_{cem}, V_{SF}\right) = 70.9 - 0.76 T_{cure} - 71.5 V_{cem} - 91.1 V_{sf} - 16.8\,w/cm$$
$$+ 1.10 T_{cure} V_{cem} + 1.33 T_{cure} V_{SF} + 0.307 T_{cure}\,w/cm - 31.9 V_{cem}^2$$
$$- 309 V_{cem} V_{SF} - 65.2 V_{cem}\,w/cm - 64.5 V_{SF}^2 - 78.3 V_{SF}\,w/cm$$

Uncertainty

$\Delta x_1 = [\pm\,0\%]$
$\Delta x_2 = [\pm\,5\%]$
$\Delta x_3 = [\pm\,5\%]$
$\Delta x_4 = [\pm\,5\%]$
$V_{pore,upper}\,(w/cm,\,V_{cem},\,V_{SF}) = 1.1\,V_{pore}$
$V_{pore,lower}\,(w/cm,\,V_{cem},\,V_{SF}) = 0.9\,V_{pore}$
$r_{pore,\,upper}\,(w/cm,\,V_{cem},\,V_{SF}) = 1.15\,r_{pore}$
$r_{pore,\,lower}\,(w/cm,\,V_{cem},\,V_{SF}) = 0.85\,r_{pore}$

Fixed Parameters

gradation of aggregate
$\rho_{cem} = 3{,}150\ \text{kg/m}^3, \rho_{SF} = 2{,}200\ \text{kg/m}^3$
$T_{cure} = 90\,°C$

Goal

The combination T_{cure}–V_{cem}–V_{SF}–w/cm should satisfy the requirements for volume fraction of porosity, V_{pore}, and average pore radius, r_{pore}

Task Objectives

Identify the T_{cure}–V_{cem}–V_{SF}–w/cm input space such that $HDEMI_{V_{pore}} \geq 1$, and $HDEMI_{r_{pore}} \geq 1$.

Figure 72. Clarification of design task to determine material processes satisfying the structure performance requirements.
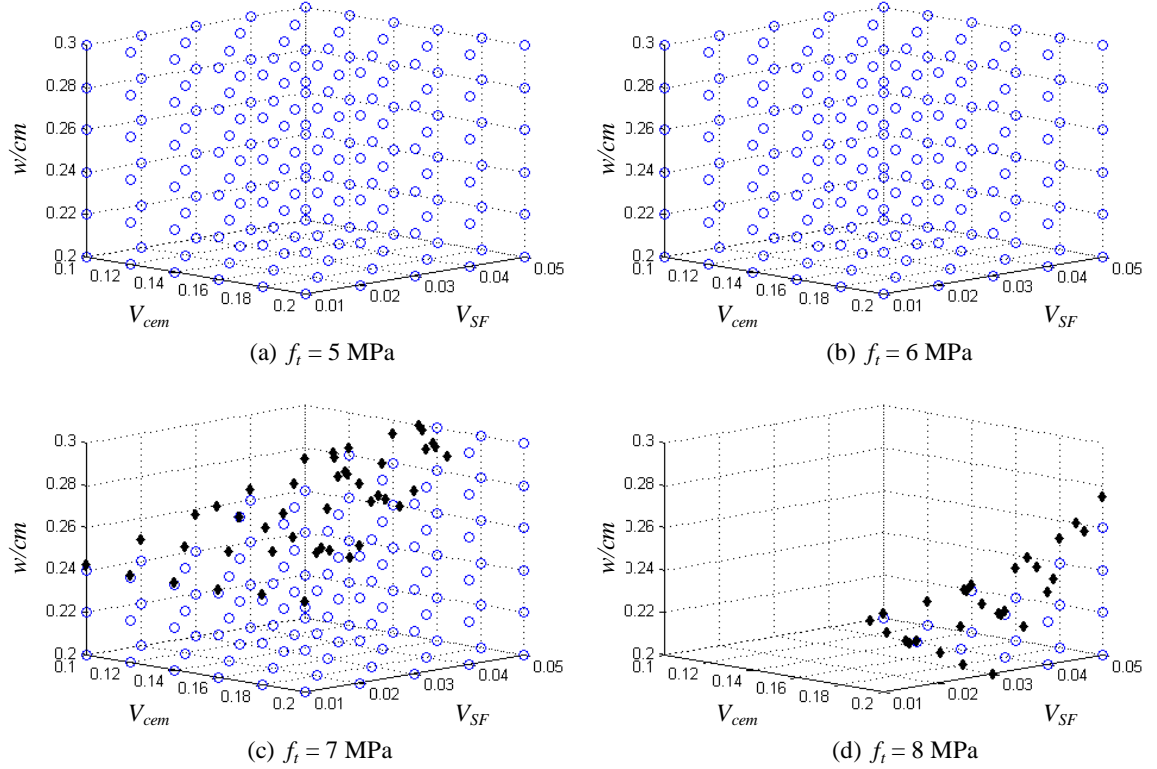
Figure 73. Feasible $V_{cem} - V_{SF} - w/cm$ input space that satisfies the specified uniaxial tensile strength of the matrix, f_t , for $5 \le f_t \le 8$ MPa and $T_{cure} = 90$ ºC.

6.6.2   Minimal mass within the feasible design space

Determining the minimum mass of a panel within the feasible design space is important for several reasons. First, the mass of the UHPC panel may impact the transportation of UHPC panels either from the construction site to the final structure or if the final structure is intended to be mobile. Second, the mass of UHPC panels may impact the design and load-carrying capability of the structure supporting the panels, thus causing the overall costs of a structure incorporating the UHPC panels to increase. Therefore, it is important to understand material and structural designs that satisfy the performance requirements while minimizing mass of the panel.

A rule of mixtures approach is utilized to calculate the mass density of the UHPC material, i.e.,

$$\rho_{UHPC} = V_{fiber}\rho_{fiber} + \left(1 - V_{fiber}\right)\left(V_{cem}\rho_{cem} + V_{SF}\rho_{SF} + V_{agg}\rho_{agg} + \frac{w/cm}{\rho_{water}}\left(V_{cem}\rho_{cem} + V_{SF}\rho_{SF}\right)\right), \quad (69)$$

where V_i are the volume fractions of the ith materials, and ρ_i are the mass densities of

the ith materials. In Eq. (69), the volume fractions and water to cement ratio are

determined from the feasible design space, and the mass densities are listed in Table 17.

The mass of the panel is

$$mass = \rho_{UHPC} t_{panel} w_{panel} h_{panel}, \quad (70)$$

where t_{panel} is the thickness of the panel which can vary between 39 and 63 mm, and

w_{panel} and h_{panel} are the width and height of the panel fixed to 1625.6 and 863.6 mm,

respectively.

Table 17. Mass densities of UHPC constituents.

ρ_{fiber} (kg/m^3)	ρ_{cem} (kg/m^3)	ρ_{SF} (kg/m^3)	ρ_{agg} (kg/m^3)	ρ_{water} (kg/m^3)
7,850	3,150	2,200	2,700	1,000

The mass of the panel was calculated using Eqs. (69) and (70) for each previously

identified feasible and boundary point. The minimum mass of all feasible and boundary

points was then found via the constrained optimization problem:

$$
\begin{aligned}
Minimize: \quad & mass \\
Subject\ to: \quad & HDEMI_i \geq 1 \\
& 39 \leq t_{panel} \leq 63 \\
& 6 \leq pitch \leq 36 \\
& 0 \leq V_{fiber} \leq 2\% \\
& 0.22 \leq w/cm \leq 0.30 \\
& 0.10 \leq V_{cem} \leq 0.20 \\
& 0.01 \leq V_{SF} \leq 0.05 \\
& T_{cure} = 20,\ 90\ ^{\circ}C
\end{aligned}
\tag{71}
$$

Results of the constrained optimization problem using data determined from a robust design approach indicate that a 160.0 kg UHPC panel can survive a 1.5 MPa-ms specific impulse. The preferred material design contains $V_{cem} = 0.196$, $V_{SF} = 0.049$, $w/cm = 0.30$, and $V_{agg} = 0.517$, and $V_{fiber} = 0.020$ of triangular cross section fibers that have been twisted to a 6-mm pitch,. After curing at 90 ºC , the matrix has a 7-MPa uniaxial tensile strength. Using the mass densities listed in Table 17, the UHPC material design uses 618 kg of Portland cement, 108 kg of silica fume, 218 kg of water, and 1396 kg of aggregate following the aggregate distribution given in Table 16. The feasible UHPC panel is 45.6-mm thick.

6.6.3 Minimal cost within the feasible design space

In addition to determining minimal mass of all possible feasible designs, other objective functions can be used. For example, a cost objective function

$$
cost = P_{UHPC} t_{panel} w_{panel} h_{panel}
\tag{72}
$$

can be defined, where the cost density of UHPC

$$P_{UHPC} = V_{fiber} \rho_{fiber} P_{fiber} +$$

$$\left(1 - V_{fiber}\right) \left(V_{cem} \rho_{cem} P_{cem} + V_{SF} \rho_{SF} P_{SF} + V_{agg} \rho_{agg} P_{agg} + \frac{w/cm}{\rho_{water}} \left(V_{cem} \rho_{cem} + V_{SF} \rho_{SF} \right) P_{water} \right) \tag{73}$$

defines the costs of the UHPC per unit volume. In Eq. (73), P_i is the cost of the ith

material per kg, with individual values of P_i are listed in United States Dollars (USD)

per kg of material in Table 18. The cost density of fiber, P_{fiber}, was calculated assuming

a 0.800 USD/kg cost density for raw steel, and that raw steel accounts for 40% of the

costs of the manufactured fibers. The cost densities for Portland Cement, P_{cem}, silica

fume, P_{SF}, and aggregate, P_{agg}, were sourced from the National Institute of Standards

and Technology (NIST) Concrete Optimization Software Tool (COST) program (*Cost

Optimization Software Tool (COST)*, 2001). The cost density of water, P_{water}, was

assumed.

Table 18. Cost densities of UHPC constituents.

P_{fiber} (USD/kg)	P_{cem} (USD/kg)	P_{SF} (USD/kg)	P_{agg} (USD/kg)	P_{water} (USD/kg)
2.00	0.081	0.88	0.013	0.0004

The minimum cost of the UHPC panel is determined through the constrained

optimization problem

$$
\begin{aligned}
Minimize: &\quad cost \\
Subject\ to: &\quad HDEMI_i \geq 1 \\
&\quad 39 \leq t_{panel} \leq 63 \\
&\quad 6 \leq pitch \leq 36 \\
&\quad 0 \leq V_{fiber} \leq 2\% \\
&\quad 0.22 \leq w/cm \leq 0.30 \\
&\quad 0.10 \leq V_{cem} \leq 0.20 \\
&\quad 0.01 \leq V_{SF} \leq 0.05 \\
&\quad T_{cure} = 20,\ 90\ ^\circ C
\end{aligned}
\tag{74}
$$

Results of the constrained optimization problem using feasible and boundary data points from IDEM indicate that preferred minimized cost UHPC panel costs \$23.79 per panel, or \$339 / m^3. The preferred material design contains $V_{cem} = 0.197$, $V_{SF} = 0.029$, $w/cm = 0.20$, and $V_{agg} = 0.620$, and $V_{fiber} = 0.017$ of fibers having triangular cross sections that have been twisted to a 6-mm pitch, . The matrix has an 8-MPa uniaxial tensile strength, created by curing a mixture of at 90 ºC. Using the mass densities listed in Table 17, the UHPC material design uses 621 kg of Portland cement, 64 kg of silica fume, 1674 kg of aggregate following the aggregate distribution given in Table 16 representing a 2-mm maximum aggregate size sand mixed with quartz powder, and 137 kg of water. The feasible UHPC panel is 50.9 mm thick.

6.7   Summary

This chapter exercises a computational framework for the design of materials with a hierarchy of microstructures and mesostructures via hierarchical multiscale modeling to define the deductive mappings and the Inductive Design Exploration Method (IDEM) to define the inductive decision path.

The hierarchical multiscale model draws upon previous results in this dissertation, e.g. models at the single fiber and structural length scales, as well as analytical models and data taken from literature. For example, this chapter introduces the Mix Constituent and curing Temperature to Porosity (MCTP) model to relate the volume fractions of aggregate, cement, and silica fume; assumed distribution of aggregate size; mass ratio of water to cementitious material; and curing temperature to the volume fraction of porosity and the mean pore radii. MCTP is a combination of the void exclusion probability model (Lu & Torquato, 1992), Powers hydration model (cf. Mindess et al., 2002), and Linear Packing Model (Stovall et al., 1986) which has been validated in comparison to the experimental work of Klobes et al. (2008).

After defining the deductive mappings, IDEM is applied to top level of hierarchy, i.e., the relation between the panel thickness, quasi-static tensile strength, dissipated energy density, and the panel surviving the 1.5 MPa-ms specific impulse blast load and the relation between dissipated energy density and the panel not completely fracturing due to the perforation of a projectile traveling 1,000 m/s, to determine the feasible space of panel thicknesses, quasi-static tensile strengths, and dissipated energy densities. The feasible space of panel thickness, quasi-static tensile strengths, and dissipated energy densities are then searched for the boundary between the feasible and infeasible spaces. For multilevel problems, the boundary of the input space is used for the performance requirement for the next finer scale of hierarchy. For example, the next finer level of hierarchy for the quasi-static tensile strength and dissipated energy density space is the space of matrix tensile strength, fiber pitch, and fiber volume fraction. The iterative

process continues until the finest level of hierarchy is searched for parameters that satisfy the performance requirement of the next coarser hierarchy.

The objective functions of mass and cost were used to determine the preferred set of solutions from all identified feasible and boundary solutions. It was determined that the preferred solution to minimize mass was different than the preferred solution to minimize cost.

There are two significant aspects to this work. First, a set of PSPP relations were identified for the design of UHPC materials and structures for ballistic and blast loading. These relations facilitate not only the design of UHPC materials and structures for the stated performance requirements, but allow the new UHPC materials and structures to be rapidly designed based on new performance requirements. The second significant aspect of this work is that it exercised a computational framework for the design of new materials and structures to significantly reduce the time required compared to empirical development routes.

CHAPTER 7:

CONCLUSIONS

7.1 Summary

A computational framework was developed and exercised for the design of Ultra-High-Performance Concrete (UHPC) materials and structures subject to a blast load with a specific impulse between 1.25- and 1.5-MPa-ms and the impact of a 0.50-caliber bullet travelling at a velocity between 900 and 1,000 m/s. The considered structure for blast loading was a 1626-mm tall by 864-mm wide panel with a uniform, but adjustable, thickness; the considered structure for impact loading was a 305-mm tall by 305-mm wide panel made from the same material and to the thickness as the blast panel.

The computational framework consists of two distinct paths – a bottom-up deductive modeling and simulation path and a top-down inductive decision path – through a set of process-structure-property-performance (PSPP) relations. The bottom-up deductive mappings consist of two analytical models and two multiscale models, each consisting of three length scales. The first analytical model defines a relation between volume fractions of Portland cement, silica fume, and aggregates; aggregate size distribution; curing temperatures; pore volume fraction; and mean pore radius through a combination of the void exclusion probability model, Powers hydration model, and Linear Packing Model. The second analytical model defines a relation between volume fraction of porosity, mean pore radius, and the uniaxial quasi-static tensile strength of a

non-fiber-reinforced cementitious matrix. Both multiscale models consist of models at three length scales – single fiber, multiple fiber, and structural. At the single fiber length scale, a model was developed to predict the pullout force as a function of material properties and fiber morphology, which is expressed via the fiber's cross section, equivalent diameter, and the pitch at which the fiber was twisted. The model accounts energy dissipated due to granular flow of the 50-µm-thick ITZ and surrounding cement paste, friction between the fiber and the matrix, and the plastic work of the fiber. The resulting pullout force versus end slip relations are projected onto each fiber at the multiple fiber length scale. The multiple fiber length scale accounts for the overall fiber volume fraction, each fiber's embedded length and inclination angle, and the tensile strength of the cementitious matrix to determine a Gaussian distribution of the quasi-static tensile strength and dissipated energy density due to separation at a predefined crack plane. The mean and the standard deviation of the quasi-static tensile strength and the dissipated energy density of the fiber-reinforced matrix are used within a hand-shaking scheme to inform zero-thickness strain-rate sensitive cohesive elements at the structural length scale. By incorporating the cohesive elements, the two models at the structural length scale can account for dynamic fracture of fiber-reinforced UHPCs.

After defining the deductive mappings, the PSPP relations were searched for combinations of properties, structures, and processing steps that satisfied the system-level blast and impact performance requirements via the Inductive Design Exploration Method (IDME). For the considered PSPP relations and loading conditions, the design problem was delineated into four levels of hierarchy. Starting at the top level of hierarchy, IDEM discretized input variables, projected each set of discretized input values with account of

197

uncertainty to a range in the output space, and determined which sets of discrete input values satisfied the output space performance requirements. The feasible input values, i.e., the input values that satisfied the output space requirements, were used to determine the boundary of the feasible space, which was then used as the boundary of the output space for the next finer level of hierarchy. Through this recursive scheme, IDEM determined the feasible values of the seven design variables (i.e., curing temperature, water to cementitious material ratio, fiber pitch, and volume fractions of fiber, silica fume, aggregate, and Portland cement), which the designer can directly control. Finally, preferred combinations of the feasible values of design variables were determined through the use of objective functions, defined in terms of mass and raw material cost of the of the manufactured panel.

7.2 Summary of principles for designing UHPC materials for extreme loading conditions

The design of UHPC materials and structures for extreme loading conditions, such as blast and impact, requires detailed analysis. However, research presented in this dissertation and available in the literature provides general guidelines for the design of UHPC materials and structures. This section summarizes these findings.

Impact resistance of UHPC materials and structures can be broadly delineated into resistance to shattering, perforation, spalling, and penetration. This work found that dissipated energy densities less than 5 MPa-mm led to the shattering of UHPC panels irrespective of panel thicknesses between 38.1 and 76.2 mm. One method of producing panels with a minimum dissipated energy density of 5 MPa-mm is to introduce a 0.75%

fiber volume fraction of 14-mm long by 0.185-mm diameter straight, smooth fibers to the UHPC matrix. This conclusion is qualitatively, if not quantitatively, consistent with experimental results of Zhang et al. (2005), who found that cementitious panels incorporating a 1.5% fiber volume fraction of 13-mm long by 0.2-mm diameter fibers reduced the propagation of cracks beyond the impact crater sufficiently to prevent fracture into two or more pieces. Additionally, Zhang et al. (2005) found that similar cementitious panels without fibers shattered due to impact. Similar results were found by Dancygier and Yankelevsky (1996) using 0.8% fiber volume fractions of 30-mm long by 0.5-mm diameter hooked fibers in cementitious panels with compressive strengths between 95 and 104 MPa. Beyond shatter resistance, fibers have been shown to reduce the size of proximal craters (Zhang et al., 2005). However, fiber content has a minimal influence on either perforation or penetration responses of cementitious panels (Almusallam et al., 2013; Zhang et al., 2005).

The ability of a cementitious panel to decelerate a projectile can be measured by either the penetration depth (i.e., the distance a projectile travels from the proximal face before stopping within a cementitious panel) or the residual velocity (i.e., the velocity at which a projectile exits distal face of the cementitious panel) of the projectile. Although both the penetration depth and the residual velocity have been reduced by increased unconfined compressive strengths, the reduction was marginal for compressive strengths above MPa (Hanchak et al., 1992; Zhang et al., 2005). This conclusion has motivated some authors to postulate that a 100-MPa unconfined compressive strength is preferred due to economic considerations (Zhang et al., 2005).

Numerical simulations of 1,626-mm tall by 864-mm wide UHPC panels without rebar-reinforcement were conducted to determine combinations of quasi-static tensile strength of the fiber-reinforced UHPC, dissipated energy of the fiber-reinforced UHPC, and panel thickness (38.1 to 63.5 mm) which survived blast loads with specific impulses between 0.5 and 4.5 MPa-ms. The results, presented in Figure 36, were used to determine the critical specific impulse, defined as the maximum specific impulse which the panel will not fracture into two or more pieces, of each combination of panel thickness, quasi-static tensile strength, and dissipated energy density. Results indicate the numerical simulations indicate the preferred avenue to improve the critical specific impulse is the dissipated energy density. Results from the multiple fiber length scale indicate the dissipated energy density is primarily influenced by the type of fibers with twisted fibers preferred to straight smooth fibers. For specific impulse greater than the critical specific impulse, most panels failed in a brittle fashion, i.e., fractured in the center and then fractured near the top and bottom restraints. However, numerical simulations indicate that a ductile response is possible with dramatically greater critical specific impulses. For example, a 63.5-mm-thick panel with a 14.7-MPa quasi-static tensile strength and an 80-kJ/m^2 dissipated energy density had a critical specific impulse of 4.65 MPa-ms, which was 28% greater than the 3.63 Mpa-ms for a similar panel with a 20-MPa quasi-static tensile strength. One method to achieve the 80-kJ/m^2 dissipated energy density for the simulated ductile response is to incorporate 2.0% fiber volume fraction of 25-mm long by 0.5-mm equivalent diameter triangular fibers with a 6-mm pitch. However, it is impossible to achieve the 80-kJ/m^2 dissipated energy density with straight, smooth fibers.

7.3 Novel contributions

The unique contributions of this dissertation are as follows.

- Develops and validates a multiscale model at three different length scales for predicting the evolution of damage, deflection, and critical impulse for a UHPC panel subjected to blast loading;

- Develops a computational framework for the analysis of uniformly pitched non-circular cross section reinforcement fibers pulled from a cementitious matrix. This framework represents the first time that uniformly pitched non-circular cross section fibers have been (1) modeled in the finite element framework and (2) modeled within a matrix with constitutive properties other than an elastic, homogeneous matrix;

- Provides an alternate explanation of the mechanisms causing the elastic-plastic response of twisted fibers being pulled from a cementitious matrix;

- Implements the Inductive Design Exploration Method (IDEM) (Choi et al., 2008) in a large multiscale framework; and

- Identifies preferred designs that minimize cost and mass of UHPC materials for structures and satisfy system performance requirements related to blast and impact.

7.4 Suggestions for future work

This dissertation has focused on developing and exercising a computational framework for the design of cementitious materials and structures using data available in literature as well as various engineering assumptions. To refine this research, it is recommended to pursue the following avenues listed in order or priority.

First, it is recommended to validate the pullout response of a single twisted fiber pulled from cementitious matrices with unconfined compressive strengths between 100 and 200 MPa. Experimental data in the literature documents the pullout response of twisted fibers from cementitious materials with unconfined compressive strengths from 28 to 84 MPa (e.g. Kim et al., 2009; Sujivorakul, 2002), but experimental data does not exist for matrices with unconfined compressive strengths greater than 84 MPa.

Second, it is recommended to develop strain-rate sensitivity within the model at the single fiber length scale. Although not important for straight, smooth or hooked fibers, twisted fibers exhibited strain-rate sensitivity in the pullout force versus end slip response for end slip rates between 0.0178 and 17.8 mm/s (Kim et al., 2009). In particular, slower slip-rates produced a slip-hardening response and less total energy dissipated; higher slip rates produced a slip-neutral pullout response with slightly greater total energy dissipated. Of most concern, the 17.8 mm/s slip-rates caused the fiber to break during pullout. This refinement at the single fiber length scale would be used to inform the blast model at the structural length scale. The ultimate effect is that the pitch of the fiber might need to be reduced in order to prevent fiber breakage.

Third, explore the ductile response of UHPC panels at high energy dissipation and thickness. This response was somewhat unexpected and the region of response should be investigated numerically and experimentally to determine the bounds of the response.

Fourth, incorporate exposure to rapid thermal heating as one of the performance requirements. It is well documented that UHPCs exposed to rapid thermal heating experience thermal spall, defined as the ejection of mass from the heated surface (e.g.

Kalifa et al., 2001; Kalifa, Menneteau, & Quenard, 2000). This undesirable response has been experimentally shown to be mitigated through the addition of polypropylene fibers.

Finally, it is recommended to validate the shatter resistance of UHPC panels subject to ballistic impact. Ideally, a designed experiment would be performed to determine the threshold fiber volume fraction such that the panels do not fracture as a function of panel thickness, and unconfined compressive strength. This experimental data could be used to validate the numerically determined threshold value of dissipated energy density.

REFERENCES

Abu Al-Rub, R. K., & Voyiadjis, G. Z. (2009). Gradient-enhanced couple plasticity-anisotropic damage model for concrete fracture: Computational aspects and applications. *International Journal of Damage Mechanics*, **18**(2):115–154.

Alexander, M. G., & Mindess, S. (2005). Aggregates in Concrete. Taylor & Francis.

Almusallam, T. H., Siddiqui, N. A., Iqbal, R. A., & Abbas, H. (2013). Response of hybrid-fiber reinforced concrete slabs to hard projectile impact. *International Journal of Impact Engineering*, **58**:17–30.

Alwan, J. M., Naaman, A. E., & Guerrero, P. (1999). Effect of mechanical clamping on the pull-out response of hooked steel fibers embedded in cementitious matrices. *Concrete Science and Engineering*, **1**:15–25.

American Concrete Institute (ACI) Committee 318. (2008a). Building Code Requirements for Structural Concrete and Commentary (ACI 318-08, ISO 19338:200. ACI.

Anon. (1988). Densit patent brochure. Densit. Retrieved from http://www.densit.sk/_upload/files/beton-teknik-uk.pdf

ASTM International. (2004). Standard test method for splitting tensile strength of cylindrical concrete specimens (Testing Standard No. C 496/C 496M). West Conshohocken, PA: ASTM.

ASTM International. (2007). Standard specification for steel wire, music spring quality (Testing Standard No. A 228/A 228M). West Conshohocken, PA: ASTM.

ASTM International. (2008b). Standard specification for concrete aggregates (Testing Standard No. C 33/C 33M-08). ASTM.

ASTM International. (2012a). Standard test method for compressive strength of cylindrical concrete specimens (Testing Standard No. C 39/C 39M). West Conshohocken, PA: ASTM.

ASTM International. (2012b). Standard test method for flexural performance of fiber-reinforced concrete (using beam with third-point loading) (Testing Standard No. C1609/C1609M-12). ASTM.

Bache, H. H. (1981). Densified cement ultrafine particle-based materials (p. 35). Presented at the The Second International Conference on Superplasticizers in Concrete, Ottawa, Canada.

Backman, M. E., & Goldsmith, W. (1978). The mechanics of penetration of projectiles into targets. *International Journal of Engineering Science*, **16**(1):1–99.

Baltay, P., & Gjelsvik, A. (1990). Coefficient of friction for steel on concrete at high normal stress. *Journal of Materials in Civil Engineering*, **2**(1):46–49.

Bentz, D. P. (2000). Fibers, percolation, and spalling of High-Performance Concrete. *ACI Materials Journal*, **97**(3):351–359.

Bernard, R. S., & Hanagud, S. V. (1975). Development of a Projectile Penetration Theory (No. S-75-9) (p. 101). Vicksburg, MS: U.S. Army Engineers Waterways Experiment Station.

Biggs, J. M. (1964). Introduction to structural dynamics.

Bilodeau, A., Kodur, V. K. ., & Hoff, G. . (2004). Optimization of the type and amount of polypropylene fibres for preventing the spalling of lightweight concrete subjected to hydrocarbon fire. *Cement and Concrete Composites*, **26**(2):163–174.

Bishop, R. F., Hill, R., & Mott, N. F. (1945). The theory of indentation and hardness tests. *Proceedings of the Physical Society*, **57**(3):147–159.

Bolander, J. E., Choi, S., & Duddukuri, S. R. (2009). Fracture of fiber-reinforced cement composites: effects of fiber dispersion. *International Journal of Fracture*, **154**(1-2):73–86.

Bolander Jr., J. E., & Saito, S. (1997). Discrete modeling of short-fiber reinforcement in cementitious composites. *Advanced Cement Based Materials*, **6**(3–4):76–86.

Boshoff, W. P., Mechtcherine, V., & van Zijl, G. P. A. G. (2009). Characterising the time-dependant behaviour on the single fibre level of SHCC: Part 2: The rate effects on fibre pull-out tests. *Cement and Concrete Research*, **39**(9):787–797.

Carrere, N., Valle, R., Bretheau, T., & Chaboche, J.-L. (2004). Multiscale analysis of the transverse properties of Ti-based matrix composites reinforced by SiC fibres: from the grain scale to the macroscopic scale. *International Journal of Plasticity*, **20**(4–5):783–810.

CEB-FIP. (1998). CEB-FIP Model Code 1990. Thomas Telford.

Chakrabarty, J. (2006). Theory of Plasticity, Third Edition (3rd ed.). Butterworth-Heinemann.

Chan, Y.-W., & Chu, S.-H. (2004a). Effect of silica fume on steel fiber bond characteristics in reactive powder concrete. *Cement and Concrete Research*, **34**(7):1167–1172.

Chan, Y.-W., & Chu, S.-H. (2004b). Effect of silica fume on steel fiber bond characteristics in reactive powder concrete. *Cement and Concrete Research*, **34**(7):1167–1172.

Chen, W., Allen, J. K., Tsui, K.-L., & Mistree, F. (1996). A procedure for robust design: Minimizing variations caused by noise factors and control factors. *Journal of Mechanical Design*, **118**(4):478–485.

Chen, X. W., & Li, Q. M. (2002). Deep penetration of a non-deformable projectile with different geometrical characteristics. *International Journal of Impact Engineering*, **27**(6):619–637.

Cheyrezy, M., Maret, V., & Frouin, L. (1995). Microstructural analysis of RPC (Reactive Powder Concrete). *Cement and Concrete Research*, **25**(7):1491–1500.

Choi, H.-J. (2005). A Robust Design Method for Model and Propagated Uncertainty (Ph.D. Dissertation). Georgia Institute of Technology, Atlanta, GA.

Choi, H.-J., Austin, R., Allen, J. K., McDowell, D. L., Mistree, F., & Benson, D. J. (2005a). An approach for robust design of reactive power metal mixtures based on non-deterministic micro-scale shock simulation. *Journal of Computer-Aided Materials Design*, **12**(1):57–85.

Choi, H.-J., Austin, R., Allen, J. K., McDowell, D. L., Mistree, F., & Benson, D. J. (2005b). An approach for robust design of reactive powder metal mixtures based on non-deterministic micro-scale shock simulation. *Journal of Computer-Aided Materials Design*, **12**(1):57–85.

Choi, H.-J., McDowell, D. L., Allen, J. K., Rosen, D., & Mistree, F. (2008). An inductive design exploration method for robust multiscale materials design. *Journal of Mechanical Design*, **130**(3):031402–031413.

Choi, S.-K., Grandhi, R., & Canfield, R. A. (2007). Reliability-based Structural Design (1st ed.). London: Springer.

Clayton, J. D. (2008). A model for deformation and fragmentation in crushable brittle solids. *International Journal of Impact Engineering*, **35**(5):269–289.

Cohen, M. D., Lee, T.-F. F., & Goldman, A. (1995). A method for estimating the dynamic moduli of cement paste-aggregate interfacial zones in mortar. *Microstucture of Cement-Based Systems/Bonding and Interface in Cementitious Materials* (Vol. 370, pp. 407–412). Pittsburgh, PA: Materials Research Socity Symposium Proceedings.

Cost Optimization Software Tool (COST). (2001). National Institute of Standards and Technology. Retrieved from http://ciks.cbt.nist.gov/cost/

Cumberland, D. J., & Crawford, R. J. (1987). The Packing of Particles. Amsterdam: Elsevier.

Cunha, V. M. C. F., Barros, J. A. O., & Sena-Cruz, J. M. (2010). Pullout Behavior of Steel Fibers in Self-Compacting Concrete. *Journal of Materials in Civil Engineering*, **22**(1):1.

Dancygier, A. N., & Yankelevsky, D. Z. (1996). High strength concrete response to hard projectile impact. *International Journal of Impact Engineering*, **18**(6):583–599.

Dancygier, A. N., Yankelevsky, D. Z., & Jaegermann, C. (2007). Response of high performance concrete plates to impact of non-deforming projectiles. *International Journal of Impact Engineering*, **34**(11):1768–1779.

Davies, R. M. (1948). A critical study of the Hopkinson pressure bar. *Philosophical Transactions of the Royal Society of London. Series A, Mathematical and Physical Sciences*, **240**(821):375–457.

De Larrard, F., & Sedran, T. (1994). Optimization of ultra-high-performance concrete by the use of a packing model. *Cement and Concrete Research*, **24**(6):997–1009.

Dessault Systemes. (2010). Abaqus v6.10 Theory Manual. Dassault Systemes.

DiPaolo, B. P., Johnson, C. F., Green, B. H., Hart, W. S., Magee, R. E., & Robbins, B. A. (2012). Stuctured-materials (Stuc'd Mats) design concept and its application for protective structures panels: Blast and sequence ballistic-blast testing (ERDC/GSL No. TR-12) (p. 147). Vicksburg, MS: U.S. Army Engineering Research and Development Center.

Drucker, D. C., & Prager, W. (1952). Soil mechanics and plastic analysis or limit design. *Quart Appl Math*, **10**:157–165.

Du, X., & Chen, W. (2002). Efficient uncertainty analysis methods for multidisciplinary robust design. *AIAA Journal*, **40**(3):545–552.

Easley, T. C., Faber, K. T., & Shah, S. P. (1999). Use of a crack-bridging single-fiber pullout test to study steel fiber/cementitious matrix composites. *Journal of the American Ceramic Society*, **82**(12):3513–3520.

El-Dieb, A. S. (2009). Mechanical, durability and microstructural characteristics of ultra-high-strength self-compacting concrete incorporating steel fibers. *Materials & Design*, **30**(10):4286–4292.

Ellis, B. D., DiPaolo, B. P., McDowell, D. L., & Zhou, M. (2013). Experimental investigation and multiscale modeling of Ultra-High-Performance Concrete panels subject to blast loading. *submitted to Int. J. of Impact Engineering*.

Fedors, R. F., & Landel, R. F. (1979). An Empirical method of estimating the void fraction in mixtures of uniform particles of different size. *Powder Technology*, **23**(2):225–231.

Focacci, F., Nanni, A., & Bakis, C. (2000). Local Bond-Slip Relationship for FRP Reinforcement in Concrete. *Journal of Composites for Construction*, **4**(1):24–31.

Forrestal, M. J., & Luk, V. K. (1992). Penetration into soil targets. *International Journal of Impact Engineering*, **12**(3):427–444.

Forrestal, M. J., & Tzou, D. Y. (1997). A spherical cavity-expansion penetration model for concrete targets. *International Journal of Solids and Structures*, **34**(31–32):4127–4146.

Furnas, C. C. (1931). Grading aggregates: I. Mathematical relations for beds of broken solids of maximum density. *Ind Eng Chem*, **23**(9):1052–1058.

Gao, J., Sun, W., & Morino, K. (1997). Mechanical properties of steel fiber-reinforced, high-strength, lightweight concrete. *Cement and Concrete Composites*, **19**(4):307–313.

Gao, Y., De Schutter, G., Ye, G., Huang, H., Tan, Z., & Wu, K. (2013). Porosity characterization of ITZ in cementitious composites: Concentric expansion and overflow criterion. *Construction and Building Materials*, **38**:1051–1057.

Garas-Yanni, V. Y. (2009). Multi-Scale Investigation of Tensile Creep of Ultra-High Performance Concrete for Bridge Applications (Ph.D.). Georgia Institute of Technology, Atlanta, GA.

Garboczi, E. J., & Bentz, D. P. (1991). Digital-simulation of the aggregate-cement paste interfacial zone in concrete. *Journal of Material Research*, **6**(1):196–201.

Garboczi, E. J., & Bentz, D. P. (1998). Multiscale Analytical/Numerical Theory of the Diffusivity of Concrete. *Advanced Cement Based Materials*, **8**(2):77–88.

Gebbeken, N., Greulich, S., & Pietzsch, A. (2006). Hugoniot properties for concrete determined by full-scale detonation experiments and flyer-plate-impact tests. *International Journal of Impact Engineering*, **32**(12):2017–2031.

Ghosh, S., Lee, K., & Raghavan, P. (2001). A multi-level computational model for multi-scale damage analysis in composite and porous materials. *International Journal of Solids and Structures*, **38**(14):2335–2385.

Goltermann, P., Johansen, V., & Palbol, L. (1997). Packing of Aggregates: An alternative tool to determine the optimal aggregate mix. *ACI Materials Journal*, **94**(5):435–443.

Goodier, J. N. (1964). On the Mechanics of Indentations and cratering in Solid Targets of Strain-Hardening Metal by Impact of Hard and Soft Spheres (No. 002-64) (p. 100). Menlo Park, CA: Stanford Research Institute, Pouter Research Laboratories.

Gopalaratnam, V. S., & Shah, S. P. (1987). Tensile failure of steel fiber-reinforced mortar. *Journal of engineering mechanics*, **113**(5):635–652.

Graybeal, B. (2012). Construction of field-cast Ultra-High Performance Concrete connections (No. FHWA-HRT-12-038) (p. 8). McLean, VA: U.S. Department of Transportation.

Griffith, A. A. (1921). The Phenomena of Rupture and Flow in Solids. *Philosophical Transactions of the Royal Society of London. Series A, Containing Papers of a Mathematical or Physical Character*, **221**:163–198.

Grote, D. L., Park, S. W., & Zhou, M. (2001). Dynamic behavior of concrete at high strain rates and pressures: I. experimental characterization. *International Journal of Impact Engineering*, **25**(9):869–886.

Gu, X., Renaud, J. E., Batill, S. M., Brach, R. M., & Budhiraja, A. S. (2000). Worst case propagated uncertainty of multidisciplinary systems in robust design optimization. *Structural and Multidisciplinary Optimization*, **20**(3):190–213.

Guerrero, P., & Naaman, A. E. (2000). Effect of mortar fineness and adhesive agents on pullout response of steel fibers. *ACI Materials Journal*, **97**(1):12–22.

Hanagud, S., & Ross, B. (1971). Large deformation, deep penetration theory for a compressible strain-hardening target material. *AIAA Journal*, **9**(5):905–911.

Hanchak, S. J., Forrestal, M. J., Young, E. R., & Ehrgott, J. Q. (1992). Perforation of concrete slabs with 48 MPa (7 ksi) and 140 MPa (20 ksi) unconfined compressive strengths. *International Journal of Impact Engineering*, **12**(1):1–7.

HardwireLLC. (n.d.). Hardwire 3x2_cord_US. Hardwire. Retrieved from http://www.hardwirellc.com/resources/brochures/hw_cord_specs/US/3X2_cord_US.pdf

Harrington, E. C. (1965). The desirability functoin. *Industrial Quality Control*, **21**:494–498.

Hashin, Z. (1992). Extremum principles for elastic heterogenous media with imperfect interfaces and their application to bounding of effective moduli. *Journal of the Mechanics and Physics of Solids*, **40**(4):767–781.

Hashin, Z., & Shtrikman, S. (1963). A variational approach to the theory of the elastic behaviour of multiphase materials. *Journal of the Mechanics and Physics of Solids*, **11**(2):127–140.

Hassaballah, A., & Wenzel, T. H. (1995). A strength definition for the water to cementitious materials ratio. *Proceedings ACI 5th International Conference, Fly Ash, Silica Fume and Natural Pozzolans in Concrete* (Vol. 153, pp. 417–438). Presented at the ACI 5th International Conference, Fly Ash, Silica Fume and Natural Pozzolans in Concrete, Milwaukee, WI: ACI.

Helton, J. C., & Davis, F. J. (2003). Latin hypercube sampling and the propagation of uncertainty in analyses of complex systems. *Reliability Engineering & System Safety*, **81**(1):23–69.

Hertz, K. D. (2003). Limits of spalling of fire-exposed concrete. *Fire Safety Journal*, **38**(2):103–116.

Hillerborg, A., Modéer, M., & Petersson, P.-E. (1976). Analysis of crack formation and crack growth in concrete by means of fracture mechanics and finite elements. *Cement and Concrete Research*, **6**(6):773–781.

Holmquist, T. J., Johnson, G. R., & Cook, W. H. (1993). A computational constitutive model for concrete subjected to large strains, high strain rates, and high pressures. *Proceedings of the 14th international symposium on ballistics* (pp. 591–600). Presented at the 14th International Symposium on Ballistics, Quebed City, Canada: American Defense Preparedness Association (ADPA).

Hopkinson, B. (1914). A method of measuring the pressure produced in the detonation of high explosives or by the impact of bullets. *Philosophical Transactions of the Royal Society of London. Series A, Containing Papers of a Mathematical or Physical Character*, **213**:437–456.

Isukapalli, S. S., Roy, A., & Georgopoulos, P. G. (1998). Stochastic Response Surface Methods (SRSMs) for Uncertainty Propagation: Application to Environmental and Biological Systems. *Risk Analysis*, **18**(3):351–363.

Jirásek, M. (1998). Nonlocal models for damage and fracture: Comparison of approaches. *International Journal of Solids and Structures*, **35**(31-32):4133–4145.

Jirásek, M., & Rolshoven, S. (2003). Comparison of integral-type nonlocal plasticity models for strain-softening materials. *International Journal of Engineering Science*, **41**(13-14):1553–1602.

Johnston, C. D. (2001). Fiber-Reinforced Cements and Concretes (1st ed.). Amsterdam: Gordon and Breach Publishers.

Jones, M. R., Zheng, L., & Newlands, M. D. (2002). Comparison of particle packing models for proportioning concrete constitutents for minimum voids ratio. *Materials and Structures*, **35**(5):301–309.

Kabele, P. (2007). Multiscale framework for modeling of fracture in high performance fiber reinforced cementitious composites. *Engineering Fracture Mechanics*, **74**(1-2):194–209.

Kachanov, L. M. (1958). On the creep fracture time. *Izv. Akad. Nauk USSR Otd. Tech*, **8**:26–31.

Kalifa, P., Chéné, G., & Gallé, C. (2001). High-temperature behaviour of HPC with polypropylene fibres: From spalling to microstructure. *Cement and Concrete Research*, **31**(10):1487–1499.

Kalifa, P., Menneteau, F.-D., & Quenard, D. (2000). Spalling and pore pressure in HPC at high temperatures. *Cement and Concrete Research*, **30**(12):1915–1927.

Kelly, T. D., van Oss, H. G., & Matos, G. R. (2012). U.S. Geological Survey Data Series 140: Cement statistics. Reston, VA. Retrieved from http://minerals.usgs.gov/ds/2005/140/ds140-cemen.pdf

Kennedy, R. P. (1976). A review of procedures for the analysis and design of concrete structures to resist missile impact effects. *Nuclear Engineering and Design*, **37**(2):183–203.

Kim, D., El-Tawil, S., & Naaman, A. E. (2007). Correlation between single fiber pullout behavior and tensile response of FRC composites with high strength steel fiber. *High Performance Fiber Reinforced Cement Composites (HPFRCC5)* (pp. 67–76). Mainz, Germany.

Kim, D. J., El-Tawil, S., & Naaman, A. E. (2009). Rate-dependent tensile behavior of high performance fiber reinforced cementitious composites. *Materials and Structures*, **42**(3):399–414.

Klobes, P., Rübner, K., Hempel, S., & Prinz, C. (2008). Investigation of the microstructure of Ultra High Performance Concrete. *Characterisation of Porous Solids VIII*, English (pp. 354–361). Presented at the 8th International Symposium on the Characterisation of Porous Solids, Edinburgh, UK: Royal Society of Chemistry.

Köksal, F., Altun, F., Yigit, I., & Sahin, Y. (2008). Combined effect of silica fume and steel fiber on the mechanical properties of high strength concretes. *Construction and Building Materials*, **22**(8):1874–1880.

Kolsky, H. (1949). An investigation of the mechanical properties of materials at very high rates of loading. *Proceedings of the Physical Society. Section B*, **62**(11):676–700.

Kouznetsova, V., Geers, M. G. D., Brekelmans, W. a. M., Kouznetsova, V., Geers, M. G. D., & Brekelmans, W. a. M. (2002). Multi-scale constitutive modelling of heterogeneous materials with a gradient-enhanced computational homogenization scheme. *International Journal for Numerical Methods in Engineering*, **54**(8):1235–1260.

Kumar, R., & Bhattacharjee, B. (2003). Porosity, pore size distribution and in situ strength of concrete. *Cement and Concrete Research*, **33**(1):155–164.

Kumar, S. V., & Santhanam, M. (2003). Particle packing theories and their application in concrete mixture proportioning: A review. *Indian Concrete Journal*, **77**(9):1324–1331.

Lan, S., Lok, T.-S., & Heng, L. (2005). Composite structural panels subjected to explosive loading. *Construction and Building Materials*, **19**(5):387–395.

Larrard, F. de. (1999). Concrete mixture proportioning : a scientific approach /. Modern concrete technology series ; E & FN Spon,.

Lee, J., & Fenves, G. L. (1998). Plastic-damage model for cyclic loading of concrete structures. *Journal of Engineering Mechanics*, **124**(8):892–900.

Leppänen, J. (2005). Experiments and numerical analyses of blast and fragment impacts on concrete. *International Journal of Impact Engineering*, **31**(7):843–860.

Li, C. Y., & Mobasher, B. (1998). Finite element simulations of fiber pullout toughening in fiber reinforced cement based composites. *Advanced Cement Based Materials*, **7**(3–4):123–132.

Li, Q. M., Reid, S. R., Wen, H. M., & Telford, A. R. (2005). Local impact effects of hard missiles on concrete targets. *International Journal of Impact Engineering*, **32**(1–4):224–284.

Li, Q. M., & Tong, D. J. (2003). Perforation Thickness and Ballistic Limit of Concrete Target Subjected to Rigid Projectile Impact. *Journal of Engineering Mechanics*, **129**(9):1083–1091.

Li, V. C., Wang, Y., & Backer, S. (1990). Effect of inclining angle, bundling and surface treatment on synthetic fibre pull-out from a cement matrix. *Composites*, **21**(2):132–140.

Lim, D. H., & Oh, B. H. (1999). Experimental and theoretical investigation on the shear of steel fibre reinforced concrete beams. *Engineering Structures*, **21**(10):937–944.

Liu, H., Chen, W., Kokkolaras, M., Papalambros, P. Y., & Kim, H. M. (2005). Probabilistic analytical target cascading: A moment matching formulation for multilevel optimization under uncertainty. *Journal of Mechanical Design*, **128**(4):991–1000.

Lu, B., & Torquato, S. (1992). Nearest-surface distribution functions for polydispersed particle systems. *Physical Review A*, **45**(8):5530–5544.

Lubliner, J., Oliver, J., Oller, S., & Oñate, E. (1989). A plastic-damage model for concrete. *International Journal of Solids and Structures*, **25**(3):299–326.

Luscher, D. (2010). A Hierarchical Framework for the Multiscale Modeling of Microstructure Evolution in Heterogeneous Materials (Ph.D.). Georgia Institute of Technology, Atlanta, GA.

Luscher, D. J., McDowell, D. L., & Bronkhorst, C. A. (2010). A second gradient theoretical framework for hierarchical multiscale modeling of materials. *International Journal of Plasticity*, **26**(8):1248–1275.

Lyons, A. (2012). Materials for Architects and Builders. Routledge.

Maekawa, K., Chaube, R., & Kishi, T. (1999). Modelling of Concrete Performance: Hydration, Micro-Structure Formation, and Mass Transport. New York, NY: E & FN Spon.

Maekawa, K., Ishida, T., & Kishi, T. (2003). Integrated Material and Structural Mechanics. *Journal of Advanced Concrete Technology*, **1**(2):91–126.

Maekawa, K., Okamura, H., & Pimanmas, A. (2003). Non-Linear Mechanics of Reinforced Concrete. New York, NY: Spon Press.

Malvar, J., & Ross, C. A. (1998). Review of strain rate effects for concrete in tension. *ACI Materials Journal*, **95**(6):735–739.

Malvern, L. E., Tang, T., Jenkins, D. A., & Gong, J. C. (1985). Dynamic compressive strength of cementitious materials. *MRS Online Proceedings Library*, **64**:119–138.

McDowell, D. L. (2010). A perspective on trends in multiscale plasticity. *International Journal of Plasticity*, **26**(9):1280–1309.

McDowell, D. L., Panchal, J., Choi, H.-J., Seepersad, C., Allen, J., & Mistree, F. (2009a). Integrated Design of Multiscale, Multifunctional Materials and Products (1st ed.). Butterworth-Heinemann.

McDowell, D. L., Panchal, J., Choi, H.-J., Seepersad, C., Allen, J., & Mistree, F. (2009b). Integrated Design of Multiscale, Multifunctional Materials and Products (1st ed.). Butterworth-Heinemann.

McGeary, R. K. (1961). Mechanical packing of spherical particles. *Journal of the American Ceramic Society*, **44**(10):513–522.

McVeigh, C., Vernerey, F., Liu, W. K., & Cate Brinson, L. (2006). Multiresolution analysis for material design. *Computer Methods in Applied Mechanics and Engineering*, **195**(37–40):5053–5076.

Mehta, P., & Monteiro, P. (2005). Concrete: Microstructure, Properties, and Materials (3rd ed.). McGraw-Hill Professional.

Menzel, C. (1952). A Proposed Standard Deformed Bar For Reinforcing Concrete. *Studies of Bond Between Concrete and Steel: a compilation of five papers* (pp. 11–64). Chicago, IL: Portland Cement Association, Research and Development Laboratories.

Mindess, S., Young, J. F., & Darwin, D. (2002). Concrete (2nd ed.). Prentice Hall.

Mistree, F., Hughes, O. F., & Bras, B. (1993). Compromise decision support problem and the adaptive linear programming algorithm. In M. P. Kamat (Ed.), *Structural Optimization: Status and Promise*, Progress in Astronautics and Aeronautics (1st ed., Vol. 150, pp. 251–290). USA: American Institute of Aeronautics and Astronautics (AIAA).

Murphy, T., Tsui, K.-L., & Allen, J. K. (2005). A review of robust design methods for multiple responses. *Research in Engineering Design*, **15**(4):201–215.

Naaman, A. (1999). Optimized geometries of fiber reinforcements of cement, ceramic and polymeric based composites.

Naaman, A. (2003). Engineered steel fibers with optimal properties for reinforcement of cement composites. *Journal of Advaced Concrete Technology*, **1**(3):241–252.

Naaman, A. E. (1985). Fiber reinforcement for concrete. *ACI Concrete International*, **7**(3):21–25.

Naaman, A. E., Namur, G. ., Alwan, J. M., & Najm, H. S. (1991). Fiber pullout and bond slip. I: Analytical study. *Journal of Structural Engineering*, **117**(9):2769–2790.

Naaman, A. E., & Wille, K. (2012). The path to Ultra-High Performance Fiber Reinforced Concrete (UHP-FRC): Five decades of progress. *Proceedings of HiPerMat 2012 3rd International Symposium on UHPC and Nanotechnology for High performance Construction Materials* (pp. 3–16). Presented at the Ultra-High Performance Concrete and Nanotechnology in Construction, Kassel, Germany: Kassel University Press.

Nöldgen, M., Fehling, E., Riedel, W., & Thoma, K. (2012). Vulnerability and robustness of a security skyscraper subjected to aircraft impact. *Computer‑Aided Civil and Infrastructure Engineering*, **27**(5):358–268.

Nyström, U., & Gylltoft, K. (2009). Numerical studies of the combined effects of blast and fragment loading. *International Journal of Impact Engineering*, **36**(8):995–1005.

Odler, I., & Rößler, M. (1985). Investigations on the relationship between porosity, structure and strength of hydrated Portland cement pastes. II. Effect of pore structure and of degree of hydration. *Cement and Concrete Research*, **15**(3):401–410.

Oh, B. ., Cha, S. W., Jang, B. S., & Jang, S. Y. (2002). Development of high-performance concrete having high resistance to chloride penetration. *Nuclear Engineering and Design*, **212**(1-3):221–231.

Ollivier, J. P., Maso, J. C., & Bourdette, B. (1995). Interfacial transition zone in concrete. *Advanced Cement Based Materials*, **2**(1):30–38.

Olson, G. B. (1997). Computational design of hierarchically structured materials. *Science*, **277**(5330):1237 –1242.

Oluokun, F. (1991). Prediction of concrete tensile strength from its compressive strength: Evaluation of existing relations for normal weight concrete. *ACI Materials Journal*, **88**(3):302–309.

Orange, G., Acker, P., & Vernet, C. (1999). A new generation of UHP concrete: Ductal(R) damage resistance and micromechanical analysis. *Proceedings PRO6: International RILEM Conference on High Performance Fiber Reinforced Cement Composites (HPFRCC 3)* (pp. 101–110). Presented at the International RILEM Conference on High Performance Fiber Reinforced Cement Composites (HPFRRCC 3), Main: RILEM.

Park, S. H., Kim, D. J., Ryu, G. S., & Koh, K. T. (2012). Effect of adding micro fibers on the pullout behavior of high strength steel fibers in UHPC matrix. *Proceedings of HiPerMat 2012 3rd International Symposium on UHPC and Nanotechnology for High performance Construction Materials* (pp. 541–548). Presented at the 3rd International Symposium on UHPC and Nanotechnology for High Performance Construction Materials, Kassel, Germany: Kassel University Press.

Park, S. W., Xia, Q., & Zhou, M. (2001). Dynamic behavior of concrete at high strain rates and pressures: II. numerical simulation. *International Journal of Impact Engineering*, **25**(9):887–910.

Parkhouse, J. G., & Kelly, A. (1995). The random packing of fibres in three dimensions. *Proceedings: Mathematical and Physical Sciences*, **451**(1943):737–746.

Pignatiello, J. J. (1993). Strategies for robust multiresponse quality engineering. *IIE Transactions*, **25**(3):5–15.

Powers, T. C. (1958). Structure and Physical Properties of Hardened Portland Cement Paste. *Journal of the American Ceramic Society*, **41**(1):1–6.

Pul, S. (2008). Experimental investigation of tensile behaviour of high strength concrete. *Indian Journal of Engineering and Material Sciences*, **15**:467–472.

Rebentrost, M., & Wight, G. (2008). Behaviour and resistance of Ultra High Performance Concrete to blast effects. *Ultra High Performance Concrete (UHPC)* (pp. 735–742). Presented at the Second International Symposium on Ultra High Performance Concrete, Kassel, Germany: Kassel University Press.

Rebentrost, M., & Wight, G. (2009). Investigation of UHPFRC slabs under blast loads (pp. 1–8). Presented at the FIB UHPFRC 2009, Marseille, France.

Ren, F., Mattus, C. H., Wang, J. J.-A., & DiPaolo, B. P. (2013). Effect of projectile impact and penetration on the phase composition and microstructure of high-performance concretes. *Cement and Concrete Composites*.

Richard, P., Cheyrezy, M., & Dugat, J. (1996). Method and a composition for preparing concrete elements having remarkable compressive strength and fracture energy, and elements obtained thereby.

Richard, P., Cheyrezy, M., & Roux, N. (1996). Metal fiber concrete compositions for molding concrete elements, elements obtained and curing process. Saint Quentin Yvelines, France.

Riedel, W., Kawai, N., & Kondo, K. (2009). Numerical assessment for impact strength measurements in concrete materials. *International Journal of Impact Engineering*, **36**(2):283–293.

Riedel, W., Nöldgen, M., Straßburger, E., Thoma, K., & Fehling, E. (2010). Local damage to Ultra High Performance Concrete structures caused by an impact of aircraft engine missiles. *Nuclear Engineering and Design*, **240**(10):2633–2642.

Riedel, W., Thoma, K., Hiermaier, S., & Schmolinske, E. (1999). Penetration of reinforced concrete by BETA-B-500 Numerical analysis using a new macroscopic concrete model for hydrocodes. *Proceedings of the 9th International Symposium on the Effects of Munitions with Structures*. Presented at the 9th International Symposium on the Effects of Munitions with Structures, Berlin-Straussberg, Germany.

Riedel, W., Wicklein, M., & Thoma, K. (2008). Shock properties of conventional and high strength concrete: Experimental and mesomechanical analysis. *International Journal of Impact Engineering*, **35**(3):155–171.

Rossi, P. (2005). Multiple scale cement composite with positive and ductile setting in uniaxial tension.

Schenker, A., Anteby, I., Gal, E., Kivity, Y., Nizri, E., Sadot, O., Michaelis, R., et al. (2008). Full-scale field tests of concrete slabs subjected to blast loads. *International Journal of Impact Engineering*, **35**(3):184–198.

Scheydt, J. C., & Müller, H. S. (2012). Microstructure of Ultra High Performance Concrete (UHPC) and its impact on durability. *Proceedings of HiPerMat 2012 3rd International Symposium on UHPC and Nanotechnology for High performance Construction Materials* (pp. 349–356). Presented at the 3rd International Symposium on UHPC and Nanotechnology for High Performacne Construction Materials, Kassel, Germany: Kassel University Press.

Schleyer, G. K., Barnett, S. J., Millard, S. G., & Wight, G. (2010a). Modelling the response of UHPFRC panels to explosive loading. *Structures Under Shock and Impact XI* (pp. 173–184). Presented at the International Conference on Structures under Shock and Impact, Tallin, Estonia: WIT Press.

Schleyer, G. K., Barnett, S. J., Millard, S. G., & Wight, G. (2010b). Modelling the response of UHPFRC panels to explosive loading. *Structures Under Shock and Impact XI* (pp. 173–184). Presented at the International Conference on Structures under Shock and Impact, Tallin, Estonia: WIT Press.

Schmit, L., & Mehrinfar, M. (1982). Multilevel optimum design of structures with fiber-composite stiffened-panel construction. *AIAA Journal*, **20**(1):138–147.

Shannag, M. J., Brincker, R., & Hansen, W. (1997). Pullout behavior of steel fibers from cement-based composites. *Cement and Concrete Research*, **27**(6):925–936.

Siddique, R. (2008). Waste Materials and By-Products in Concrete. Springer.

Simeonou, P. I., & Ahmad, S. H. (1995). Interface transition zone and the elastic modulus of cement-based computers. *Microstucture of Cement-Based Systems/Bonding and Interface in Cementitious Materials* (Vol. 370, pp. 397–406). Pittsburgh, PA: Materials Research Society Symposium Proceedings.

Sobieszczanski-Sobieski, J., James, B., & Riley, M. (1987). Structural sizing by generalized, multilevel optimization. *AIAA Journal*, **25**(1):139–145.

Song, P. S., & Hwang, S. (2004). Mechanical properties of high-strength steel fiber-reinforced concrete. *Construction and Building Materials*, **18**(9):669–673.

Stovall, T., de Larrard, F., & Buil, M. (1986). Linear packing density model of grain mixtures. *Powder Technology*, **48**(1):1–12.

Sujivorakul, C. (2002). Development of High Performance Fiber Reinforced Cement Composites Using Twisted Polygonal Steel Fibers (Ph.D.). University of Michigan, Ann Arbor, MI.

Sujivorakul, C., & Naaman, A. (2002). Evaluation of Bond-Slip Behavior of Twisted Wire Strand Steel Fibers Embedded in Cement Matrix. *Proceedings of ACI Symposium on Concrete: Material Science to Applicatioons, a Tribut to S.P. Shah, ACI SP-206*, 271–292.

Sujivorakul, C., & Naaman, A. (2003). Modeling bond components of deformed steel fibers in FRC composites. *Proceedings of International Workshop on High Performance Fiber Reinforced Cement Composites (HPFRCC-4)*, Pro 30 (pp. 35–48). RILEM Publications.

Taguchi, G. (1986). Introduction to Quality Engineering: Designing Quality into Products and Processes. White Plains, NY: Kraus International Publications.

Taguchi, G. (1992). Taguchi on Robust Technology Development: Bringing Quality Engineering Upstream. ASME Press (American Society of Mechanical Engineers).

Thomas, M. D. A., Green, B., O'Neal, E., Perry, V., Hayman, S., & Hossack, A. (2012). Marine performance of UHPC at Treat Island. *Ultra-High Performance Concrete and Nanotechnology in Construction* (pp. 365–370). Presented at the 3rd International Symposium on UHPC and Nanotechnology for High Performance Construction Materials, Kassel, Germany: Kassel University Press.

Vermeer, P. A., & de Borst, R. (1984). Non-associated plasticity for soils, concrete and rock. *Heron*, **29**(3):1–64.

Wafa, F., & Ashour, S. (1992). Mechanical properties of High-Strength Fiber Reinforced Concrete. *ACI Materials Journal*, **89**(5):449–455.

Wang, J. A. J., Mattus, C. H., & Ren, F. (2009). DHS counter Improvised Explosive Device Effects Basic Research Project (DHS cIED project) FY09 Final Report (No. ORNL/TM-2009/317) (p. 108). Oak Ridge, TN: Oak Ridge National Laboratories.

Wong, H. S., & Abdul Razak, H. (2005). Efficiency of calcined kaolin and silica fume as cement replacement material for strength performance. *Cement and Concrete Research*, **35**(4):696–702.

Wu, C., Oehlers, D. J., Rebentrost, M., Leach, J., & Whittaker, A. S. (2009). Blast testing of ultra-high performance fibre and FRP-retrofitted concrete slabs. *Engineering Structures*, **31**(9):2060–2069.

Yankelevsky, D. Z. (1997). Local response of concrete slabs to low velocity missile impact. *International Journal of Impact Engineering*, **19**(4):331–343.

Yao, W., Li, J., & Wu, K. (2003). Mechanical properties of hybrid fiber-reinforced concrete at low fiber volume fraction. *Cement and Concrete Research*, **33**(1):27–30.

Yazıcı, H., Yardımcı, M. Y., Aydın, S., & Karabulut, A. Ş. (2009). Mechanical properties of reactive powder concrete containing mineral admixtures under different curing regimes. *Construction and Building Materials*, **23**(3):1223–1231.

Zhang, J., Yan, C. W., & Jia, J. Q. (2010). Compressive strength and splitting tensile strength of Steel Fiber Reinforced Ultra High Strength Concrete (SFRC). *Applied Mechanics and Materials*, **34-35**:1441–1444.

Zhang, M. H., Shim, V. P. W., Lu, G., & Chew, C. W. (2005). Resistance of high-strength concrete to projectile impact. *International Journal of Impact Engineering*, **31**(7):825–841.

Zheng, W., Kwan, A. K. H., & Lee, P. K. K. (2001). Direct tension test of concrete. *ACI Materials Journal*, **98**(1):63–71.

Zhou, X. Q., Kuznetsov, V. A., Hao, H., & Waschl, J. (2008). Numerical prediction of concrete slab response to blast loading. *International Journal of Impact Engineering*, **35**(10):1186–1200.